Testing and Analysis of Shape-memory Polymers for Morphing Aircraft Skin Application

by

Scott Gibson Rauscher

B.S. in Mechanical Engineering, University of Pittsburgh, 2006

Submitted to the Graduate Faculty of

Swanson School of Engineering in partial fulfillment

of the requirements for the degree of

Master of Science

University of Pittsburgh

2008

UNIVERSITY OF PITTSBURGH

SWANSON SCHOOL OF ENGINEERING

This thesis was presented

by

Scott Gibson Rauscher

It was defended on

April 11th, 2008

and approved by

Dr. Lisa Mauck Weiland, Assistant Professor, Department of Mechanical Engineering and Materials Science

Dr. William Slaughter III, Professor, Department of Mechanical Engineering and Materials Science

Thesis Advisor: Dr. William W. Clark, Professor, Department of Mechanical Engineering and Materials Science

Testing and Analysis of Shape-memory Polymers for Morphing Aircraft Skin Application

Scott Gibson Rauscher, M.S.

University of Pittsburgh, 2008

Morphing aircraft have the potential to possess a variety of advantages over current static aircraft, such as improved maneuverability, increased speed and better fuel efficiency. This thesis focuses on testing the feasibility of a shape-memory polymer to function as the skin of a morphing aircraft undergoing the wing-sweep method of wing shape-change. A review of literature is presented, giving a brief history of shape-memory polymers, an overview of current significant shape-memory polymer application, an overview of current morphing aircraft in morphing application and an overview of the current methods to activate shape-memory polymers. Analytical and finite element models are created to predict out-of-plane deformations caused by aerodynamic loads on an independently functioning sub-section of a tile array that would comprise the skin of a morphing aircraft. Five generations of a shape-memory polymer tile sub-section with embedded fibers are described and subsequently tested to confirm analytical and finite element models. Alternate shape-memory polymer tile sub-sections are created to specifically address the problem of buckling as the tile experiences shear-induced shape-change mimicking that seen in a morphing aircraft. Bi-axial pre-strains are induced on the alternate tile sub-sections to successfully cure the buckling problem. Finite element modeling, thermal analytical analysis and screw-driven load frame machine data are used to calculate the power required to induce shape-change as well as sufficiently heat the tile sub-section via its embedded

wires. Power requirements, experimental results and modeling results are discussed in terms of real-world feasibility. Finally, suggestions are made for future work on a similar topic.

TABLE OF CONTENTS

LIST OF TABLES

LIST OF FIGURES

ACKNOWLEDGMENTS

First and foremost, I would like to thank Dr. William W. Clark, my advisor, for his support and guidance throughout my time here at the University of Pittsburgh. I recognize how fortunate I was to be able to work under him as a graduate student and I am grateful for all that he has done. I would also like to thank the members of the Vibration and Control Laboratory and the members of the Sound, Systems and Structures Laboratory for their friendship, advice and ability to keep me sane.

1.0 INTRODUCTION

Most aircraft are currently designed for a single mission with a single purpose. Different wing patterns are used by aircraft undertaking different missions. For example, an F-17 is designed specifically and only for attack missions, while a Boeing 747 is designed for long-distance, large-load flights. This limitation on current aircraft requires the use of multiple aircraft to undertake a multifaceted mission. The inefficiencies of this become immediately clear. If an F-17 were able to efficiently fly a long distance, execute an attack mission and then efficiently fly the same distance back, the need for an aircraft carrier could be eliminated. An F-17, however, is not designed to be able to fly long distances efficiently. Likewise, there are many scenarios that if a single aircraft could efficiently execute a variety of missions, the number of different aircraft as well as the number of total aircraft could be significantly decreased. The next logical question becomes: So how do we add this increased versatility?

Since the wings of an aircraft are the most defining feature in controlling the way in which an aircraft moves and functions, it makes sense to focus on modification of the wings. If the wings of an aircraft were able to change shape mid-flight (or even on the ground), that same aircraft could then be used to execute more than one type of mission at a high level of efficiency. The shape-changing aircraft could also maintain an optimal wing pattern during each stage of flight of each mission, thus improving its range, maneuverability and speed. A

great deal of research has been completed in an effort to create and optimize such a morphing aircraft.

It is the focus of this thesis to simulate, test and model the stages of shape-change of the wings of a theoretical morphing aircraft structure (MAS). Since the design of the wing will consist of a pattern of many identical "tiles", the actual tests and simulations will be performed on one of these tiles. Experimental and theoretical analyses will be implemented in order to predict and verify the behavior of these independently functional subsections as they undergo shape-change in the presence of an aerodynamic pressure load, a shear force and applied heat. In the process of determining the behavior of a tile test specimen, and subsequently trying to control it, additional analyses will be conducted that relate less directly to the application of a morphing aircraft wing.

1.1 OUTLINE OF THESIS

This thesis will be presented in the following manner:

A review of literature is first presented. A brief history of shape-memory materials is presented, followed by some of the most extraordinary current applications and research. Review of past work in morphing aircraft is given, including the 8-year long DARPA/NASA/AFRL funded MAV project.

Motivation for the need of shape-changing aircraft is given, which is then related to the purpose of this thesis. Background information on shape-memory polymers (SMPs) and previous relevant concept design is given through the literature review. Previous and expected problems are also reviewed from previous SMP morphing aircraft projects.

Several theoretical and finite element models are created of the tile sub-section undergoing heating, shearing and pressure loading. First, a fiber-embedded shape-memory polymer plate (FESMPP) is analyzed mathematically, and later with ANSYS, to predict out-of-plane deflections caused by a simulated aerodynamic pressure load. An analytical and finite element model are also created for an SMP plate without fibers for comparison. An SMPP is then analyzed using a finite element model to predict out-of-plane deformations caused by the folding associated with shearing-induced shape-change. A finite element model is then created to cure the large deformations by utilizing bi-axial pre-strains. A FESMPP in its un-strained, initial state is then analyzed with ANSYS to determine optimal heating parameters and the time required to fully heat the plate to its transition temperature. These parameters are then used to determine the associated power requirements. Mechanical power requirements are then found (using ANSYS) for the shearing motion required to induce shape-change as well as the loads required to induce a pre-strain.

The procedure behind experimental testing is discussed, including the method used to create bi-axial pre-strains for the pre-tensioned SMP plate to be used for reduction of deformation caused by shape-change. Experimental results are then given followed by results and conclusions. Improvements are suggested and possible future work is then discussed.

2.0 LITERATURE REVIEW

A shape-memory polymer is, in the broadest of senses, a polymer material that has the ability to "remember" its initial geometric configuration. Generally, the polymer is created in an initial shape, re-formed into a secondary shape and then controllably activated (most commonly via applied heat) to return to its original shape. Transformation of the SMP from its secondary shape to its initial shape begins to occur only after the SMP reaches its predefined transition temperature, known as the glass transition temperature. This glass transition temperature is an inherent property of the polymer that is defined within the SMP recipe prior to manufacturing. The word "memory" in shape-memory polymer is especially appropriate because once the polymer is stimulated while in its secondary state, it will "remember" its initial shape and return to it without *any* guidance from an external force. This phenomenon has sparked a great deal of interest in a variety of different applications looking to utilize even the smallest untapped potential of the polymer.

Andreas Lendlein has completed two extensive literature reviews summarizing nearly 200 total articles dealing with shape-memory polymer research (Lendlein, 2002 and Lendlein, 2007). Topics reviewed include the many varieties in which SMP takes form, the physical and molecular mechanisms behind the shape-memory effect, the mechanical and thermal characteristics of SMPs and some of their current applications. While these reviews are an excellent source for nearly any question proposed about the mechanics and function of shape-

memory polymers, a few relevant pieces that pertain to the work covered in this thesis will be reviewed. Also provided is a review of literature that adds to the broad picture of why and where the work done in this thesis fits into the research spectrum.

2.1 BRIEF HISTORY

The shape memory effect was first observed in the 1930's in a pseudo elastic Gold-Cadmium (Au-Cd) alloy. The first commercially available shape-memory materials, however, were not developed until 1962-1963 by the Naval Ordinance Laboratory. These new shape memory materials were known as shape-memory alloys (SMAs) and were commercially marketed as Nitinol, a Nickel-Titanium alloy (Kauffman, 1993). SMAs generally have higher strength properties than shape memory polymers, but a few other factors make them unsuitable for application in a morphing aircraft wing. SMAs have a much higher density than SMP's and can achieve recoverable strains significantly lower than their polymer counterparts.

Shape-memory polymers were first introduced in 1984 by Nippon Zeon Co. in Japan. These polynorborene-based SMPs had a limited glass temperature transition range as well as limited manufacturability. It was not until a few years later that a subsidiary of Mitsubishi Heavy Industry developed the first polyurethane-based SMP, which is still the most widely used type of SMP (Liang 1997). Many variations now exist, each tailored to a different application throughout a huge variety of fields. Fields of study include biomechanics, smart structures, morphing aircraft, automobiles, actuation, and application in variety of material composites. There are also a variety of ways to activate the SMP, including: ambient heating, electrical heating, photo-thermal (laser) heating, light-activated heating, magnetically heating

through vibration, or actuating embedded conducting particles within the SMP. Many of these topics will be reviewed, as well as some of the most promising current research and application of shape-memory polymers. Relevant past research directly relating to the work done in this thesis will also be presented. This information will all be given in order of increasing relevance as it directly pertains to this thesis.

2.2 SIGNIFICANT SHAPE-MEMORY POLYMER APPLICATION

In the last few years, there has been an increasing attempt to utilize the full potential of shape memory polymers. SMPs are being studied for application in a variety of different fields. Mentioned next are a couple of the many emerging biomedical applications, which are among the most significant and valuable applications of shape-memory polymers. One noteworthy area of SMP biomedical research is in the improvement of current sutures. Lendlein and Langer (2002) created a smart degradable medical suture to be used in minimally invasive surgical procedures. The feasibility of the suture was validated by stretching SMP fibers in their heated state to three times their nominal length, letting them cool, then using them to loosely stitch a rat wound. The suture was then re-heated to its transition temperature, causing the thread to tighten and close the wound while applying an appropriate, controllable force of 0.1 N (Figure 2-1).

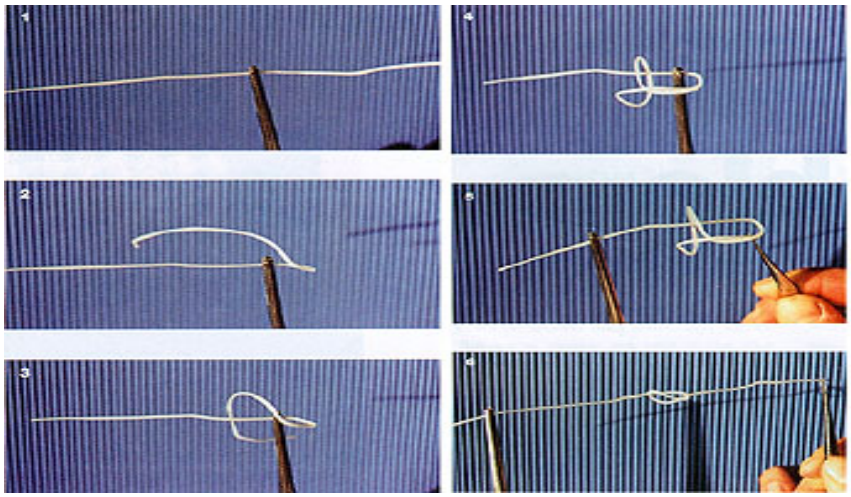

Figure 2-1 SMP suture going through stretching and re-heating process (Lendlein and Langer, 2002)

The possibility of using a shape memory polymer as a self-expandable stent (Figure 2-2) was also investigated (Wache, 2003). Current stents are usually made of metal and have several undesired side effects with blood or tissue. In an effort to solve this problem, Wache et al. conducted several *in vitro* tests. It was concluded that a shape memory polymer stent can solve many of the current complications associated with stent implanting and secondary effects incurred after surgery.

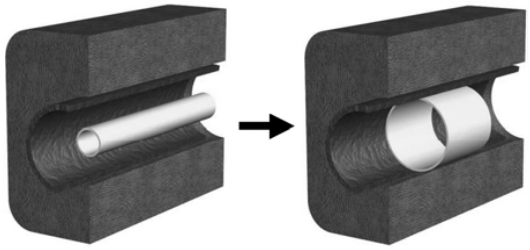

Figure 2-2 Model of SMP stent self-expanding in blood vessel (Wache, 2003)

The method was further investigated by implanting SMP stents in rabbits to confirm feasibility (Mei-Chin Chen, 2007). The implanted stent was found to be intact and functional without a thrombus (obstruction) formation after 24 hours.

Past work has also been done in a variety of smart structures. Smart materials and smart structures differ in a few ways, though both groups share the characteristic of being able to sense and respond to some kind of stimulus. The distinct difference between smart structures and smart materials lies in the method of control. Smart materials are intrinsically controlled through one or many of their characteristics inherent within the material and generally do not require external control. The biomedical applications that have been presented are good examples of this. Ideally a smart material would require no external stimulus when responding to environmental changes, but currently there are very few materials which can exhibit this behavior. A smart structure on the other hand is most generally thought of as a structure system that has embedded sensors and/or actuators and *is* usually externally controlled by a computer. Also, note that shape-memory polymers are intrinsically controlled insofar as they possess the controllability ability once the primary and secondary shapes have already been set.

2.3 MORPHING AIRCRAFT

One area of smart structure research and application that has received a great deal of attention is in the field of morphing aircraft structures (MASs), or morphing aircraft vehicles (MAVs). MAVs are single aircraft vehicles that are capable of changing shape in order to improve their performance over standard static design. The reasoning behind this advantage is

that since current aircraft are designed with a wing geometry that offers optimal performance at one critical stage of flight (and significantly lower performance at a different stage), morphing aircraft could offer optimal performance at multiple stages of flight. Located below (Figure 2-3) is a spider plot that attempts to graphically capture the advantage of morphing aircraft that has just been discussed.

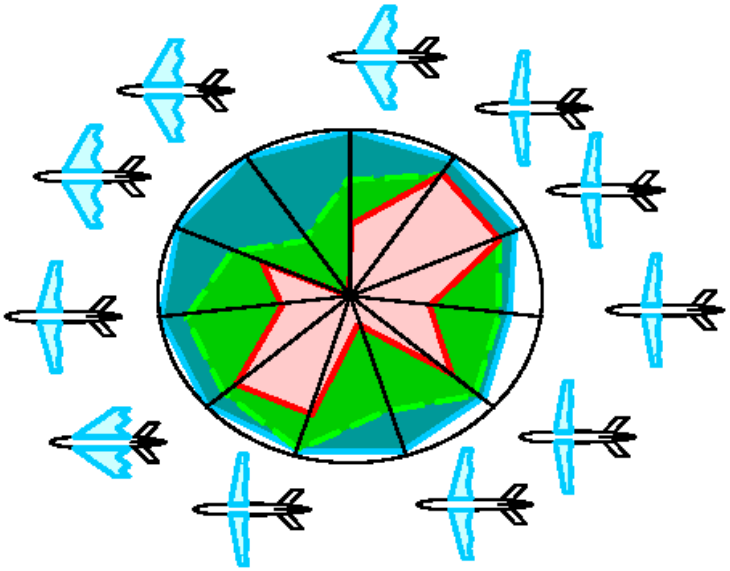

Figure 2-3 Qualitative spider plot (Bortolin, 2005)

The marked radii of the circle each represent a different stage of flight (take-off, landing, attack, etc.) while the wing orientation sketches on the ends of the radii represent the ideal wing configuration for the stage of flight. Note that the specific stage of flight is not marked since the plot applied generally to many aircraft and stages of flight. The inside areas of the circle represent efficiency during the stages of flight, such as aerodynamics, range, fuel economy and endurance. The blue area represents aircraft efficiency of a highly morphable aircraft at each corresponding wing orientation during the stages of flight. The blue area is the largest area since the aircraft would be able to achieve almost exactly the desired optimal wing configuration for each stage of flight. The green and red areas represent aircraft efficiency at

the same stages of flight *if* the aircraft were only able to partially morph or not morph at all, respectively. Note that the red area would correspond to current static aircraft and has extremely low performance at a few stages of flight and is unable to perform at one stage of flight. Again the specific stages of flight are not given in the spider plot, but the general depiction of efficiency for a morphing aircraft at different stages of flight are very representative. For example, an F-17 Nighthawk is not very fuel efficient when flying long distances due to its wing orientation. However, if the Nighthawk had morphable wings, it could fan its wings forward during long stages of flight to significantly improve fuel economy by improving its aerodynamics.

Figure 2-4 F-17 Nighthawk

The morphing mechanism of an MAV is generally a mechanical device embedded within the wing that is somehow linked to strategically placed actuators also located within the wing. The actuators and mechanical mechanisms are all encased in a skin designed to withstand the aerodynamic pressure loads that an aircraft sees in the air. The skin can be made of stretchable materials like silicon, or of two-state soft-hard materials like shape-memory

polymer. In the case of SMP skin, the actuators stimulate the memory material and the mechanical mechanism is then free to induce shape change. Generally the morphing material is softened upon receiving stimulus, kept soft during the shape-change process and then re-hardened after the shape-change is complete. Once ideal materials are found and implemented, MAVs have the potential to be able to morph into a variety of different configurations allowing for maximum efficiency throughout each stage of flight. Shown in Figure 2-5 below are a few airplanes that already use morphing methods.

Figure 2-5 Aircraft with variable sweep wings. Left to right: F-111, B-1, F-14 (Bortolin, 2005)

It is anticipated that eventually MASs will be lightweight, self-healing, aerodynamically efficient individual aircrafts that can adapt to multiple mission roles with the ability to autonomously control nearly every aspect of their geometry and function. Government agencies like NASA and particularly the Defense Advanced Research Project Agency (DARPA) have funded the majority of smart structure and morphing aircraft projects. The first in-depth look at the feasibility of a true morphing aircraft was completed in 2001. The

2-phase, 8-year program was funded by DARPA, NASA and AFRL and resulted in a full-scale SMA-activated morphing aircraft able to utilize over 70 different wing shapes. The wings contained 10 independent segments each consisting of a honeycomb arrangement of SMA material covered by a silicon skin. Deflection rates of over 80 degrees per second and maximum deflections of over 20 degrees were achieved (Kudva, 2004). Shown in Figure 2-6 below are a few of the wing shapes that could be achieved by actuating the different segments in the wing section. The maximum deflections of the morphing section of the wing as it dips down from the static part of the wing are also given.

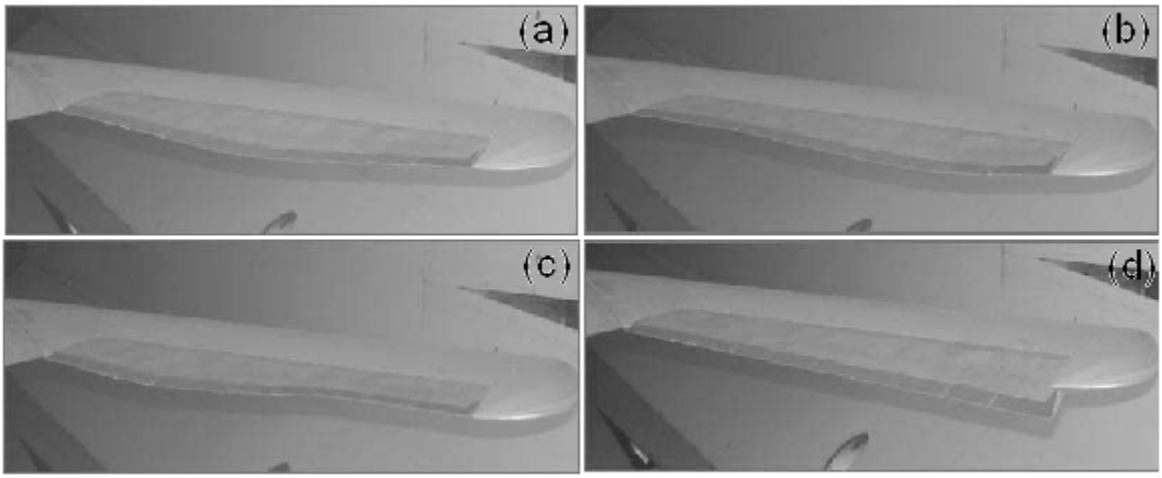

Figure 2-6 (a) 15° in center using segments 5 & 6, (b) 10° using segments 7 & 8, (c) 10° using segments 3 & 4 and (d) 20° using all Segments (Linear Variation) (Kudva, 2004)

Self-healing structures have also become an area of increasing interest in the research community, especially for use with morphing aircraft. Self-healing structures, as you would guess, are defined by having the ability to self-repair from an incurred wound. While most past research has resulted in poor findings, NextGen Aeronautics, The University of California and the US Army Aviation and Missile Research, Development and Engineering Center were

able to demonstrate a proof-of-concept self-healing prototype, which could also use the same mechanism to demonstrate morphing (Duenas et al.). The prototype was made of a mendomer, a variation of SMP material, with embedded magnetic particles used for activation. The mendomer was loaded with around 10% particle concentration, intentionally damaged and then inductively actuated to induce self-healing. It can be seen in Figure 2-7 that after exposure to heat for 2 minutes, the crack completely healed.

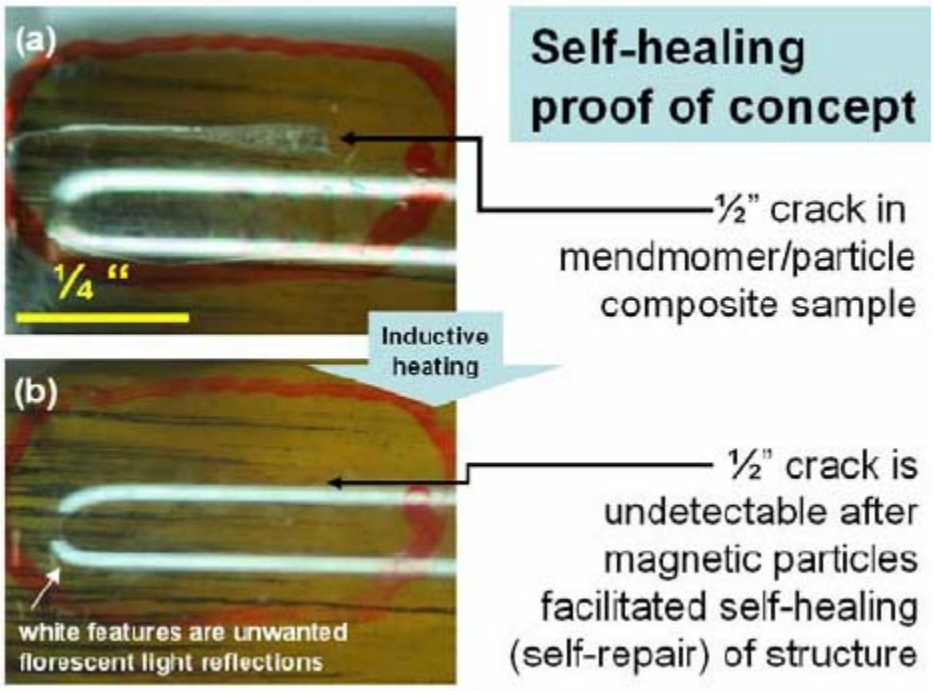

Figure 2-7 (a) sample with crack prior to healing and (b) sample after self-healing (Duenas et al.)

Upon further inspection using 100X magnification, there was no evidence of a previous crack. Although the glass-transition temperature and self-healing time need to be improved, this proof-of-concept is another example of the significance and versatility that SMPs posses.

While smart materials have to ability to improve a morphing aircraft and although they will most likely be used in final morphing designs, they aren't completely necessary. Several

attempts at demonstrating a morphing aircraft smart structure without the use of a smart material have been made by the University of Florida. A prototype morphing aircraft model, roughly the size of a medium-sized bird, was created using somewhat non-conventional methods. As opposed to most morphing aircraft designs, the focus of this morphing aircraft design was on alterations to the wing that could utilize dynamic control (Abdulrahim, 2005). The prototype aircraft is able to utilize both active and quasi-static forms of morphing using actuators located on the wing as well as a thin, flexible wing. Twisting motion in the wingtips is achievable for roll control. A bird-like "craning" motion is also achievable by pulling the wings inward during flight via built-in actuators (Figure 2-8).

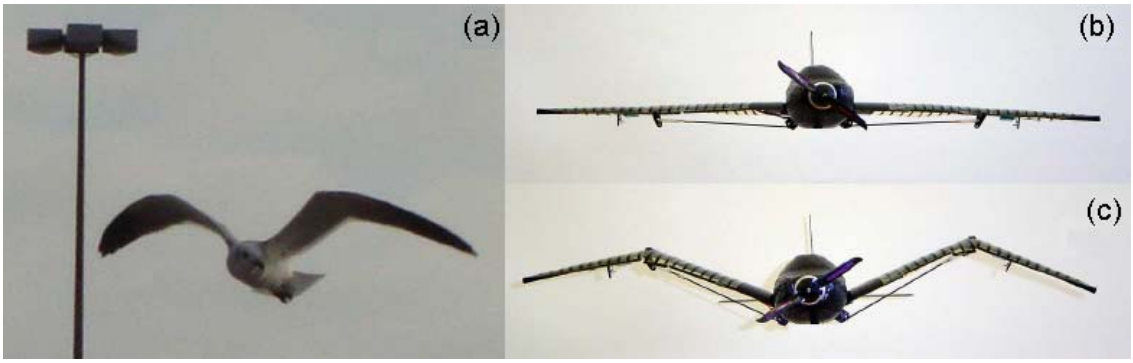

Figure 2-8 (a) Seagull demonstrating wing craning, (b) prototype morphing aircraft in nominal configuration and (c) aircraft in craning position (Abdulrahim, 2005)

There are a number of studies also investigating various morphing concepts to be used in wing design. Among the many methods of wing morphing include camber change, wing twist, wing sweep change and wing span change (Bae, 2007). Though wing span change is the type of morphing that this thesis pertains to, SMPs could potentially be used in each of the mentioned concept designs.

Smart structures are also being considered as a means to improve current space cargo shortcomings. SMP foam, shape-memory polymer in open cellular form, has been investigated as a method to improve feasibility of deployable structures used in space. A functional deployable structure could dramatically cut the cost of sending structures to space by significantly reducing space-bound cargo weight and volume. Cold hibernated elastic memory (CHEM) has been investigated as a method to package these deployable structures. The idea is that a CHEM structure would be created and bundled here on Earth, subsequently shuttled to space and then remain in space as a condensed structure until activated for deployment as needed. It was found through experimental testing that a CHEM polyurethane foam, with 93.4% strain, could expand up to 1273% against a 1 N load. While an increase in the load dramatically reduced the expansion rate, it was found that the strain was fully recoverable against a 1 N load even after a hibernation period of two months (Tey, 2001). These findings suggest that SMP foam, though likely in a further stage of development, could be a very valuable material in deploying large structures in space that function in a passive state, e.g. a satellite.

2.4 METHODS OF ACTIVATING SHAPE-MEMORY POLYMERS

Several methods of triggering the memory effect in shape-memory polymers have been developed. The most common and probably the easiest triggering method to actually implement is by the use of heat (thermal activation). Activation through heat was the first method discovered as a way to induce shape change in shape-memory polymers and has subsequently had a few modifications. Thermal activation can be subdivided into a few more

specific methods of activation - electrical heating, ambient heating and photo-thermal heating. Electrical heating, the most commonly used method to heating, and ambient heating, mostly used in experimental analysis, have already been overviewed and are explained in further detail later in this thesis. Photo-thermal heating, or laser heating, is most applicable for small-scale shape-memory polymers. Maitland et al. (2007) successfully demonstrated a prototype laser-activated SMP foam device for use in aneurysm treatment. A hollowed out SMP foam spheroid was collapsed into a secondary cylindrical shape, and then laser-activated back to its nominal shape using a 1 - 8.6 Watt laser.

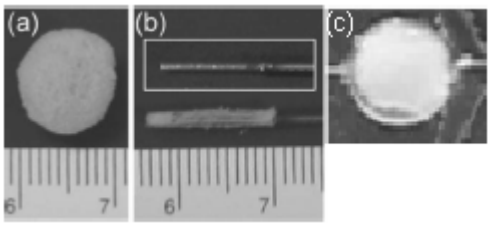

Figure 2-9 SMP Foam in (a) nominal spheroid state, (b) secondary cylindrical state and (c) final state (Maitland et al., 2007)

With no simulated flow inside the modeled aneurysm, the SMP foam sample fully re-expanded within 60 seconds. Note that an optical fiber was embedded inside the spheroid for increased light absorbance. Viability of laser-heated SMPs have also been demonstrated, but to be used in thrombus removal, a procedure needed to unclog obstructed blood vessels (Small, 2005). A shape-memory polymer sample was cast into a corkscrew shape to set its nominal shape and then manually straightened into a secondary rod shape. Although only preliminary testing was conducted, the idea was that the SMP rod would be inserted into a vein, via a catheter,

penetrating the thrombus occlusion. The rod would then be hit with a laser, activating it back to its corkscrew shape, and pulled out of the vein along with the thrombus.

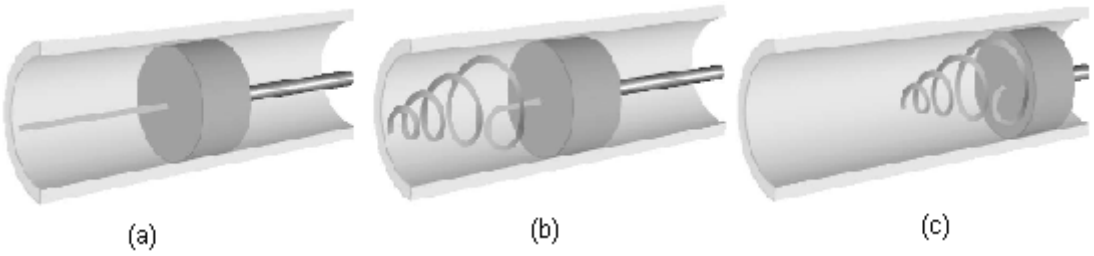

Figure 2-10 Thrombus removal process, from (a) to (c), using the SMP "micro-actuator" (Small, 2005)

Testing *in vitro* showed that a 4 centimeter SMP rod was successfully able to fully deploy into a corkscrew shape in just 5 seconds upon activation from a 1 Watt laser.

Light-activation is another promising method for stimulating shape-memory polymers back to their nominal state. Lendlein at. al. (2005) stretched a polymer film to 120% of its nominal length, irradiated it with ultraviolet light for 60 minutes and then released the external force. The sample kept its shape until being irradiated again for 60 minutes, after which it returned to its nominal state. Another noteworthy finding was the effect caused by applying irradiation to only partial sections of the polymer film sample. As shown below in Figure 2-11, applying irradiation to only the top side of the sample created a corkscrew shape.

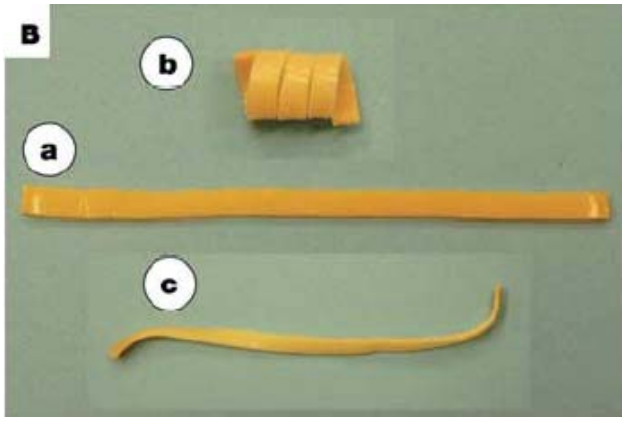

Figure 2-11 (a) Sample in initial state, (b) sample after applied UV irradiation to only the top side and (c) polymer after returning to initial state via more UV (Lendlein et al., 2005)

Magnetically activated shape-memory materials exist in several forms. Homogeneously ferromagnetic shape-memory materials can achieve strains on the order of 10% through an applied magnetic field and no external force. Note that these materials are not polymers and are not in the same family as SMPs in the sense that has been used. Shape-memory polymers with embedded magnetic particles or embedded carbon nanotubes have also been investigated for the same application and shown to be effective (Conti, 2007 and Lendlein, 2007). Magnetic activation is achieved by applying an alternating magnetic field to induce heating through friction in the particles. A shape-memory polymer loaded with ferromagnetic particles (~7% concentration) was successfully found to reach glass transition temperature, allowing it to shape-change back to its nominal state (Schmidt, 2005).

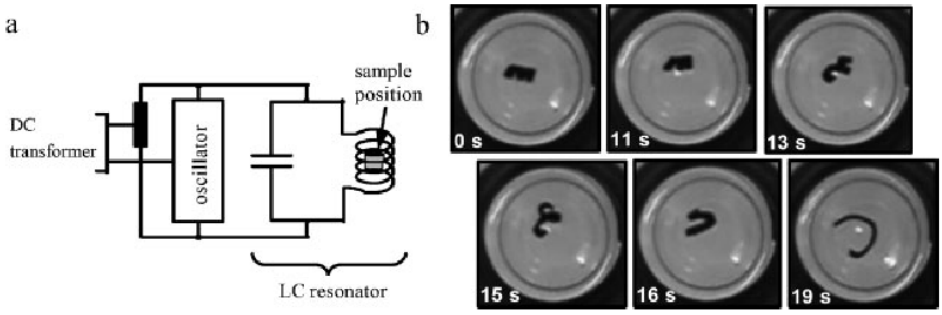

Figure 2-12 (a) Schematic of alternating magnetic field generator and (b) accompanying shape change (Schmidt, 2005)

The embedded particles had a negligible effect on the SMP transition temperature and only a small effect on the nominal polymer modulus (Buckley, 2006).

Another method of activation is through the absorption of water. It has been found that the glass transition temperature of shape-memory polymer can be lowered significantly by submersing it in water, thereby functioning as a means of activation. Several tests were done to verify and quantify this finding (Huang Yang, 2005). An SMP fiber was bent into a circular shape and cooled to set the secondary shape. After immersing the fiber in water at standard conditions for about 140 minutes, shape change occurred till the fiber nearly reached its nominal cylindrical shape.

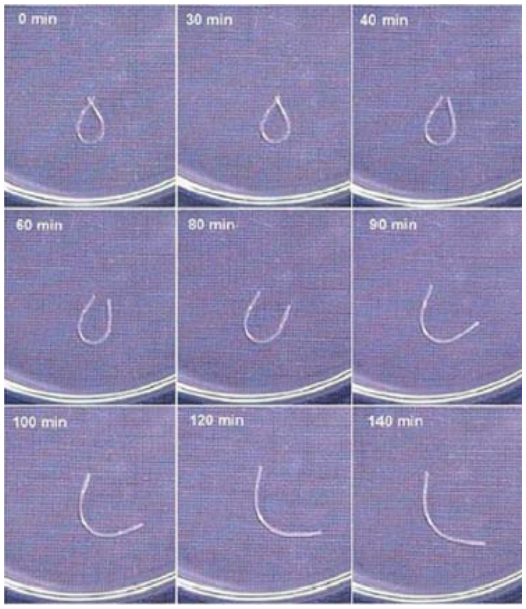

Figure 2-13 Shape-memory polymer undergoing water-driven recovery

Concluding, there are currently many ways to induce the shape-memory effect in shape-memory polymers each with advantages and disadvantages. To help give a clearer understanding of the methods of activation, three groups are formed. The first group includes only methods that use direct thermal application. Electrical heating, laser heating and ambient heating all fall into this category. The second group includes only methods that use *indirect* thermal application. Subsets of this method include embedded conducting particles or carbon nanotubes, embedded magnetic nanoparticles and water activation. The third category, which can not really be called a group, consists solely of light-induced activation. The light-induced shape-memory effect is independent of temperature and therefore deserves separation from the other two categories.

2.5 SHAPE MEMORY POLYMER CHARACTERISTICS

There has been extensive quantification of both the thermal and the mechanical characteristics of shape-memory polymers. With the large variety of SMP materials, methods of activation and applications, the task of reviewing them all seems impossible. Lendlein, however, reviewed nearly 200 articles in an effort to do so. Therefore, I'll mention only several of the most relevant characteristics and procedures used in finding them.

Gall et al. found that the isothermal free stain recovery rate was found to increase with increasing temperature or decreasing pre-deformation temperature. It was also found that the SMP was able to strain up to 80% and show 100% strain recovery. A prototype, intended for biomedical application, was created to demonstrate the SMP characterization findings.

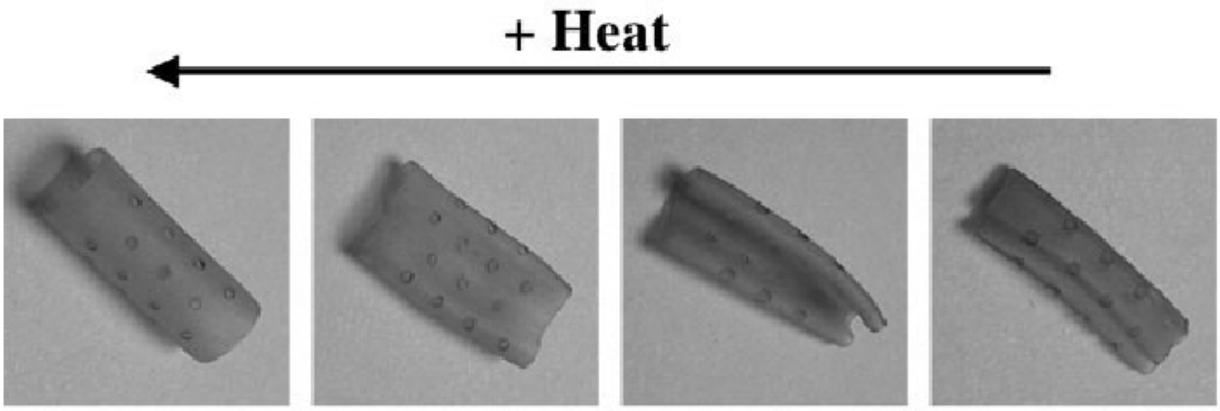

Figure 2-14 Prototype SMP stent exhibiting memory effect (Gall et al., 2005)

Keihl et al. investigated the mechanical properties of an SMP to determine its feasibility for application in morphing aircraft. This SPIE paper (Keihl, 2005) and the relating thesis (Bortolin, 2005) are by far the most relevant pieces of literature pertaining to this thesis.

As a result, I'll be referencing them both throughout this thesis as means for comparison and contrast. In brief summary, Bortolin cut out 4 x 4 x .127 in. squares of SMP from larger SMP sheets, attached them in custom shear-inducing fixtures and conducted tests mimicking the shape change needed for a common morphing wing. Ambient heating via an oven was used as the method of activation. It was found that significant out-of-plane deformation occurred during the shear tests and so a test rig was used to uni-axially pre-strain the other specimens (Figure 2-15) in an effort to reduce or eliminate the out-of-plane deformation.

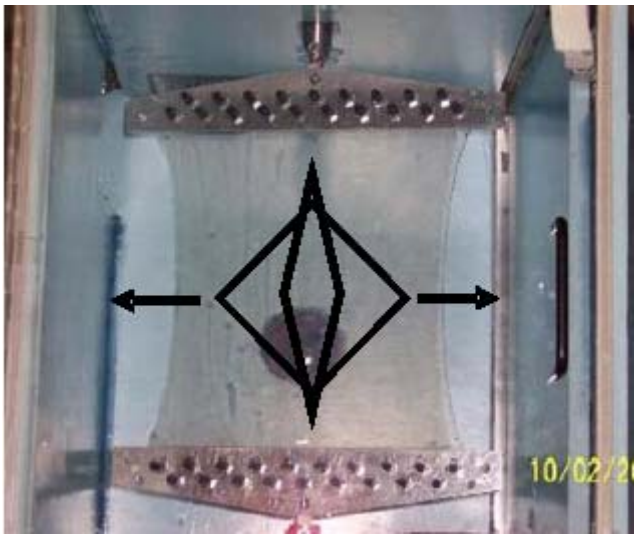

Figure 2-15 Bortolin's prestrained specimen in test rig (Bortolin, 2005)

Post test observations and data acquisition readings were focused on stress-strain relationships; there were no aerodynamic simulations created to quantify real-world performance. Samples were pre-strained different percentages and the effect of out-of-plane deformation, attributed to buckling, was quantified. Finite element models were also created in ABAQUS to determine theoretical buckling load values. The conclusions of the work noted that "complete control of buckling was not realized" and it was suggested that bi-axial pre-strain may be an answer to the

problem. Although this work is similar to what is covered in this thesis, the procedure, testing, theoretical analysis and results all differ in many ways. This thesis will also contribute a significant amount of additional material.

3.0 BACKGROUND INFORMATION

Background information of a previous shape-memory polymer pixel tile design is given as well as information about Veriflex and nickel-chromium wire, the two primary materials used in this thesis.

3.1 PREVIOUS SMP TILE DESIGN

In line with the recent surge of morphing aircraft research and development, this thesis was conducted to further determine the feasibility of a sweeping-style morphing aircraft wing. The skin of the wings was to be comprised of an array of interlocking tiles (Figure 3-1) that moved in unison to produce the shape change of the wing.

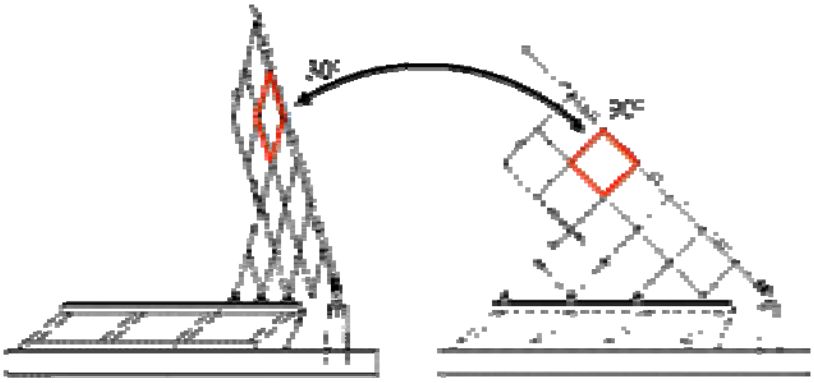

Figure 3-1 Shape change process of a morphing wing containing interlocking tiles. The slider bar on the bottom moves the linkages, causing the tiles to change shape.

The tiles (Figure 3-2) are set to contain two materials: thermally activated SMP acting as a membrane, and fibers located within the SMP membrane acting as both heating elements and structural reinforcement.

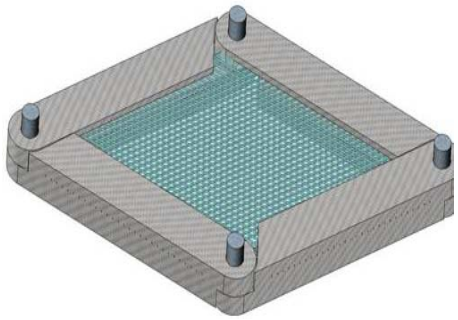

Figure 3-2 SolidWorks representation of a single tile from the tile array in the wing: the green inside represents SMP, while the thin black lines represent the wire fibers.

Shape change of the morphing wing occurs in 3 steps. The wing is initially in a rigid state. First, the SMP membrane is softened via applied current to the heating elements, leaving the wing skin in a flexible state. Next the configuration of the tiles is changed using a sliding bar and linkages connected to the array of tiles. Finally, power to the heating elements is removed, causing the SMP to cool and harden, and the wing is set in its new shape. The process can be repeated as necessary to achieve desired degrees of wing sweep.

There are a few problems and concerns associated with the proposed process that need to be addressed.

- The most obvious of these concerns is whether or not the SMP/fiber composite will withstand aerodynamic loads. In its hard state, SMP will experience a negligible amount of out-of-plane deformation caused by aerodynamics loads,

but the SMP requires some reinforcement to hold up to the loads while in its soft state.

- There is also a possibility that shearing of the tiles will compromise the structural integrity of the SMP membrane by causing it to buckle. This is confirmed and addressed later in the thesis.
- Another foreseeable problem is the possibility of large out-of-plane deformations between the fibers embedded in the SMP. This is referred to as "pillowing" and is also addressed later in this thesis, though it is found to be inconsequential.

3.2 VERIFLEX

Veriflex, a polymer commercially manufactured by a spin-off company of Cornerstone Research Group (CRG) called CRG Industries, LLC, is the shape-memory polymer that is used extensively in this thesis. Veriflex is a two-part (1 part catalyst, 24 parts resin) shape-memory polymer resin system. Once heated above its activation temperature, Veriflex changes from a rigid polymer to a very elastic state. While in its elastic state, it can be deformed via twisting, pulling, bending or stretching to an elongation of up to 200%. If the polymer is cooled while in this deformed state, it will harden and maintain its new configuration indefinitely. Upon being reheated to its activation temperature again, the polymer will return, without manipulation, to its initial state in which it was cured. The process is indefinitely repeatable without loss of memory effect or strength. Standard Veriflex, which is used in this thesis, has a glass transition temperature of 62^{o}C. Typical mechanical properties of standard Veriflex are

given below in Table 3-1. Experimentally found mechanical properties for Veriflex in its elastic state are given in Table 3-2. A qualitative graph representing the storage modulus of Veriflex versus its temperature are also given below in Figure 3-3.

Table 3-1 Mechanical properties of Veriflex (CRG Industries, LLC, 2008)

	Mechanical Properties	**Specifications ($T < T_g$)**
ASTM D 638	Tensile Strength	22.96 Mpa
ASTM D 638	Tensile Modulus	1241.05 Mpa
ASTM D 638	Elongation to break	3.90%
ASTM D 790	Flexural Strength	31.72 Mpa
ASTM D 790	Flexural Modulus	1241.05 Mpa
ASTM D 695	Compressive Strength	32.41 Mpa
ASTM D 695	Compressive Modulus	1447.90 Mpa
	Thermal Conductivity	0.17 W/(m*K) at 18.6 ºC
	Material density	0.92 g/cm^3 or 920 kg/m^3

Table 3-2 Experimentally determined Young's Modulus for Veriflex (Beblo, 2006)

Axial E (Mpa)		Transverse E (Mpa)	
T < Tg	T > Tg	T < Tg	T > Tg
23 °C	80 °C	23 °C	80 °C
1050	0.24	1050	0.24

The long cure cycle for standard Veriflex (as suggested by CRG Industries) requires that the combined 2-part resin be heated to 75^{o}C for 36 hours. This is the cure cycle that will be used throughout this thesis unless otherwise noted. Note that after hand-mixing the two-part Veriflex resin, it was placed into a vacuum chamber prior to pouring to remove air bubbles.

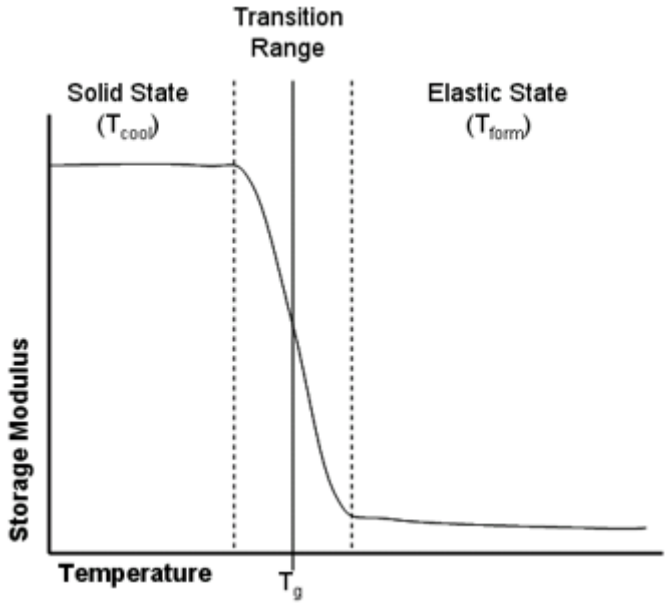

Figure 3-3 Qualitative graph representing strength of Veriflex vs. its temperature

3.3 NICKEL-CHROMIUM (NICHROME) WIRE

Nickel-chromium (Nichrome) wire, an alloy commonly used in heating devices, is used extensively in this thesis as the material for the embedded fibers located within the SMP. The fibers function as reinforcement as well as a method of heating the SMP. There are a variety of material and heating characteristics inherent to Nichrome wire that need to be addressed and adapted for use in the SMP.

Generally speaking, Nichrome wire increases in temperature as electrical power is supplied. As a supplied current travels through the Nichrome wire, the resistance in the wire creates a voltage drop and, in turn, heat (or from Ohm's Law, $P = I^2 * R$). Listed below in Table 3-3 (MOR Electric Heating Assoc., Inc., 2008) is a chart giving required current values to produce a corresponding temperature value for a large range of wire diameters in free air.

Table 3-3 Nichrome in free air electrical properties chart (MOR Electric Heating Assoc., Inc.)

CURRENT TEMPERATURE CHARACTERISTICS OF NICHROME 60 STRAIGHT WIRE Showing approximate amperes necessary to produce a given temperature. Applying only to straight wires stretched horizontally in free air.								
AWG (Gauge)	**Dia."**	**Temp. 400F Temp. 204C**	**600 316**	**800 427**	**1000 538**	**1200 649**	**1400 760**	**1600 871**
10	.102	15.43	22.03	28.15	35.63	44.30	54.39	65.08
11	.091	13.23	18.72	23.89	30.16	37.54	46.07	55.15
12	.081	11.34	15.91	20.27	25.53	31.77	39.03	46.73
13	.072	9.73	13.53	17.21	21.61	26.89	33.06	39.60
14	.064	8.34	10.50	14.59	18.30	22.76	28.01	33.56
15	.057	7.15	9.78	12.38	15.50	19.26	23.73	28.44
16	.051	6.13	8.31	10.50	13.11	16.30	20.10	24.10
17	.045	5.31	7.18	9.13	11.30	13.90	16.90	20.30
18	.040	4.66	6.26	7.90	9.75	11.96	14.51	17.37
19	.036	4.09	5.46	6.84	8.41	10.30	12.45	14.87
20	.032	3.58	4.77	5.92	7.25	8.86	10.69	12.72
21	.0285	3.14	4.16	5.13	6.26	7.63	9.17	10.88
22	.0253	2.76	3.63	4.44	5.40	6.56	7.87	9.31
23	.0226	2.42	3.16	3.84	4.67	5.65	6.76	7.97
24	.020	2.12	2.76	3.32	4.01	4.86	5.80	6.82
25	0179	1.84	2.42	2.90	3.44	4.15	4.97	5.86
26	.0159	1.58	2.09	2.52	3.00	3.61	4.31	5.06
27	.0142	1.37	1.80	2.19	2.62	3.14	3.73	4.37
28	.0126	1.18	1.55	1.90	2.28	2.73	3.23	3.77
29	.0113	1.02	1.34	1.65	1.99	2.37	2.80	3.25
30	.010	.875	1.16	1.43	1.74	2.06	2.43	2.81
31	.0089	.754	1.00	1.24	1.51	1.79	2.10	2.42
32	.008	.650	.860	1.08	1.32	1.56	1.82	2.09
33	.0071	.560	.750	.940	1.13	1.34	1.56	1.80
34	.0063	.493	.658	.820	.978	1.16	1.34	1.54

The resistance of the wire is a function of its diameter and length, and via Ohm's Law, the required voltage is then V=IR. In application of these mentioned properties, a desired temperature would be produced by applying the appropriate current or applying a voltage equal to the appropriate current times the total wire resistance. There is one small step needed, however, before the current/temperature chart can be put to use. Since the maximum working temperature of Veriflex is 135^{o}C, the temperature of the Nichrome wire also needs to be kept below 135^{o}C to prevent damage to the Veriflex during the heating procedure. The chart does not include the needed temperature of 135^{o}C and so a simple extrapolation is used.

Using the Nichrome electrical data from Table 3-3, a plot (Figure 3-4) was generated to show how much electrical current needed to be applied to a Nichrome wire to produce a given

temperature. A 2nd order polynomial trendline relating temperature and current was created for a range of the most likely gauge diameter candidates.

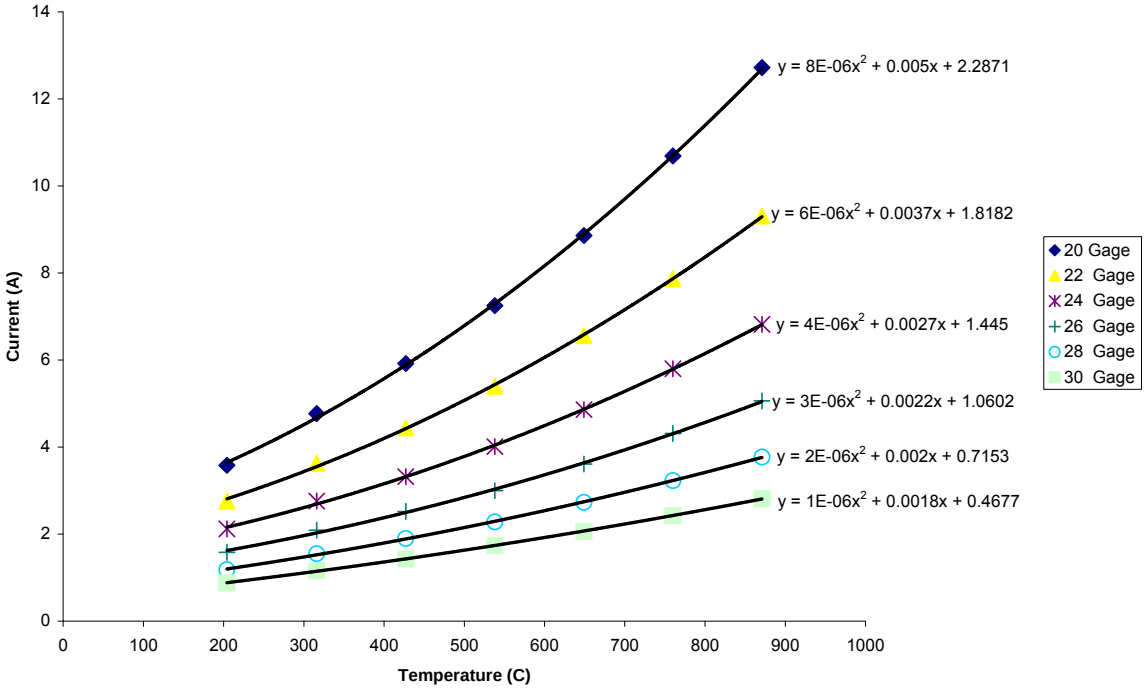

Figure 3-4 Plot showing currents required to achieve a given temperature at a given gage size

Gauge sizes within the determined relevant range for the Nichrome wire were plotted, and all R^2 values for the resulting trendline equations were at least .999. This procedure could be easily applied to any other gage size, but for the sake of readability and realized relevance resulting from iterative ANSYS testing mentioned later, gauge sizes were kept between 20 and 30 (or .036" and .0113"). Also, according to MOR Electric Heating Assoc., Inc., a smaller diameter wire corresponds to both faster heating of the wire itself and also lower required power. The downside to a smaller wire is that it does not produce as much heat, shown later during ANSYS modeling. So the wire needs to be small, but not too small.

Using the equations located in Figure 3-4, the current required to achieve a temperature of 135°C was found in each of the plotted gauge diameters (Table 3-4).

Table 3-4 Current required to achieve 135°C for given wire diameters

AWG (Gauge)	Diameter (inches)	Required Amps for 135°C
20	0.032	3.1079
22	0.0253	2.4271
24	0.02	1.8824
26	0.0159	1.4119
28	0.0126	1.0218
30	0.01	0.72893

Other general properties of the Nichrome wire used are listed below in Table 3-5.

Table 3-5 Properties of Nichrome wire at given diameters at standard pressure and temperature

AWG (Gauge)	Diameter (inches)	Resistance (Ohms/m)	Density (kg/m^3)	Thermal Conductivity (W/m/°C)	Specific Heat (J/kg/°C)	Modulus of Elasticity (Gpa)
20	0.032	2.163	8300	13.2	450	186
22	0.0253	3.461	8300	13.2	450	186
24	0.02	5.482	8300	13.2	450	186
26	0.0159	8.759	8300	13.2	450	186
28	0.0126	13.95	8300	13.2	450	186
30	0.01	21.94	8300	13.2	450	186

Using the required current values from Table 3-4 and the resistance values from Table 3-5, the power required to heat a given diameter wire to 135°C is shown below in Table 3-6. Power was calculated using $P = I^2 * R$. Note that in order to find energy, these power numbers need to be multiplied by the time over which the Nichrome is heated. This is done later when determining the power requirements associated with heating the SMP plate.

Table 3-6 Power required to heat given lengths of Nichrome wires to 135°C

AWG (Gauge)	Diameter (inches)	Power required to heat Nichrome wire to 135°C (Watts)			
		1 meter	2 meters	3 meters	4 meters
20	0.032	20.89	41.79	62.68	83.57
22	0.0253	20.39	40.78	61.16	81.55
24	0.02	19.43	38.85	58.28	77.70
26	0.0159	17.46	34.92	52.38	69.84
28	0.0126	14.56	29.13	43.69	58.26
30	0.01	11.66	23.32	34.97	46.63

These power requirement numbers assume that the Nichrome wire is in free air at standard temperature and pressure. Also, since the Nichrome wires heat up to temperature almost immediately, these power requirements would correspond to the power input to the Nichrome required to keep the wires at 135°C. These power numbers will be used and adapted later when determining final power requirements associated with heating an SMP plate via embedded Nichrome fibers.

4.0 ANALYTICAL MECHANICAL MODELING

In order to determine which values of each parameter are needed to achieve desired results, several models are created to predict final deflections. The models will be addressed as three separate endeavors. The first model will be developed to find a surface deflection map of the fiber-embedded SMP (FESMP) tile in its un-heated, un-sheared and heated, un-sheared states as it undergoes a uniform pressure load. The second model will be used to capture the "wrinkling" effect of the tile as it is sheared into its skewed rhombic state. The third model, a combination of the previous two, will be used to find the surface deflection map of the sheared tile as it undergoes a uniform pressure load.

4.1 DEFLECTION MODEL FOR FESMP TILE

The surface deflection map of the fiber-embedded SMP tile in its un-sheared configurations was found using several methods. First, plate theory was used to create a surface plot of the deflection of the tile as caused by a transverse pressure load. The material properties of the plate were then altered to accommodate the unidirectional embedded fibers. Since the composite plate model couldn't incorporate the tension of the fibers, the tension was indirectly related to the strength of the fibers. This was done by relating the tensioned wire to the bending rigidity of an equivalent plate layer. The effective modulus of the fibers was then

found by relating the tension in the wire to the transverse deflection of the effective plate layer. The maximum deflection of the tile is then plotted versus overall modulus of the FESMP tile, including both the modulus of SMP and modulus of the fiber as a function of tension. This was all done in several steps as shown below.

4.1.1 Generating stress and strain equations

A three-dimensional model of the fiber-embedded shape-memory polymer plate undergoing a uniform pressure load is created using plate theory (Ugural, 1981 and Reddy, 1997).

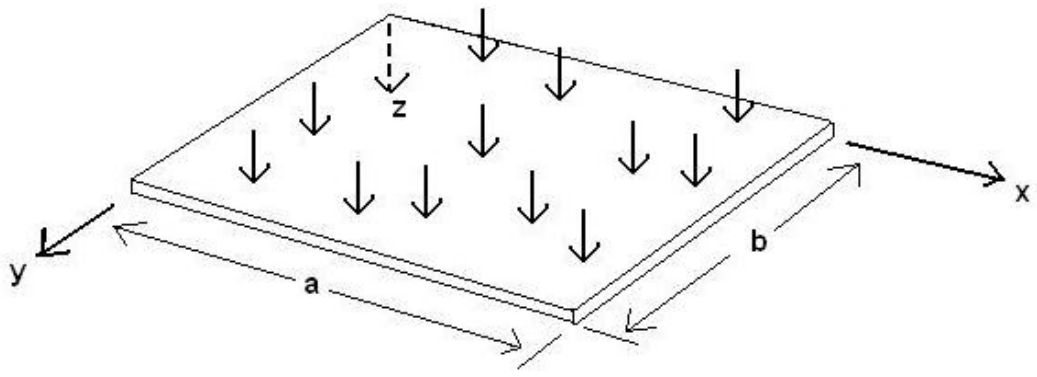

Figure 4-1 Plate undergoing uniform pressure load

The strain energy stored in an elastic body, for a general state of stress, can be given by

$$U = \frac{1}{2}\iiint_V \left(\sigma_x\varepsilon_x + \sigma_y\varepsilon_y + \sigma_z\varepsilon_z + \tau_{xy}\gamma_{xy} + \tau_{xz}\gamma_{xz} + \tau_{yz}\gamma_{yz}\right)\, dx\ \ dy\, dz \qquad (4.1)$$

Where,

σ_i = Stress in the i-direction

ε_i = Strain in the i-direction

τ_{ij} = Shear stress in the ij-direction

γ_{ij} = Shear strain in the ij-direction

In order to simplify the above equation, some background fundamental theory is required. As per the fundamental assumptions for small deflection plate theory of bending, the plate is assumed to be under the following conditions:

1. The deflection of the mid-surface is small compared with the thickness of the plate. This means that the square of the slope is a negligible quantity.
2. The mid-plane remains unstrained subsequent to bending.
3. Plane sections initially normal to the mid-surface remain normal to that surface after bending. This means that the strains γ_{xz} and γ_{xz} will be negligible as well as normal strain ε_z.
4. The stress normal to the mid-plane, σ_z, is small compared to the other stress components and may be neglected. This becomes less valid as loads become more concentrated.

As a consequence of these assumptions, the strain-displacement relations can be reduced to (4.2 - 4.7). Note that subscripts on the right side of the equations denote differentiation, e.g., $R_{,ij} = \frac{\partial R}{\partial i}\frac{\partial R}{\partial j}$.

$$\varepsilon_x = u_{,x} \qquad \varepsilon_y = v_{,y} \qquad \varepsilon_z = u_{,z} = 0 \qquad (4.2 - 4.4)$$

$$\gamma_{xy} = u_{,y} + v_{,x} \qquad \gamma_{xz} = w_{,x} + u_{,z} = 0 \qquad \gamma_{yz} = w_{,y} + v_{,z} = 0 \qquad (4.5 - 4.7)$$

Where,

u = component of displacement in the x direction

v = component of displacement in the y direction

w = component of displacement in the z direction

With w = w (x, y) and an applied downward load, integration over z of the expressions for γ_{xz} and γ_{yz} gives

$$u = -z \cdot w_x + u_0(x, y) \tag{4.8}$$

$$v = -z \cdot w_y + v_0(x, y) \tag{4.9}$$

Since $u_0(x, y)$ and $v_0(x, y)$ represent the values for u and v on the mid-plane of the plate, and by assumption (2) above, u and v can be reduced to:

$$u = -z \cdot w_x \tag{4.10}$$

$$v = -z \cdot w_y \tag{4.11}$$

Substituting (4.10-4.11) into (4.2, 4.3 and 4.5) yields the following expressions for strain:

$$\varepsilon_x = -z \frac{\partial^2 w}{\partial x^2} \tag{4.12}$$

$$\varepsilon_y = -z \frac{\partial^2 w}{\partial y^2} \tag{4.13}$$

$$\gamma_{xy} = -2z \frac{\partial^2 w}{\partial x \, \partial y} \tag{4.14}$$

Using the fundamental assumptions for small-deflection plate theory, the generalized Hooke's Law equations for relating stress and strain are

$$\varepsilon_{\mathrm{x}} = \frac{1}{\mathrm{E_x}}\left[\sigma_{\mathrm{x}} - \nu_{12}\left(\sigma_{\mathrm{y}} + \sigma_{\mathrm{z}}\right)\right] \tag{4.15}$$

$$\varepsilon_{y} = \frac{1}{E_{y}}\left[\sigma_{y} - \nu_{12}\left(\sigma_{x} + \sigma_{z}\right)\right] \tag{4.16}$$

$$\gamma_{\mathrm{xy}} = \frac{\tau_{\mathrm{xy}}}{\mathrm{G}_{12}} \tag{4.17}$$

4.1.2 Altering material properties to accommodate unidirectional fibers

Here it becomes necessary to distinguish between a completely isotropic material and a unidirectional fiber-reinforced lamina containing an isotropic matrix and isotropic fibers.

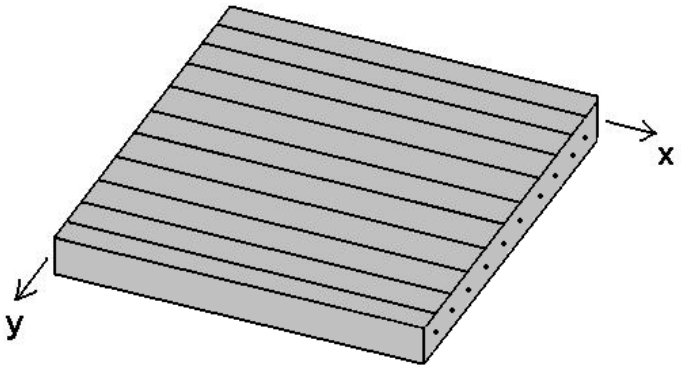

Figure 4-2 Fiber-reinforced plate

The following assumptions have to be made about the interaction of the wire fibers with the SMP plate:

1. The fiber and the matrix are perfectly bonded together, rendering the deflections in those surrounding areas of SMP equal to the deflection of the fiber.
2. The fibers are parallel and uniformly distributed through the matrix.

3. The matrix is free of all voids.
4. The fibers and matrix and both isotropic and adhere to Hooke's Law.
5. The applied loads are either parallel (fiber tension) or perpendicular (transverse pressure) to the fiber direction.
6. The areas of SMP in between fibers experience a negligible amount of deflection as compared to the overall surface deflection, i.e. no pillowing in between the fibers. This will be modeled to confirm that this is true.

The fiber-reinforced material properties, used in (4.15 - 4.17), can now be expressed in terms of the fiber properties, matrix properties and volume fractions in (4.18a - 4.18h) below (Jones, 1999). Note that the fiber direction is along the x-direction.

$$E_x = E_f V_f + E_m V_m \qquad E_y = \frac{E_f E_m}{E_f V_m + E_m V_f} \qquad (4.18a - b)$$

$$G_{12} = \frac{G_f G_m}{G_f V_m + G_m V_f} \qquad \nu_{12} = \nu_f V_f + \nu_m V_m \qquad (4.18c - d)$$

With,

$$G_f = \frac{E_f}{2(1+\nu_f)} \qquad G_m = \frac{E_m}{2(1+\nu_m)} \qquad (4.18e - f)$$

$$V_f = \frac{\pi \cdot r^2 \cdot a \cdot N}{t \cdot a \cdot b} \qquad V_m = 1 - V_f \qquad (4.18g - h)$$

Where,

E_f = modulus of fiber

E_m = modulus of matrix

ν_f = Poisson's ratio of fiber

ν_m = Poisson's ratio of matrix

V_f = volume fraction of fiber

V_m = volume fraction of matrix

E_x = longitudinal modulus of fiber-reinforced composite

E_y = transverse modulus of fiber-reinforced composite

G_m = shear modulus of SMP matrix

G_f = shear modulus of Nichrome fibers

G_{12} = shear modulus of fiber-reinforced composite

$\nu_{12} = \nu$ = Poisson's ratio of fiber-reinforced composite

r = radius of fiber

N = number of fibers contained in FESMP plate

t = thickness of FESMP plate

a = length of FESMP plate

b = width of FESMP plate

Setting (4.12 - 4.14) equal to (4.15 - 4.17), respectively, and solving for the stress components yields stress in terms of elastic modulus and transverse deflection:

$$\sigma_x = \frac{-z}{1-\nu^2}\left(E_x w_{xx} + \nu \cdot E_y w_{yy}\right) \tag{4.19}$$

$$\sigma_y = \frac{-z}{1-\nu^2}\left(E_y w_{yy} + \nu \cdot E_x w_{xx}\right) \tag{4.20}$$

$$\tau_{xy} = -2 \cdot z \cdot G_{12} w_{xy} \tag{4.21}$$

Substituting (4.19 - 4.21) into (4.15 - 4.17) gives strain in terms of elastic modulus and transverse deflection, as shown below in (4.22 - 4.24).

$$\varepsilon_x = \frac{1}{E_x}\left[\frac{-z}{1-\nu^2}\cdot\left(E_x w_{xx} + \nu\cdot E_y w_{yy}\right) + \nu\frac{z}{1-\nu^2}\left(E_y w_{yy} + \nu\cdot E_x w_{xx}\right)\right] \tag{4.22}$$

$$\varepsilon_y = \frac{1}{E_y}\left[\frac{-z}{1-\nu^2}\cdot\left(E_y w_{yy} + \nu\cdot E_x w_{xx}\right) + \nu\frac{z}{1-\nu^2}\left(E_x w_{xx} + \nu\cdot E_y w_{yy}\right)\right] \tag{4.23}$$

$$\gamma_{xy} = -2\cdot z\cdot w_{xy} \tag{4.24}$$

Substituting the stress (4.19 - 4.21) and strain (4.22 - 4.24)) components into the original strain energy equation (4.1), and recalling the fundamental assumptions ($\gamma_{xz}=\gamma_{xz}=\varepsilon_z=0$), strain energy can be given in terms of material properties and deflection. For a plate of uniform thickness, strain energy can be integrated over the thickness (from –t/2 to t/2) and written as

$$U = \frac{1}{2}\iint_A \frac{t^3}{12(1-\nu^2)}\left[E_x w_{xx}(w_{xx}+\nu\cdot w_{yy}) + E_y w_{yy}(w_{yy}+\nu\cdot w_{xx}) + 4G_{12}w_{xy}{}^2(1-\nu^2)\right] \tag{4.25}$$

Or, alternatively

$$U = \frac{1}{2}\iint_A \frac{t^3}{12(1-\nu^2)}\left[E_x w_{xx}{}^2 + E_y w_{yy}{}^2 + w_{xx}w_{yy}\cdot\nu\,(E_x+E_y) + 4G_{12}w_{xy}{}^2(1-\nu^2)\right] \tag{4.26}$$

Substituting flexural rigidities (located below in 4.28a - 4.28e) yields a final expression for strain energy:

$$U = \frac{1}{2}\iint_A D_{11}w_{xx}{}^2 + D_{22}w_{yy}{}^2 + D_{12}w_{xx}w_{yy} + D_{21}w_{xx}w_{yy} + 4D_{66}w_{xy}{}^2\ dx\ dy \tag{4.27}$$

where,

$$D_{11} = \frac{E_x t^3}{12(1-\nu^2)}, \qquad D_{22} = \frac{E_y t^3}{12(1-\nu^2)}, \qquad D_{12} = \frac{\nu E_y t^3}{12(1-\nu^2)} \tag{4.28a - c}$$

$$D_{21} = \frac{\nu E_x t^3}{12(1-\nu^2)}, \qquad D_{66} = \frac{G_{12} t^3}{12} \qquad (4.28d - e)$$

4.1.3 Application of Ritz Method

The Ritz method will now be applied, as it is ideally suited for the bending of a clamped rectangular plate, of sides *a* and *b*, carrying a uniform load. The Ritz method is based on the principle of minimum potential energy, which states, "of all admissible displacements, those which satisfy the equilibrium equations make the total potential energy a minimum" (p.73, Reddy, J.N., 1997). For this particular application of the method, the principle of virtual work will be used, related to potential energy as shown in (4.29).

$$\delta U + \delta V = \delta (U + V) \equiv \delta \Pi \equiv 0 \qquad (4.29)$$

where,

U = strain energy

V = work

U + V = Π = potential energy

The plate is assumed to have all of its edges clamped, resulting in boundary conditions of the following form:

$$w = 0 \quad , \quad \frac{\partial w}{\partial x} = 0 \quad (x = a, 0)$$

$$w = 0 \quad , \quad \frac{\partial w}{\partial y} = 0 \quad (y = b, 0)$$

Deflection assumes the form

$$w_0(x,y) \approx W_{mn}(x,y) = \sum_i^m \sum_j^n c_{ij}\eta_{ij}(x,y) \tag{4.30}$$

with $\eta_{ij}(x,y)$ being defined as functions that satisfy the clamped-clamped boundary conditions:

$$\eta_{ij}(x,y) = X_i(x)Y_j(y) \tag{4.31}$$

where,

$$X_i(x) = \left(\frac{x}{a}\right)^{1+i}\left(1-\frac{x}{a}\right)^2 \tag{4.32}$$

$$Y_j(y) = \left(\frac{y}{b}\right)^{1+j}\left(1-\frac{y}{b}\right)^2 \tag{4.33}$$

for i = 1,2,…,m and j = 1,2,…,n. Note that (4.32 - 4.33) have been simplified from (4.34 - 4.35) below.

$$X_i(x) = \sin\lambda_i x - \sinh\lambda_i x + \alpha_i(\cosh\lambda_i x - \cos\lambda_i x) \tag{4.34}$$

$$Y_j(y) = \sin\lambda_j y - \sinh\lambda_j y + \alpha_j(\cosh\lambda_j y - \cos\lambda_j y) \tag{4.35}$$

where,

$$\cos\lambda_i a \cdot \cosh\lambda_i a - 1 = 0$$

$$\alpha_i = \frac{\sinh\lambda_i a - \sin\lambda_i a}{\cos\lambda_i a - \cosh\lambda_i a} = \frac{\cosh\lambda_i a - \cos\lambda_i a}{\sinh\lambda_i a + \sin\lambda_i a}$$

The virtual work of the plate with clamped-clamped boundary conditions can be given by Eq. 4.36 below (as per Ugural, 1981),

$$0 = \int_0^b \int_0^a \left[D_{11}\left(\frac{\partial^2 w_0}{\partial x^2} \frac{\partial^2 \delta w_0}{\partial x^2} \right) + D_{12}\left(\frac{\partial^2 w_0}{\partial y^2} \frac{\partial^2 \delta w_0}{\partial x^2} + \frac{\partial^2 w_0}{\partial x^2} \frac{\partial^2 \delta w_0}{\partial y^2} \right) \right. \tag{4.36}$$

$$\left. + 4D_{66}\left(\frac{\partial^2 w_0}{\partial x \partial y} \frac{\partial^2 \delta w_0}{\partial x \partial y} \right) + D_{22}\left(\frac{\partial^2 w_0}{\partial y^2} \frac{\partial^2 \delta w_0}{\partial y^2} \right) - q \delta w_0 \right] \quad dx \quad dy$$

with

$$\delta \mathrm{w}_0 = \sum_{\mathrm{p}}^{\mathrm{m}} \sum_{\mathrm{q}}^{\mathrm{n}} \delta \mathrm{c}_{\mathrm{pq}} \eta_{\mathrm{pq}} \tag{4.37}$$

$$\eta_{pq}(x, y) = X_p(x) Y_q(y) \tag{4.38}$$

Note that potential energy can be expressed as

$$\Pi(w_0) = \frac{1}{2} \int_0^b \int_0^a \left[D_{11}\left(\frac{\partial^2 w_0}{\partial x^2} \right)^2 + 2D_{12}\left(\frac{\partial^2 w_0}{\partial x^2} \frac{\partial^2 w_0}{\partial y^2} \right) \right. \tag{4.39}$$

$$\left. + 4D_{66}\left(\frac{\partial^2 w_0}{\partial x \partial y} \right)^2 + D_{22}\left(\frac{\partial^2 w_0}{\partial y^2} \right)^2 - 2q w_0 \right] dx\, dy$$

Substituting (4.30 - 4.31) and (4.37 - 4.38) into (4.36) results in

$$0 = \sum_p^m \sum_q^n \left\{ \sum_i^m \sum_j^n c_{ij} \int_0^b \int_0^a \left[D_{11} \frac{d^2 X_i}{dx^2} Y_j \frac{d^2 X_p}{dx^2} Y_q + 4D_{66} \frac{dX_i}{dx} \frac{dY_j}{dy} \frac{dX_p}{dx} \frac{dY_q}{dy} \right. \right. \tag{4.40}$$

$$\left. \left. + D_{12}\left(X_i \frac{d^2 Y_j}{dy^2} \frac{d^2 X_p}{dx^2} Y_q + \frac{d^2 X_i}{dx^2} Y_j X_p \frac{d^2 Y_q}{dy^2} \right) + D_{22} X_i \frac{d^2 Y_j}{dy^2} X_p \frac{d^2 Y_q}{dy^2} \right] dx\, dy - \int_0^b \int_0^a q X_p Y_q \, dx dy \right\} \delta c_{pq}$$

Since the summation over p and q is arbitrary, (4.40) can be reduced to

$$0 = \sum_{i}^{m}\sum_{j}^{n}\left\{\int_0^b\int_0^a\left[D_{11}\frac{d^2X_i}{dx^2}Y_j\frac{d^2X_p}{dx^2}Y_q + 4D_{66}\frac{dX_i}{dx}\frac{dY_j}{dy}\frac{dX_p}{dx}\frac{dY_q}{dy}\right.\right. \tag{4.41}$$

$$\left.\left. + D_{12}\left(X_i\frac{d^2Y_j}{dy^2}\frac{d^2X_p}{dx^2}Y_q + \frac{d^2X_i}{dx^2}Y_jX_p\frac{d^2Y_q}{dy^2}\right) + D_{22}X_i\frac{d^2Y_j}{dy^2}X_p\frac{d^2Y_q}{dy^2}\right]dx\,dy\right\}c_{ij} - \int_0^b\int_0^a qX_pY_q\,dx\,dy$$

This equation can easily be solved with a symbolic manipulator, e.g. MathCAD. For m = n = 1 and $q = q_0$ (uniformly distributed load), evaluating the integrals results in

$$0 = \left[\left(\frac{4}{5a^3}\right)\left(\frac{b}{630}\right)D_{11} + 4D_{66}\left(\frac{2}{105a}\right)\left(\frac{2}{105b}\right) + 2D_{12}\left(-\frac{2}{105a}\right)\left(-\frac{2}{105b}\right) + D_{22}\left(\frac{a}{630}\right)\left(\frac{4}{5b^3}\right)\right]c_{11}$$

$$-\left(\frac{a}{30}\right)\left(\frac{b}{30}\right)q_0$$

Solving for the constant c_{11}

$$c_{11} = \left(\frac{49}{8}\right)\frac{q_0a^4}{7D_{11} + 4\frac{a^2}{b^2}(D_{12} + 2D_{66}) + 7\frac{a^4}{b^4}D_{22}}$$

Substituting c_{11} into the deflection equation (4.30) gives a final expression for deflection as a function of position, load, geometry and material properties:

$$w_0(x,y) \approx W_{11}(x,y) = \left(\frac{49}{8}\right)\frac{q_0a^4\left[\frac{x}{a} - \left(\frac{x}{a}\right)^2\right]^2\left[\frac{y}{b} - \left(\frac{y}{b}\right)^2\right]^2}{7D_{11} + 4\frac{a^2}{b^2}(D_{12} + 2D_{66}) + 7\frac{a^4}{b^4}D_{22}} \tag{4.42}$$

This final expression for deflection has minimal error (<5%, p.299 Reddy, J.N., 1997) as compared to an expression with many more iterations. Deflection as a function of x and y is now plotted (Figure 4-4) using appropriate material properties (Table 4-1).

Table 4-1 Material parameters and resulting properties for the FESMP at cold/heated states

Material Parameters	
r	8.500 mils
a	3.000 in
b	3.000 in
N	16
t	0.2500 in
E_m	152.0 ksi
E_f	2.698×10^4 ksi
υ_m	0.45
υ_f	0.30
p_0	2.700 psi

Resulting Material Properties		
	cold state	heated state
E_x	267.3 ksi	115.8 ksi
E_y	152.9 ksi	34.95 ksi
v	0.4490	0.4490
G_{12}	52.74 ksi	12.06 psi

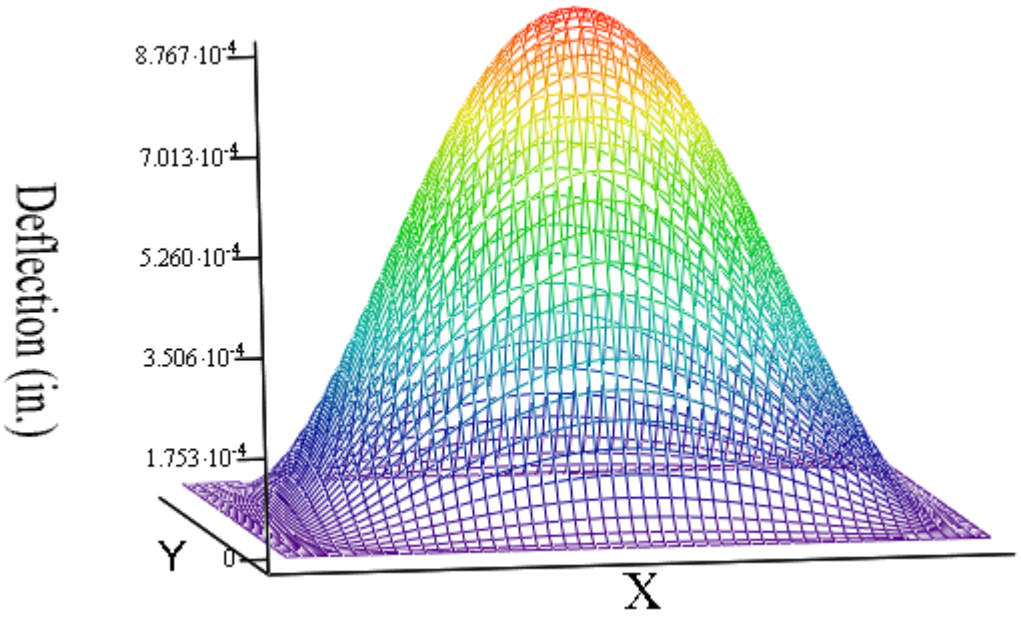

Figure 4-3 Out-of-plane deflection of cold FESMP plate versus X-Y position

Deflection at the center of the FESMPP plate (at x=a/2 and y=b/2) is shown to be 0.8767 mils in the cold state. For the heated state (E = 34.95 ksi), deflection at the center of the plate is found to be 3.51 mils. Note that the dimensions of the plate are 3" x 3".

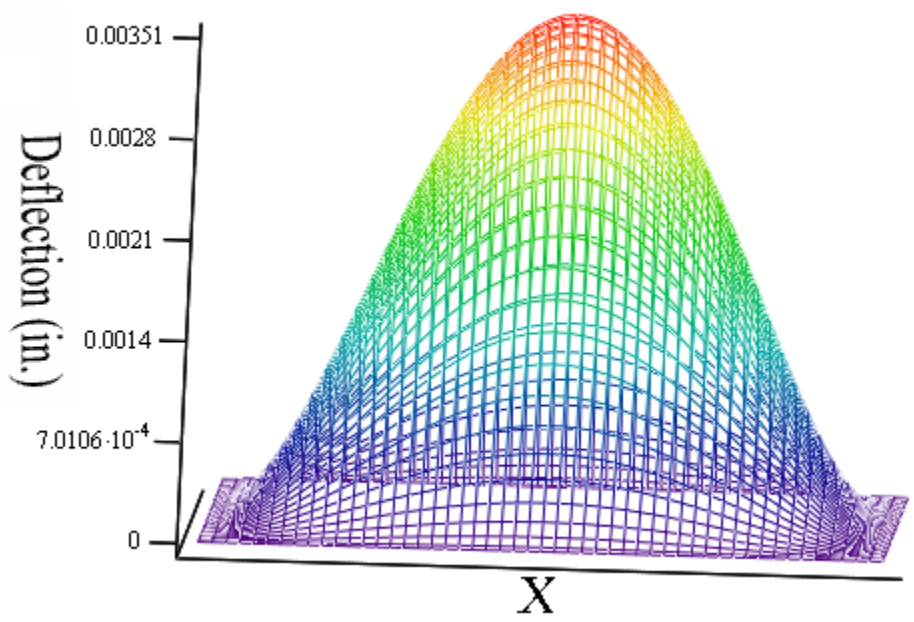

Figure 4-4 Out-of-plane deflection of heated FESMP plate versus X-Y position

Note that these plots and preceding analytical solution can easily be adapted to accommodate a fiber with parameters that differ from the Nichrome wire used. Although the model was able to produce a plot for the heated case in Figure 4-4, the results are invalid since fundamental assumptions 1. and 3. in section 4.1.1 are violated.

4.1.3.1 Theory for homogeneous SMP plate without embedded fibers

For comparison, deflection of an SMP plate without embedded fibers is also found using simple plate theory (Timoshenko, 1959). The work done by transverse surface loading p(x,y) can be represented as

$$W = \iint_A wp \; dx \; dy \tag{4.43}$$

Integrating and applying boundary conditions to the strain energy equation reduces it to

$$U = \frac{D}{2} \iint_A \left(\frac{\partial^2 w}{\partial x^2} + \frac{\partial^2 w}{\partial y^2} \right)^2 dx \, dy \tag{4.44}$$

Assuming a Fourier deflection expression of the form

$$w(x,y) := \sum_{m=1}^{\infty} \sum_{n=1}^{\infty} a_{mn} \cdot \left(1 - \cos\left(\frac{2 \cdot m \cdot \pi \cdot x}{a} \right) \right) \cdot \left(1 - \cos\left(\frac{2 \cdot n \cdot \pi \cdot y}{b} \right) \right) \tag{4.45}$$

Strain energy can be rewritten as

$$U = \frac{D}{2} \int_0^b \int_0^a \left\{ \sum_{m=1}^{\infty} \sum_{n=1}^{\infty} 4\pi^2 a_{mn} \left[\frac{m^2}{a^2} \cos\frac{2m\pi x}{a} \left(1 - \cos\frac{2n\pi y}{b} \right) + \frac{n^2}{b^2} \cos\frac{2n\pi y}{b} \left(1 - \cos\frac{2n\pi x}{a} \right) \right] \right\}^2 dx \, dy \tag{4.46}$$

And work can be rewritten as

$$W = p_0 \int_0^b \int_0^a \left[\sum_{m=1}^{\infty} \sum_{n=1}^{\infty} a_{mn} \left(1 - \cos\frac{2m\pi x}{a} \right) \left(1 - \cos\frac{2n\pi y}{b} \right) \right] dx \; dy \tag{4.47}$$

Applying minimizing conditions of $\frac{\partial \Pi}{\partial a_{mn}} = 0$, where Π = potential energy = U − W, it follows that

$$0 = 4D\pi^4 ab\left\{\left[3\left(\frac{m}{a}\right)^4 + 3\left(\frac{n}{b}\right)^4 + 2\left(\frac{m}{a}\right)^2\left(\frac{n}{b}\right)^2\right]a_{mn} + \sum_{r=1}^{\infty} 2\left(\frac{m}{a}\right)^4 a_{mr} + \sum_{r=1}^{\infty} 2\left(\frac{n}{b}\right)^4 a_{rn}\right\} - p_0 ab \tag{4.48}$$

For a square plate (a = b), iterating and plugging constants into the assumed deflection expression yields:

$$w = \frac{p_0 a^4}{4D\pi^4}\left[.11774\left(1-\cos\frac{2\pi x}{a}\right)\left(1-\cos\frac{2\pi y}{a}\right) + .01184\left(1-\cos\frac{4\pi x}{a}\right)\left(1-\cos\frac{2\pi y}{a}\right)\right.$$

$$+ .01184\left(1-\cos\frac{2\pi x}{a}\right)\left(1-\cos\frac{4\pi y}{a}\right) + .00189\left(1-\cos\frac{4\pi x}{a}\right)\left(1-\cos\frac{4\pi y}{a}\right) + .00268\left(1-\cos\frac{2\pi x}{a}\right)\left(1-\cos\frac{6\pi y}{a}\right)$$

$$\left. + .00268\left(1-\cos\frac{6\pi x}{a}\right)\left(1-\cos\frac{2\pi y}{a}\right) + .00020\left(1-\cos\frac{6\pi x}{a}\right)\left(1-\cos\frac{6\pi y}{a}\right)\right] \tag{4.49}$$

Note that one iteration results in a 1.5% error, and that 7 iterations are used here. This equation is then plotted as a function of x and y, using the other fixed values shown below in Table 4-2.

Table 4-2 Values used in homogeneous SMP plate

Material Parameters	
a	3.000 in.
b	3.000 in.
p_0	2.700 psi
E	152.3 ksi
t	0.2500 in.
v	0.45

Resulting Material Properties		
	cold state	heated state
E_x	152.3 ksi	34.81 psi
E_y	152.3 ksi	34.81 psi
v	0.45	0.45
G_{12}	52.52 ksi	12.00 ksi

where,

$$D = \frac{Et^3}{12(1-\nu^2)}$$

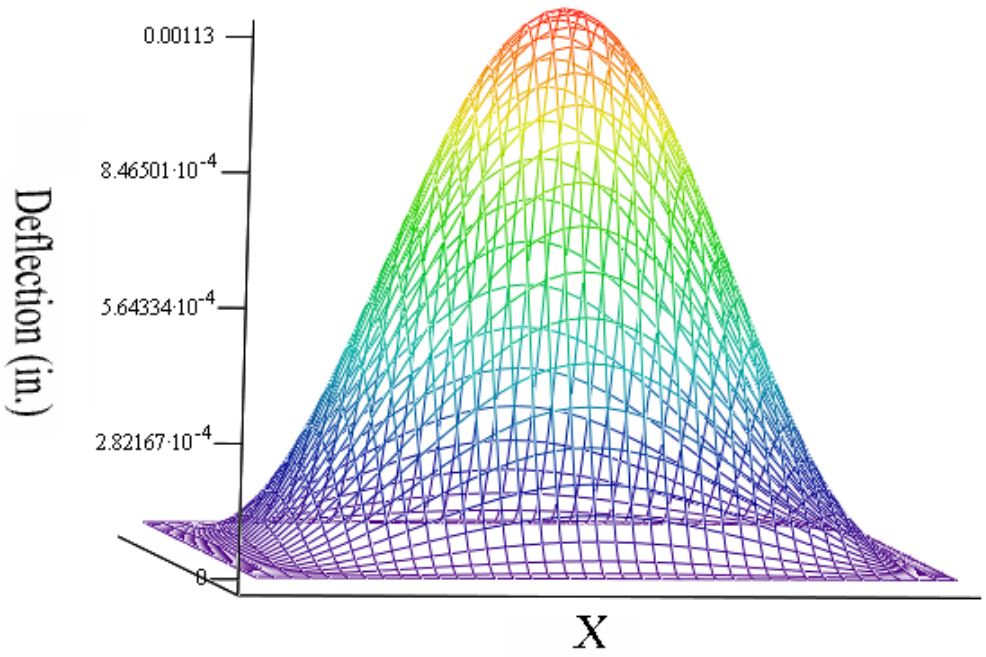

Figure 4-5 Out-of-plane deflection of cold homogeneous SMP plate versus X-Y position

The maximum deflection found here is 1.113 mils at the center of the plate as compared to 0.877 mils found above (Figure 4-4) when fibers were embedded into the un-heated plate. It makes sense, of course, that the deflection would decrease with embedded fibers, and a 20% reduction seems reasonable. However, 1.113 mils of out-of-plane deflection is still very small

and highly unlikely to be the cause of any structural damage if the SMP plate were functioning as the skin on a morphing aircraft. It is only when the homogeneous SMP plate is heated that the clear advantage of the fibers is shown. As shown in Figure 4-6 below, the maximum deflection at the center of the SMP plate is found to be 4.94 in. This is obviously far too large a deflection for the plate to withstand without failing and also too large for the previously used plate theory model to hold. The results of Figure 4-6 below are therefore invalid.

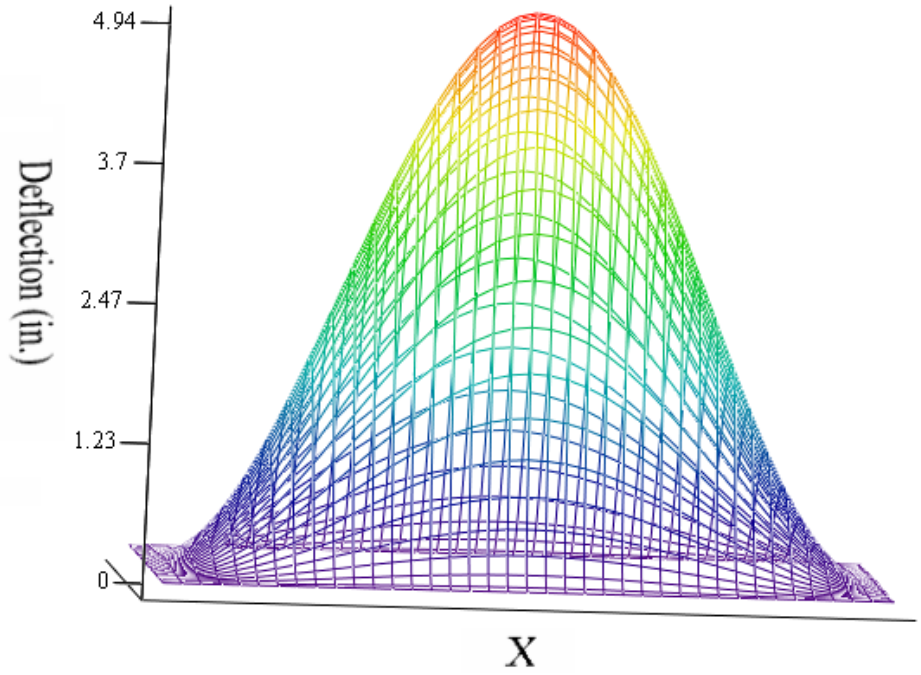

Figure 4-6 Out-of-plane deflection of heated homogeneous SMP plate versus X-Y position

4.1.4 Calculating the effective modulus of the fibers

The fiber modulus, E_f, that was used above (4.18-4.42) is a material property of the fiber in its unstrained (un-tensioned) state. Since the fibers embedded into the SMP matrix

can be pre-tensioned to further reduce deflection, it becomes necessary to account for the new increased effective modulus of the fibers due to the applied tension. In order to directly relate the effect of tensioning the fiber to the reduced deflection of the fiber-embedded SMP plate, the tension in the fiber is first related to deflection in the fiber through string/cable theory. Deflection can then be expressed as a function of tension in the fiber. Next, a new expression for deflection will be found, this time as a function of modulus, using plate theory. The two expressions can then be equated using the common deflection term, and an effective modulus of the fiber will then be created that is a function of tension in the fiber.

4.1.4.1 Finding fiber deflection vs. fiber tension via string/cable theory

A two-dimensional model of a tensioned wire undergoing a lateral deflection is created (Figure 4-7). Note that once the fiber is tensioned, it is assumed that the fiber will retain its tension through the heating process, and, relevant to later modeling, the shearing process.

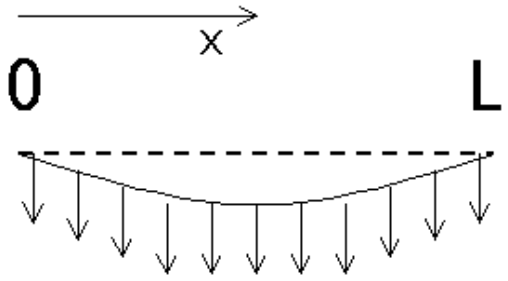

Figure 4-7 Drawing of 2-D tensioned wire model

The wire is assumed to be in equilibrium and tension is assumed to be constant throughout the wire. With force density ρg (i.e. the weight of the wire) and tension T, the equilibrium profile $u(x)$ of the wire is governed by

$$\frac{d^2u}{dx^2} = \frac{\rho g}{T} \tag{4.50}$$

Integrating twice and applying boundary conditions $u(0) = 0$ and $u(L) = 0$, the wire's deflection profile is found to be

$$u(x) = x(x-L)\frac{\rho g}{2T} \tag{4.51}$$

Adding an upward pressure opposing gravity

$$u(x) = x(x-L)\frac{\rho_L g - P_L}{2T} \tag{4.52}$$

With,

r = radius of wire = 8.000 mils (26 AWG)

L = length of wire = 3.000 in.

ρ = density of wire = 524.4 lb/ft^3

ρ_L = linear density of wire = $\rho \pi r^2$

g = gravity

P = uniform pressure load = 2.700 psi (400.0 psf)

P_L = linear pressure load = 8.100 lbf/in.

Deflection as a function of position, x, and tension, T, is found to be

$$u(x,T) = \frac{4.038}{T} \cdot \left(3x - x^2\right) \text{ in.} \tag{4.53}$$

Note that maximum deflection, as a function of only tension, can easily be found by setting x equal to L/2.

4.1.4.2 Finding fiber tension versus fiber modulus via plate theory

The first step is to come up with effective plate parameters that are adapted from the many parallel fibers' parameters. Assuming the area in between the fibers will behave the same as the fibers themselves (which will later be shown to be true once they are embedded into the SMP), the total cross-section of the group of wires can be changed into one thinner, square cross-section, as shown in Figure 4-8, to create a plate with an effective thickness.

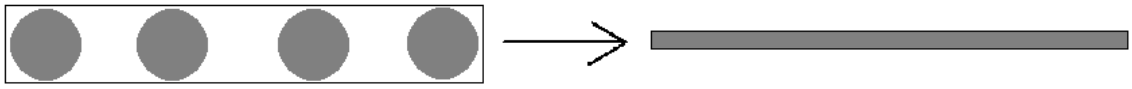

Figure 4-8 Geometrically converting total fiber cross-sectional area

The area of the sum of fiber cross-sections is divided by its length, resulting in an effective thickness of the wire plate.

$$t_{effective} = \frac{\pi \cdot r_{wire}^{\ 2} \cdot n}{a} \tag{4.54}$$

where,

r_{wire} = radius of the wire = 8.000 mils (26 AWG)

n = number of wires = 16

a = length of cross-section = 3.000 in.

The second step is to set the deflection from the two-dimensional model created via string/cable theory equal to the deflection from plate theory model. The plate theory to create the model relies on the same Ritz method used to model the SMP plate, except that the plate is fully isotropic, so that the D constants are all equal in this case. Since the D constants are all equal, the governing equation becomes much simpler and so a total of seven iterations are used.

$$x(x-a)\frac{\rho_L g - P_L}{2T_{wire}} = \tag{4.55}$$

$$\frac{p_0 a^4}{4D\pi^4}\left[.11774\left(1-\cos\frac{2\pi x}{a}\right)\left(1-\cos\frac{2\pi y}{a}\right)+.01184\left(1-\cos\frac{4\pi x}{a}\right)\left(1-\cos\frac{2\pi y}{a}\right)\right.$$

$$+.01184\left(1-\cos\frac{2\pi x}{a}\right)\left(1-\cos\frac{4\pi y}{a}\right)+.00189\left(1-\cos\frac{4\pi x}{a}\right)\left(1-\cos\frac{4\pi y}{a}\right)$$

$$+.00268\left(1-\cos\frac{2\pi x}{a}\right)\left(1-\cos\frac{6\pi y}{a}\right)+00268\left(1-\cos\frac{6\pi x}{a}\right)\left(1-\cos\frac{2\pi y}{a}\right)$$

$$\left.+.00020\left(1-\cos\frac{6\pi x}{a}\right)\left(1-\cos\frac{6\pi y}{a}\right)\right]$$

where,

$$D = \frac{E_f t_e^{\,3}}{12\,(1-\nu_f^{\,2})}$$

This expression can be reduced to

$$x(x-a)\frac{\rho_L g - P_L}{2\cdot T_{wire}} = -\frac{0.01590\cdot a^4\cdot p_0\cdot\left(\nu_f^{\,2}-1\right)}{E_f\cdot t_e^{\,2}} \tag{4.56}$$

After some algebraic manipulation, the modulus of the wire can be expressed as a function of tension in the wire at the center of the square plate, $x = y = \frac{a}{2}$. First, the plate deflection is found for a given modulus, then that deflection is equated to that of a fiber so that E_f can be written as a function of tension, T.

$$E_f(T_{wire}) = T_{wire} \cdot \frac{.12152 \cdot a^2 \cdot p_0 \cdot \left(\nu_f{}^2 - 1\right)}{t_e{}^3 \cdot \left(\rho_L \cdot g - P_L\right)} \tag{4.57}$$

Note that a tension of .144lbf corresponds to a modulus of 186 Gpa (shown below in Figure 4-9), which is the unstrained actual modulus of the Nichrome wire used. This discrepancy (0 lbf should correspond to unstrained modulus) will quickly become negligible as a useful amount of tension is applied.

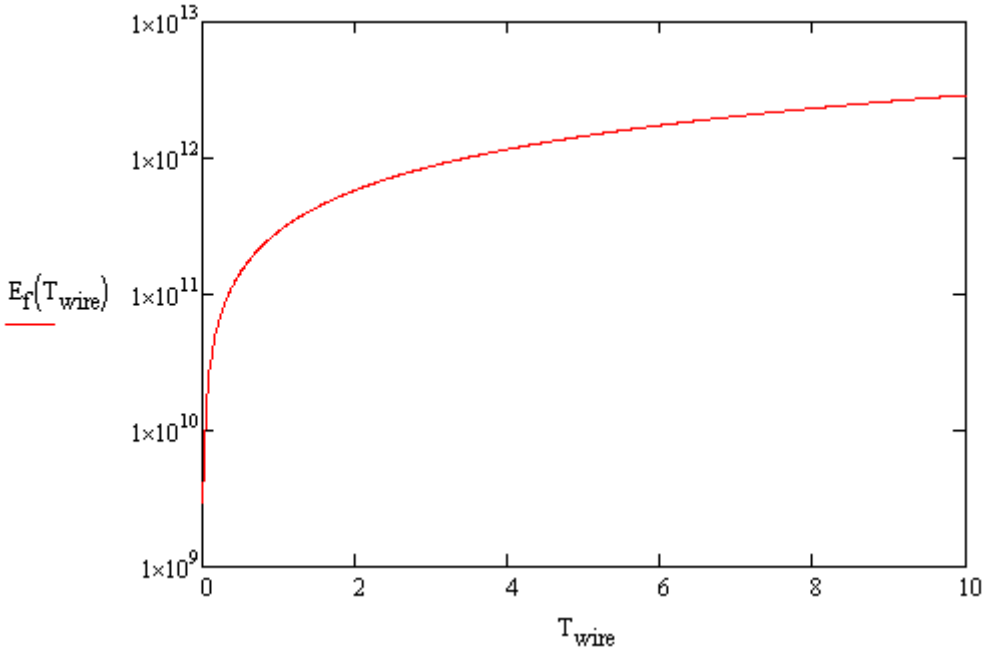

Figure 4-9 Effective Nichrome fiber modulus (Pa) as a function of its tension (N)

4.1.4.3 Maximum deflection of FESMP tile versus overall modulus

The deflection at the center of the FESMPP vs. its overall modulus is plotted in Figure 4-10 below. As the modulus increases by about an order of magnitude, the deflection does as well. Note that a modulus of 152.3 ksi (which corresponds to a homogeneous SMP plate) results in a deflection of 1.113 mils, which, as it should be, is identical to the maximum deflection of the homogeneous SMP plate in Figure 4-5.

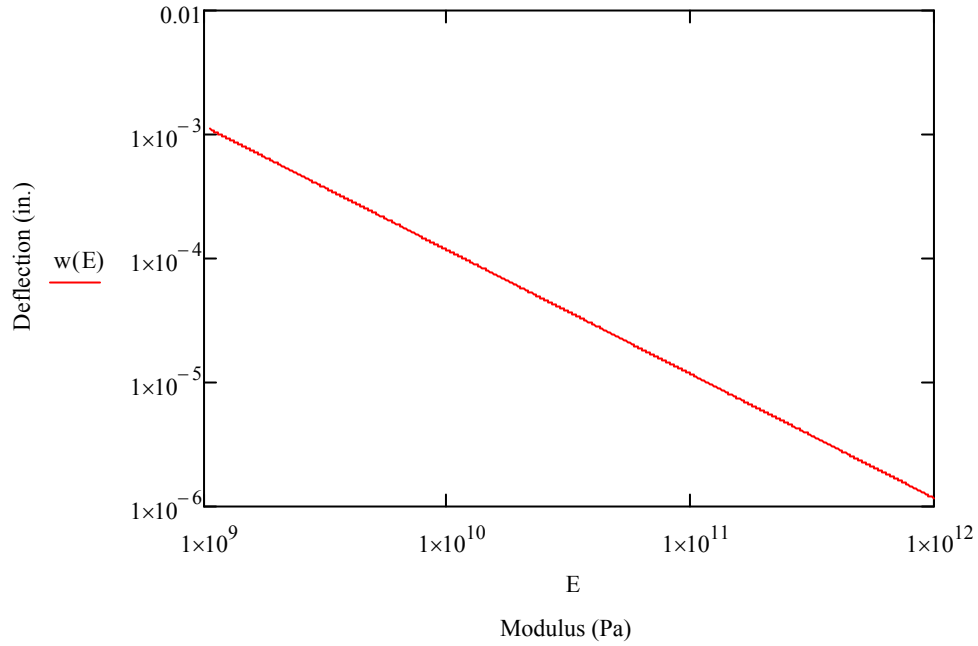

Figure 4-10 Log-Log plot of FESMP tile deflection versus overall modulus

4.1.4.4 Maximum deflection of FESMP tile versus fiber tension

In order to achieve an overall modulus increase of the FESMPP, the fiber tension is increased. With the fiber tension kept in a reasonable range as per Figure 4-10 above (0 to 10 lbf), the deflection of the FESMPP is plotted versus the fiber tension (Figure 4-11).

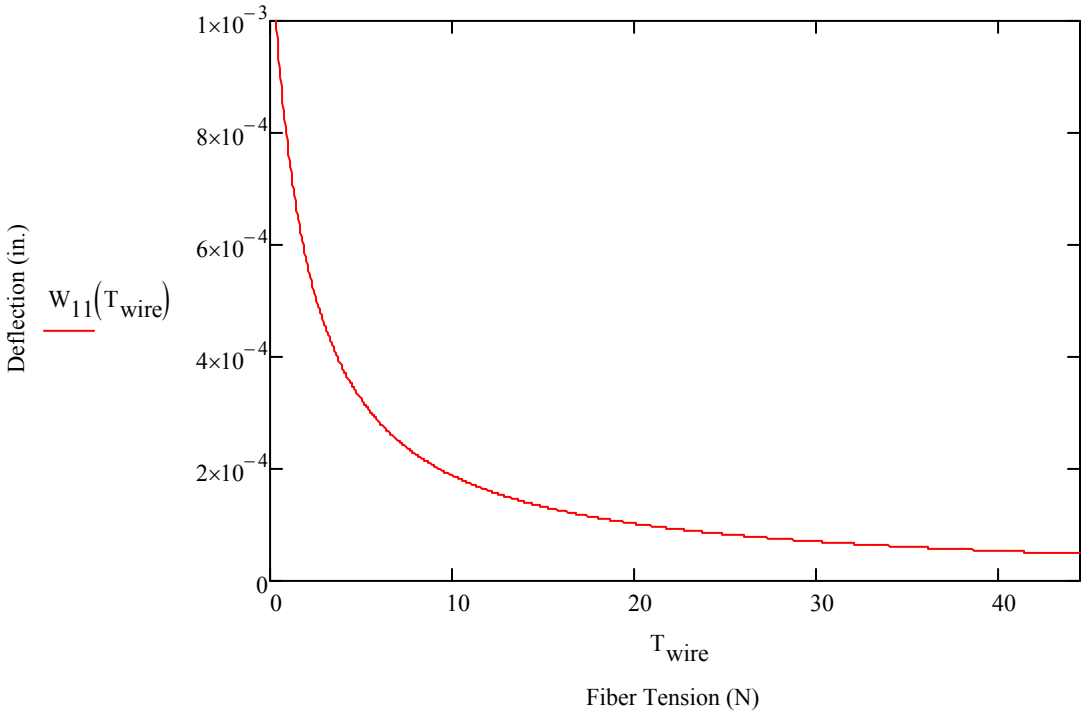

Figure 4-11 Plot of FESMPP maximum deflection vs. fiber tension.

As expected, the deflection of the FESMPP quickly reduces with increased fiber tension. To check and see that the model is consistent, a common data point is used for comparison. The maximum deflection of the FESMPP is found to be 0.8767 mils when the fiber tension is 0.1440 lbf. This is indeed correct, as a fiber tension of 0.1440 lbf (0.64 N) corresponds to un-tensioned Nichrome wire, having a modulus of 2.698 x 10^4 ksi as mentioned above. Thus, it makes sense that the deflection matches that of the un-tensioned FESMPP case above in Figure 4-3 (also .87 mils) for which un-tensioned Nichrome wire having a modulus of 2.698 x 10^4 ksi is also used.

Increasing the tension of uni-axial Nichrome fibers in an SMP matrix is now clearly and directly related to the deflection of a fiber-embedded shape-memory polymer plate. This

model can easily be broadened to include any matrix/fiber materials, so long as they are well-behaved and linear elastic.

4.2 PILLOWING MODEL

The above models equate the fiber-embedded SMP plate to a plate containing a single homogeneous material. In order for this to be valid, it must be proven that the deflections of the SMP in between the wires of the real-world heterogeneous plate are negligible in comparison to the overall out-of-plane deflection of the plate.

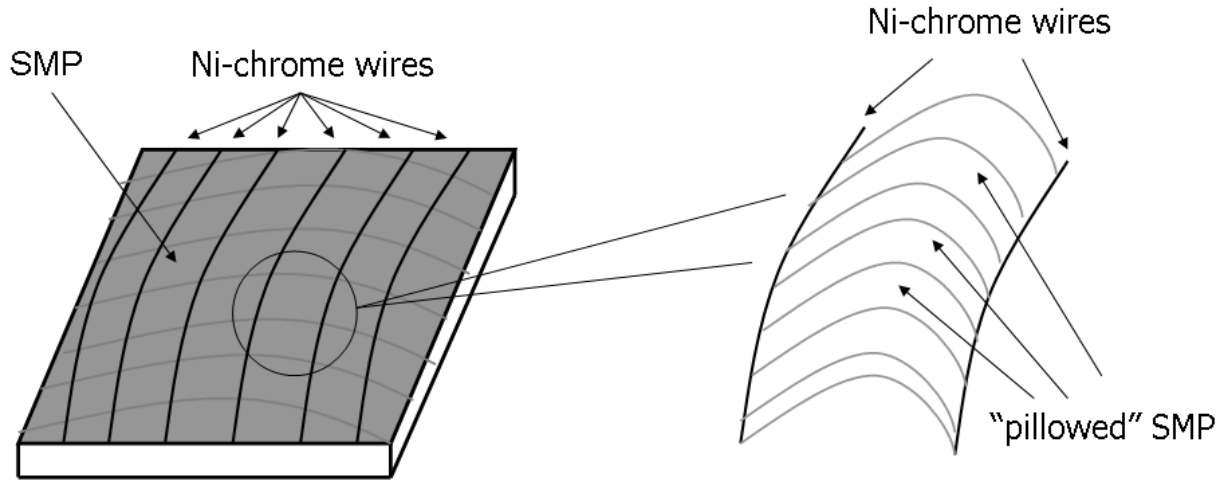

Figure 4-12 Depiction of the pillowing effect

The SMP in between the Nichrome wires was conservatively modeled as having two of its edges simply supported and the other two edges clamped, which corresponds to the real-world boundary conditions, but with an infinite length. The plate can be modeled as having an infinite length since the ratio of the length to width of the SMP being modeled is very large (~16). A few assumptions are made in addition to those listed sections 4.1.1 and 4.1.2.

1. The Nichrome "beams" are identical.
2. The deflection surface of the plate is symmetrical with respect to the x-axis.
3. The beams resist bending in the vertical plane only and do not resist torsion.

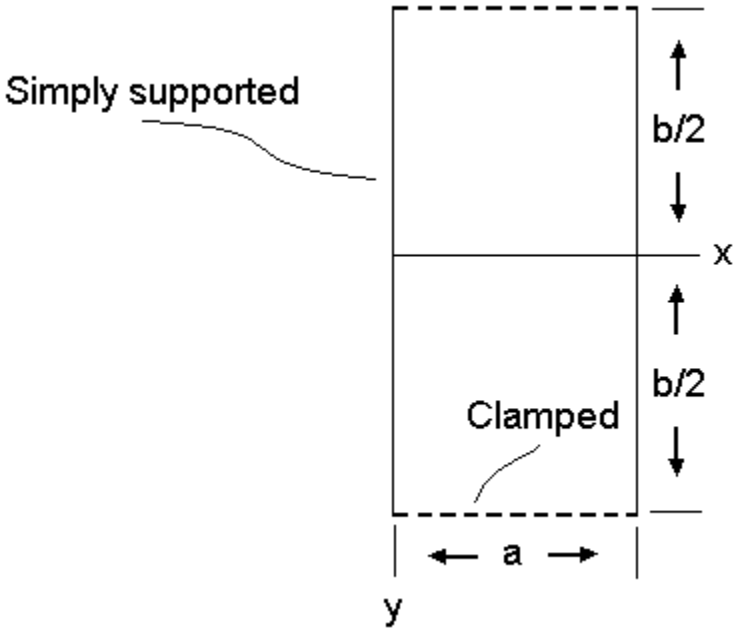

Figure 4-13 Boundary conditions for SMP plate undergoing pillowing effect

Using the solution generated (Timoshenko, 1959) for "Rectangular Plates with Two Opposite Edges Simply Supported and the Other Two Edges Clamped" (Eq. 4.58) derived using roughly the same method used at the beginning of this section , the maximum deflection at the center of the plate is found for a length to width ratio (b/a) of ∞.

$$w_{\max} = 0.01302 \cdot \frac{qa^4}{D} \tag{4.58}$$

where,

w_{max} = Maximum out-of-plane deflection of plate

q = Uniform lateral pressure load = 2.7 psi

a = Width of clamped side = 0.1875 in. (calculated by dividing length of plate, 3", by number of evenly spaced wires, 16)

D = Flexural rigidity = $\frac{Et^3}{12\,(1-\nu^2)}$

t = Thickness of plate = 0.25 in.

ν = Poisson's ratio = .45

Using Eq. 4.58, the maximum out-of-plane deflection of the plate is found for both the un-heated and heated states of SMP. Note that these deflections would be additive with the deflections found in the previous composite plate models. The results are listed below in Table 4-3.

Table 4-3 Maximum deflection values resulting from pillowing effect

	Maximum out-of-plane deflection (mils)
un-heated SMP (152.3 ksi)	1.7×10^4 mils
heated SMP (34.81 psi)	0.776 mils

Looking at Table 4-3, the deflection for the un-heated case is certainly negligible, but the deflection for the heated case is almost as much as the total overall deflection of the composite plate. The reason for the relatively large deflection in the heated case is that the model assumes only 16 Nichrome wires are embedded into the plate. This was done because

the previous composite plate assumes the same number of wires. However, as shown later in the "POWER REQUIREMENTS" sections, the minimum number of wires required to sufficiently heat the SMP is actually close to 50. This means that the distance in between each wire is much smaller than was used in calculating the results in Table 4-3. Using 50 wires in the model instead, which corresponds to a clamped length of 0.06", results in a maximum deflection of 0.008 mils for the heated SMP case. This amount is clearly negligible, especially since the overall composite plate deflection would decrease as well as a result of the increased number of wires.

5.0 FINITE ELEMENT MODELING FOR FESMP TILE

In order to verify the validity of the previous mathematical models, several finite element models were created using ANSYS.

5.1 ANSYS MODELS FOR DEFLECTION OF SMP TILE

The first models created were relatively simple and were used only to verify deflection results from the homogenous SMPP case. SOLID95 elements were used to form a 100,000 node (nodes increased until convergence was observed) mesh of the plate. Material properties were specified for SMP (Table 5-1 or ANSYS code in Appendix) and the side edges were all constrained to have no rotation or deflection.

Table 5-1 Material properties input into ANSYS for SMP deflection analysis

	cold state	heated state
E_x	152.3 ksi	34.81 psi
E_y	152.3 ksi	34.81 psi
E_z	152.3 ksi	34.81 psi
v_{12}	0.45	0.45
G_{12}	52.52 ksi	12.00 psi

A uniform pressure load of 2.700 psi was applied to the entire bottom of the plate. A linear static solution was found and out-of-plane deflection contours were plotted. The results of the cold state case are shown below in Figure 5-1.

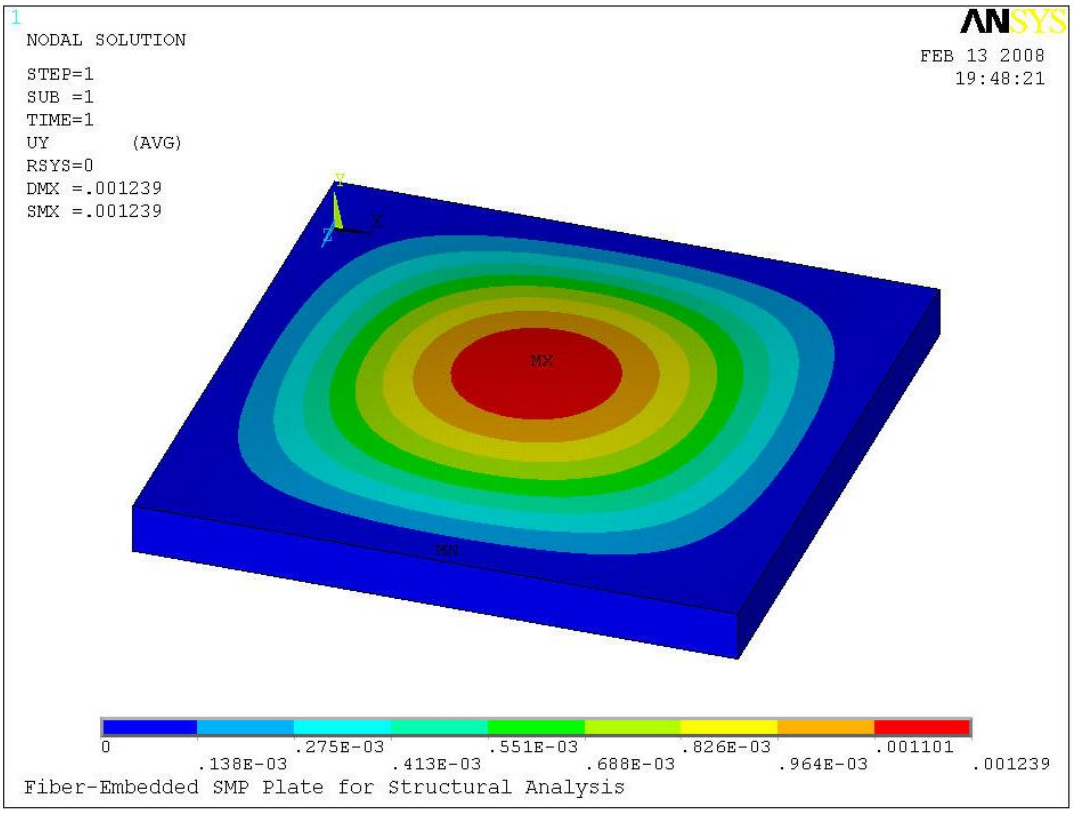

Figure 5-1 ANSYS out-of-plane deflection contour plot of homogeneous SMPP in cold state

ANSYS shows a maximum deflection of 1.239 mils as compared to 1.113 mils found in the analytical model derived above. Both the analytical results and finite element solutions results will be compared to experimental findings.

The same code used for the cold SMPP case was also used for the heated SMPP case, except for a couple modifications. The modulus of elasticity was, of course, changed to 240 kPa to accommodate the SMPP's change in properties when heated beyond its transition temperature. Secondly, a non-linear solution was found (by specifying NLGEOM, ON)

instead of the previously used linear solution since the expected deflections in the heated state are very large. With 100,000 nodes used again, ANSYS determined a maximum deflection value (at the center of the plate) of 0.6020 inches (Figure 5-2) as compared to 4.940 inches found in the analytical model. Note that the 4.94 in. found from the analytical model is invalid

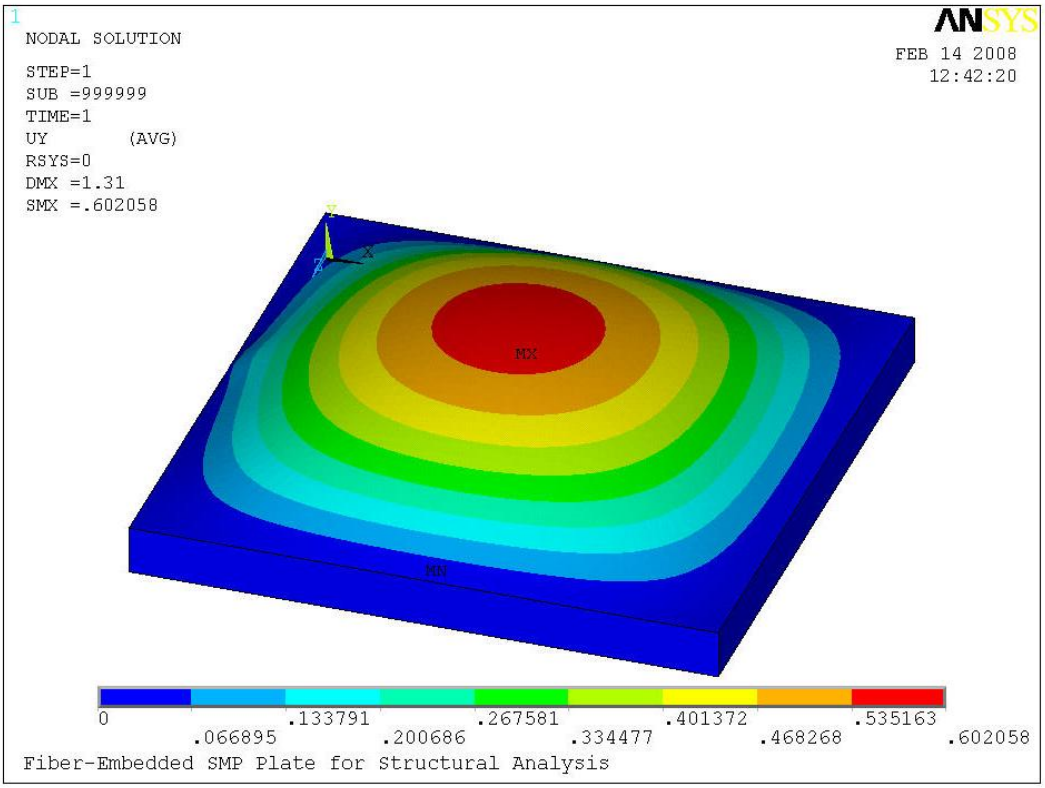

Figure 5-2 ANSYS out-of-plane deflection contour plot of homogeneous SMPP in heated state

This huge discrepancy was attributed to the analytical model being linear while the ANSYS model was non-linear. To verify this, an identical model was created in ANSYS with non-linear solving turned off. The resulting maximum deflection of this new linear (and incorrect) model was 5.421 inches - a difference of 8.8% compared to the analytical model. This is roughly the same margin of error that the analytical cold state model produced (10.1%). Since an out-of-plane deflection of 5 inches is borderline impossible in a 3 x 3 in. plate, it can

be assumed that both the linear ANSYS model and the analytical model (linear by nature) are incorrect. Therefore, the non-linear maximum deflection of 0.602 inches produced from the ANSYS model will be used as the point of reference when conducting experimental testing.

5.2 ANSYS MODELS FOR DEFLECTION OF FESMP TILE

Contour plots for out-of-plane deflections were also generated for the fiber-embedded SMP plate cases. The same code from above was used, only with the altered material properties shown below in Table 5-2.

Table 5-2 Properties input into ANSYS for FESMP deflection analysis

	cold state	heated state
E_x	267.3 ksi	115.8 ksi
E_y	152.9 ksi	34.95 ksi
E_z	152.9 ksi	34.95 ksi
v_{12}	0.449	0.449
G_{12}	54.74 ksi	12.01 ksi

Note that these properties in Table 5-2 are created from inputting the properties from Table 3-2 into Eqs. 4-18.

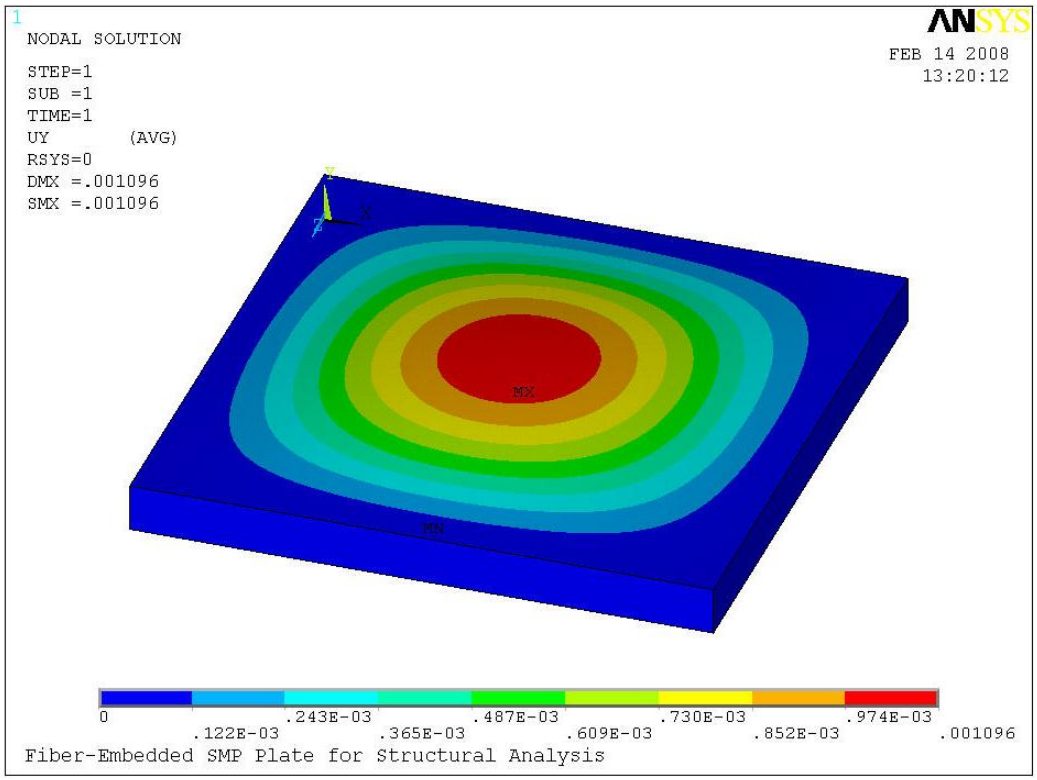

Figure 5-3 ANSYS out-of-plane deflection contour plot of FESMPP in cold state

Figure 5-3 shows the deflection results for the FESMPP in its cold state. It did not matter whether or not ANSYS solved for a linear or non-linear solution since the non-linear effects were negligible. The ANSYS solution found a maximum center deflection of 1.096 mils as compared to the 0.877 mil maximum deflection found with the analytical model of a FESMPP with zero tension in the wires. This results in a 19.9% discrepancy between the ANSYS and analytical model (if the ANSYS model is used as the reference). The only real difference between the FESMPP and SMPP ANSYS deflection models lies in the altered material properties of the plate, and so logically the source of error must lie there. However, since the material strength properties of SMP input into ANSYS were generated from the composite plate analytical model, and the boundary conditions of both models are identical, the

primary source of variation is in question. Although neither solutions is absolutely correct, the two are close enough to confirm validation. Figure 5-4 below shows the deflection results for the FESMPP in its heated state.

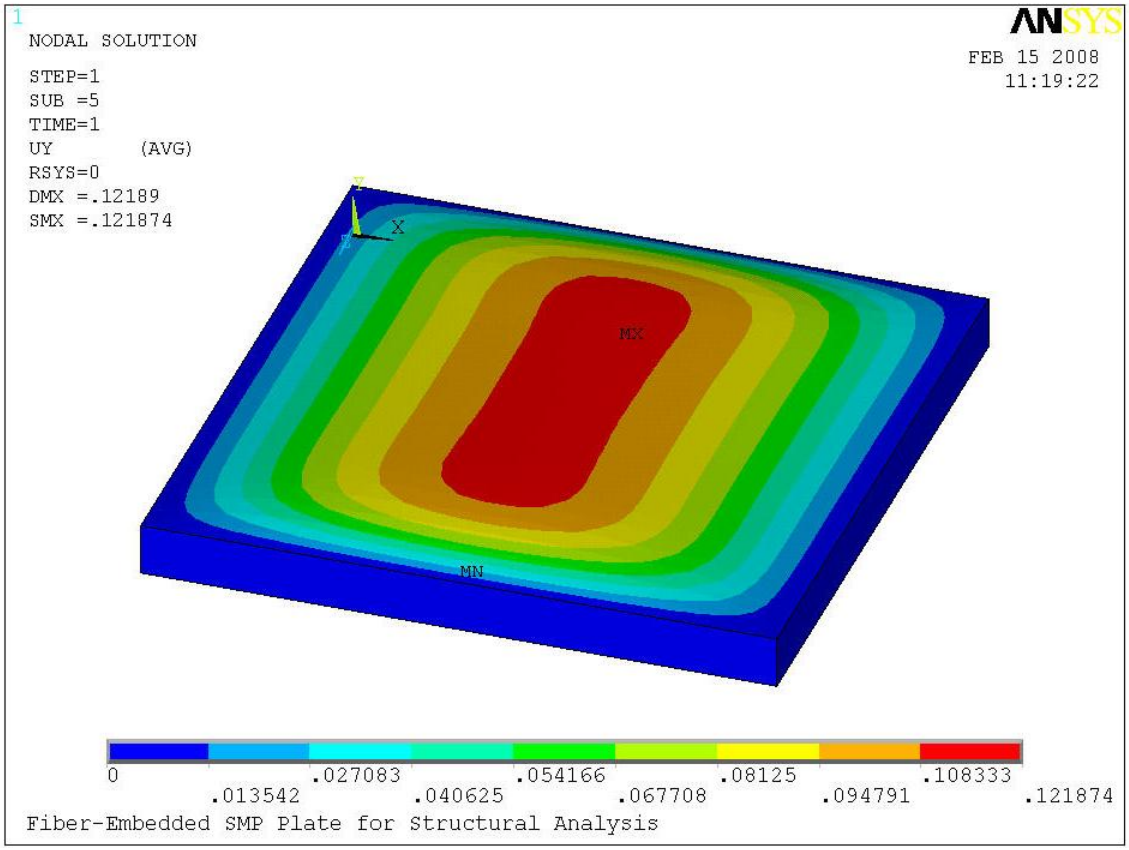

Figure 5-4 ANSYS out-of-plane deflection contour plot of FESMPP in heated state

A maximum deflection of 0.121 inches is found using a non-linear ANSYS model. It is interesting to note that if fewer than about 50,000 nodes were used, ANSYS was unable to find a reasonable solution and so 100,000 nodes were again used for convergence. Also interesting to note is that this is the first result where evidence of uni-axially embedded fibers is noticeable (shown by the rectangular deflection shape above). When compared to the heated, un-

tensioned FESMPP analytical model (max deflection of 0.00351), it becomes obvious that true solution is, in fact, non-linear. Therefore, the ANSYS model will be used as the point of reference for experimental testing rather than the analytical model.

Previously discussed was a method to incorporate the added resistance to out-of-plane deformation caused from tensioning the embedded Nichrome wires. Since this was done by relating the tension in the wire to its modulus of elasticity, an ANSYS model incorporating tension in the wires via a composite plate with improved strength properties would use the exact same code as the FESMPP model, only with increased strength properties. The maximum deflection of such an ANSYS plot would therefore follow the relationship generated in Eq. 4.57, which expressed the modulus of the wire as a function of its tension. One way to generate a non-trivial ANSYS representation of a FESMPP with tensioned wires would be to model the SMP and Nichrome as separate entities. However, this requires a substantial amount of processing time due to the number of elements needed to create a satisfactory mesh surrounding the tiny wires. In this work it is assumed that the value of the added accuracy would be minimal as compared to the computational burden.

5.3 ANSYS MODELS FOR SMP PLATE UNDERGOING SHAPE CHANGE

Several finite element ANSYS models were created to predict deflections caused from the shearing motion of the SMP tile. The first model created shows the deformed shape of the SMP plate after shape-change was induced without any built-in pretensions. As shown below in Figure 5-5, the out-of-plane folding effect is apparent. Note that ANSYS does not correctly display the final rhombus shape.

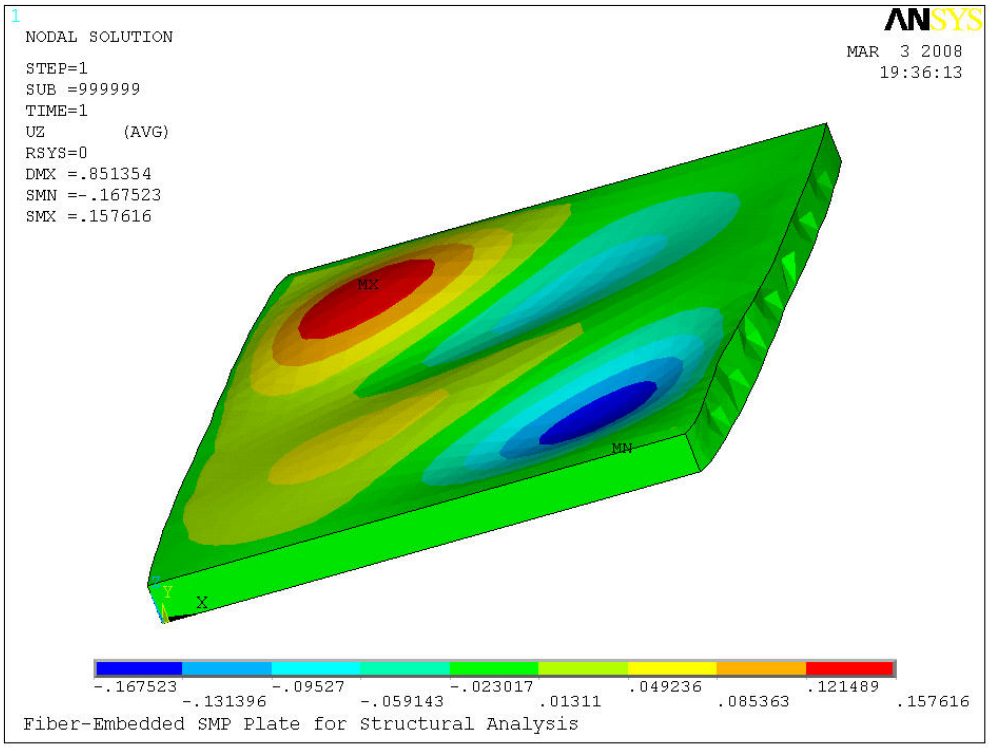

Figure 5-5 ANSYS z-deflection contour plot of out-of-plane folding effect caused by shape-change

The model was created with SOLID95 elements and 15,000 nodes. All four sides of the plate were constrained to have zero out-of-plane deflection. One of the four sides of the plate, which can be thought of as the "bottom", had its deflections constrained in all degrees of freedom. The opposing side (top) had X and Y deflections imposed such that its final position would result in a 45 degree rhombus shape. More specifically, the X deflection of the side was set to 2.12 in. and the Y deflection to 0.88 in. (Figure 5-6).

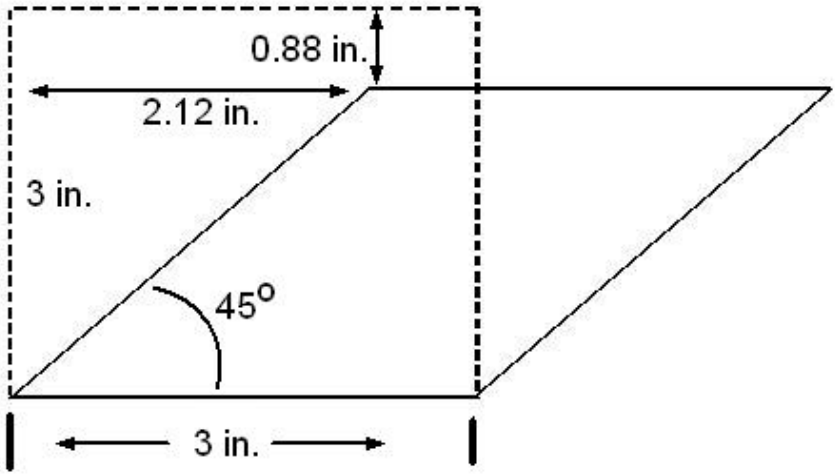

Figure 5-6 Drawing of square SMP tile changing to rhombus shape

The remaining two sides (the left and right) had deflections imposed so that their new positions would form a 45 degree angle with their original positions. In other words, a deflection boundary condition was imposed on both of the sides that satisfied the equation y = x (a slope of 1 corresponds to a 45 degree angle) for the left side and y = x - 3 for the right side.

6.0 FABRICATION

Several fabrication procedures were required, as there were a variety of different test specimens.

6.1 FIBER-EMBEDDED SMP TILE FABRICATION

The first set of specimens created and tested were the fiber-embedded SMP plates (FESMPPs). It took several trials before the final design of the FESMPPs was realized. The fabrication process of the four generations of prototype design occurred in a few shared general steps, which will now be given in chronological order.

A rigid frame was created to contain the SMP as well as induce shape change via its rotation. Nickel-Chromium wires were then placed uni-axially at the center of the frame. Next, a seal was created and SMP was poured, encasing the wires. The tile was then placed in an oven to cure and set the SMP. Once cured, the wires were cleaned up so that they were electrically connected and accessible. The tile was then ready for testing. The aforementioned steps are common to each generation of tile frame, but also very general. To ensure reproducibility, the variations of each stage of prototype fabrication will be explained specifically.

6.1.1 First Generation FESMP Tile

First, a simple preliminary prototype was created by machining 2 square cuts from 2 square plates to form the two frame pieces. Nickel-Chromium wires were woven around a separate rigid frame and then set on top of one of the two square pieces. The second square piece was then placed on top to sandwich the wires in between the frame (Figure 6-1) after a generous amount of epoxy was poured on the lower piece of the frame to ensure that the wires and frame halves were held in place.

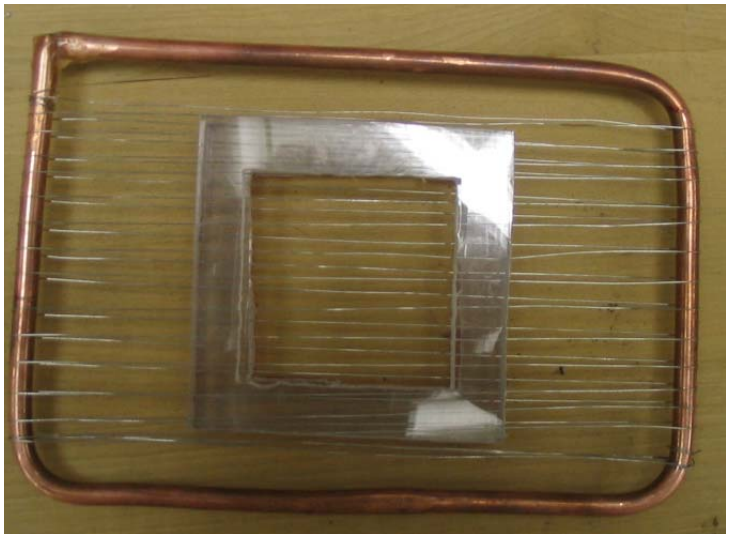

Figure 6-1 Preliminary frame sandwiching wires that are still wrapped around the rigid frame

After the epoxy finished curing, the wires were cut to free them from the frame. The loose ends of the Nichrome wires were then connected to one another in series. The bottom side of the new wire-embedded frame was sealed and SMP was poured inside. The final result is shown below in Figure 6-2.

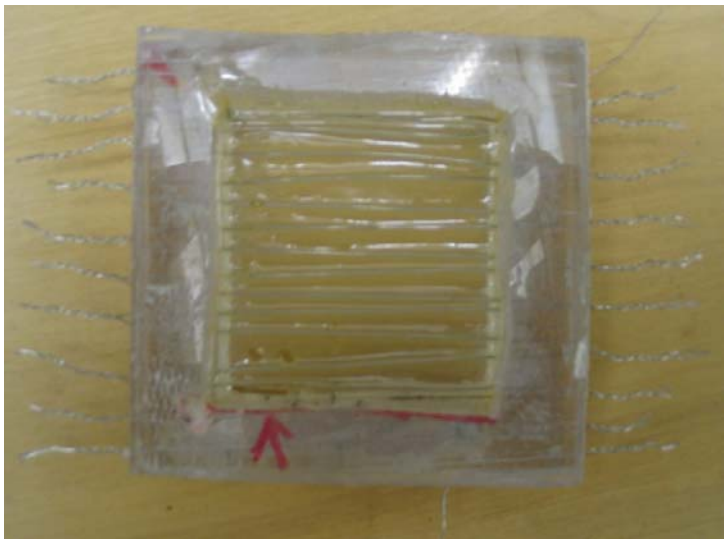

Figure 6-2 Preliminary attempt at embedding wires into the SMP

This design proved to be surprisingly effective once testing began, though there were a few obvious drawbacks. Since the frame is rigid and does not allow for motion, a new frame needed to be created to allow for the desired shape change.

6.1.2 Second Generation FESMP Tile

The next generation prototype was designed to allow for the desired amount of rotation. The frame for the FESMP tile was designed to be made of four connecting rigid bars. A drawing was made using SolidWorks, which was then input into a rapid-prototyping machine. The four identical pieces contained holes into which the wires were to be woven, as well as connecting pins and holes so that the assembled structure would rigidly rotate. Shown below in Figure 6-3 is the SolidWorks design that was input into the rapid-prototyping machine.

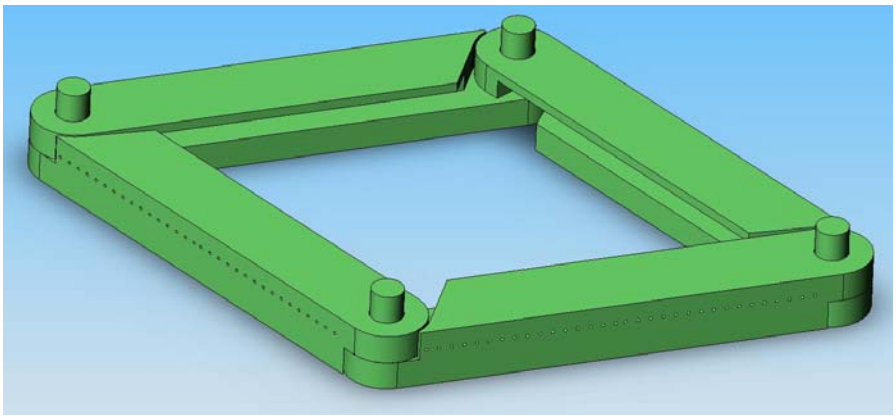

Figure 6-3 SolidWorks drawing of first FESMPP frame given to rapid-prototyping machine

Figure 6-4 shows the end result after coming out of the rapid-prototyping machine, having the wires woven and the SMP poured.

Figure 6-4 Fabricated prototype after wires were woven and SMP was poured

There were several drawbacks to this design as well. Firstly, weaving the 0.017" diameter Nichrome wires into the frame was labor intensive. It was also difficult to keep the wires in tension during the process. Secondly, the rapid-prototyped bars comprising the frame bowed inward during the SMP curing process compromising the structural integrity of the frame as well as causing the Nichrome wires to become un-tensioned.

6.1.3 Third Generation FESMP Tile

The frame of the third generation of the tile was created using injection molding and polycarbonate. First, a master part (Figure 6-5) was created using SolidWorks and the rapid-prototyping machine. The part created from the rapid-prototyping machine was used solely for the creation of the mold.

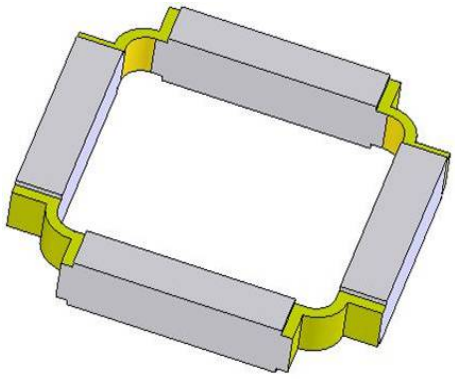

Figure 6-5 SolidWorks drawing to be imported into rapid-protoyping machine

The SolidWorks drawing itself, however, also represents what the final tile frame will look like. The yellow colored portion of the drawing represents the flexible hinged of the frame and will be made of polyurethane via injection molding. The white portion of the drawing will be

made of pieces of polycarbonate that have been machined to match the dimensions of the drawing. The polyurethane used to make the hinges will function as both the hinges as well as the adhesive that bonds the hinges to the rest of the polycarbonate frame.

After created, the master part (Figure 6-6) was then suspended in a box frame and silicon was poured into the box frame, completely covering the master part.

Figure 6-6 Resulting master part from rapid-prototyping machine, with attached material to allow mold creation process

The silicon-full box frame with the encased master part was placed into an oven and cured. The cured, hardened mold was then cut in half, resulting in a mold of the master part located inside (Figure 6-7).

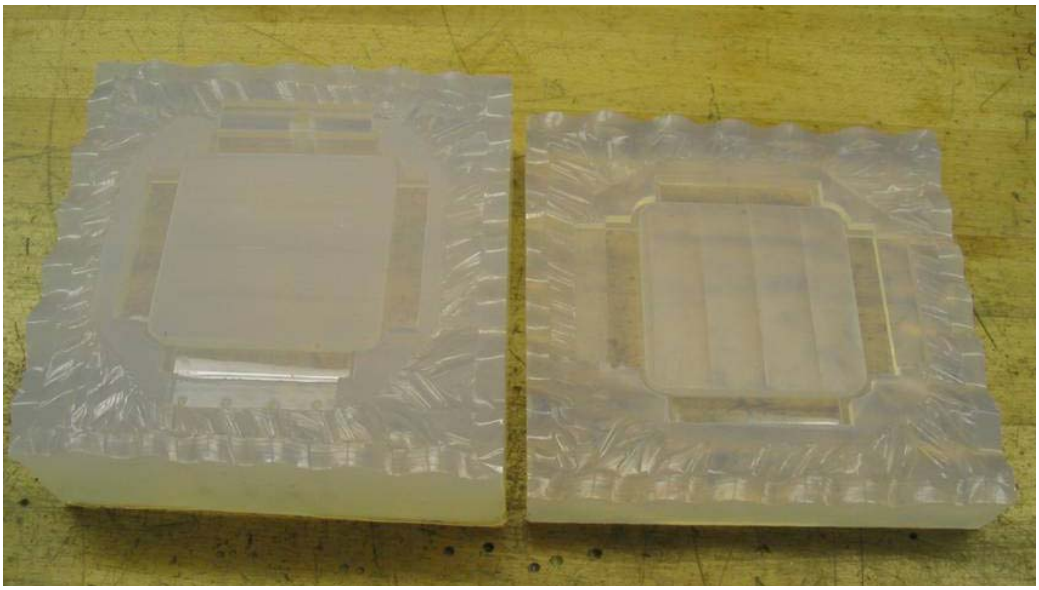

Figure 6-7 Silicon mold used to make final tile frame

After the creation of the mold, eight pieces were machined out of polycarbonate to be placed into the mold prior to polyurethane injection. Note that once the finished part is obtained, these polycarbonate pieces represent the white-colored portion of the SolidWorks representation of the part located in Figure 6-5. After the polycarbonate pieces were placed snuggly inside, a loom of wires (similar to the one used in the first generation tile, but with a removable side) was set on top of the bottom half of the frame (Figure 6-8).

Figure 6-8 Loom frame with removable side for Nichrome weaving (wires not shown)

The loom was placed in such a way that the wires ran uniaxially through what would be the middle of the tile while the loom frame hovered outside the entire mold. The mold was sealed, with the exception of the gate and valves (polyurethane intake and air outtake), and then set inside the vacuum-sealed mixing/pouring chamber (Figure 6-10).

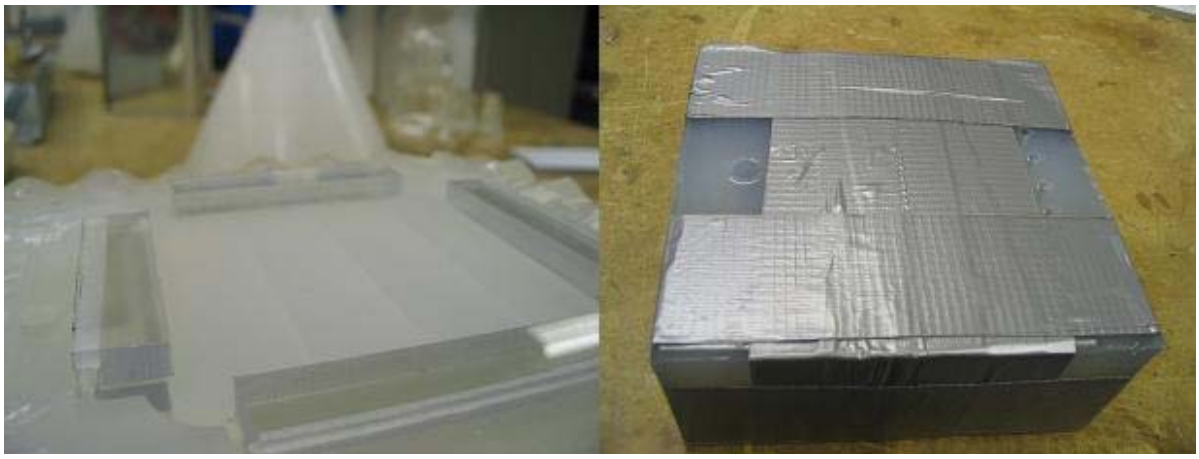

Figure 6-9 (Left) Close-up of the bottom half of the mold with polycarbonate pieces placed inside and (Right) sealed mold with gate and valves showing. Note that the wires are not shown in either of these pictures.

Figure 6-10 Vacuum-sealed mixing and pouring chamber (the mold is not inside).

After placing the sealed mold with polycarbonate frame pieces and wires contained inside, the two-part polyurethane recipe was then mixed and poured into the mold using the machine in Figure 6-10. The mold was once again placed into the oven to cure, this time for the polyurethane to harden. Following the curing process, the loom was slid out from the wires via its removable side and the mold was re-opened to reveal the newly created frame (Figure 6-11).

Figure 6-11 Third generation tile frame after being removed from the mold.

With polycarbonate sides and polyurethane hinges, the frame was able to easily rotate and withstand the tension created from the wires. It was noted that although the frame could withstand the tension of the wires, some quick tests showed that the hinges may prove to be too flexible and unable to resist the shrinking associated with curing SMP. Also since the loom hovered outside of the mold while its woven wires ran through the mold, clay was required to ensure there was a seal in between each wire. This caused for some messy and time consuming procedures.

6.1.4 Fourth Generation FESMP Tile

The next generation fiber-embedded shape-memory polymer tile was very similar to the third generation, except with a couple improvements. The loom of wires was integrated into the mold by drilling holes and placing rods into them for the wires to be woven around. As shown

in Figure 6-12 the integrated loom allowed for a much nicer mold without any protruding wires.

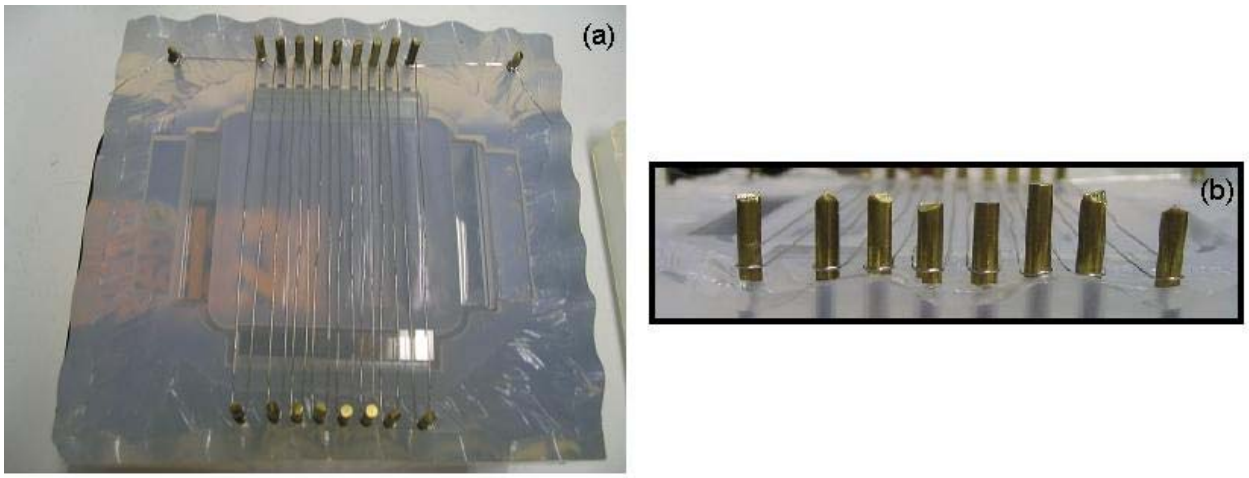

Figure 6-12 (a) Fourth generation mold with integrated loom for weaving wires and (b) close-up of wires woven around embedded rods in mold.

The remainder of the process for making the frame was nearly identical to the process used in the third generation FESMP tile. Polycarbonate pieces were again placed into the mold to act as the frame. The mold was sealed, polyurethane was poured and cured, and the resulting part was removed. The final part (Figure 6-13) required no clean-up (unlike the 3rd generation tile) and functioned as desired, with the exception of one flaw.

Figure 6-13 Fourth generation part after application of reflective tape used for optical sensor measurements

After around 3-4 cycles of heating the tile, rotating it, and cooling it back down, the polyurethane hinges started to tear. This was mainly due to the inability of the tile to remain rhombus-shaped during shape-change. Since there was no rigid fixture to force the tile into a rhombic shape during shape-change, it was up to the hinges to maintain the two equal sets of angles. The hinges were apparently too weak to withstand the forces associated with shearing and so a fifth generation tile was needed to fix the problem.

6.1.5 Fifth Generation FESMP Tile

With the fourth generation FESMP tile functioning nearly as desired, there were only a couple problems that needed to be addressed. It was originally intended that the SMP tile progress through its shape change while in a rhombic shape. It was determined during the third and fourth generation tile phases that the tile was, in fact, not maintaining a rhombic shape

throughout the shearing induced shape change. Wanting to salvage the third and forth generation tiles, it was decided that a rigid exoskeleton be made to fit into the existing tile frame. An attached exoskeleton would constrain the tile to rotate such that its shape would always be rhombic, as well as relieve a large amount of stress that had previously been placed on the polyurethane hinges. The exoskeleton to be fitted into the existing tile frames was designed using SolidWorks (Figure 6-14).

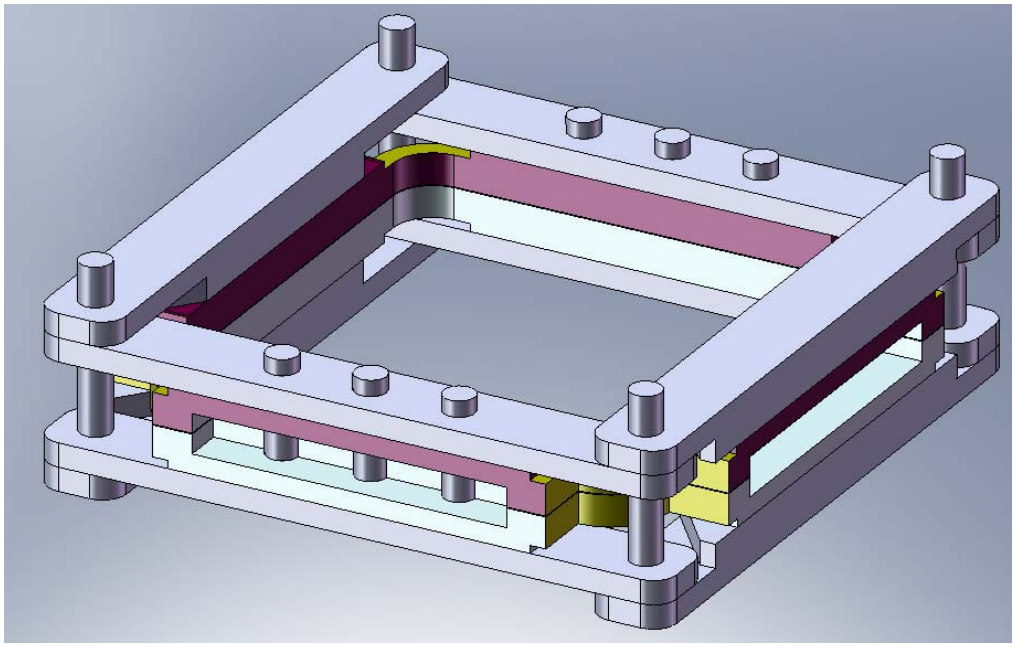

Figure 6-14 Exoskeleton to be fitted into existing tile frames created in SolidWorks

The exoskeleton was fitted with one pin on each corner and a total of six other pins to fit in pre-drilled holes through an existing tile frame. The six pins through the sides of the tile serve to secure the tile to the exoskeleton while the four corner pins allow for purely rotational shape change. Since it is assumed that the tile will almost certainly have to maintain its rhombic state with the attached exoskeleton, a physical exoskeleton was not made to confirm this. Also,

once the shear-induced shape-change testing had begun, it was clear that the problem of the hinges proved trivial in comparison to the buckling incurred from the shape-change process. It was determined that the exoskeleton frame would be machined later only if it were still needed in the efforts to reduce the buckling effect.

6.2 FABRICATION OF SMP TILES FOR BUCKLING REDUCTION

In order to address the large out-of-plane deformations in the tiles caused from the shear-induced shape change, fabrication of separate tiles was necessary for testing purposes. Note that the steps taken to reduce buckling were done strictly as a proof of concept. As a result, the original design specifications of a final SMP tile with a 0.25" thickness and shear-induced shape-change angle of 45^{o} were ignored.

Figure 6-15 Fourth generation FESMPP after only a slight shear-induced shape-change

These separate tiles were created *only* to address the large deformations caused from shearing and so no arrangements were made to accommodate embedded fibers or heating elements. Although embedded heating elements would likely have made it more convenient to heat the

tiles during pre-straining and testing, it was felt that additional variables into the system would have complicated things more than simplified them. Similar to the fiber-embedded SMP tiles, several attempts were made before reaching a sufficiently effective tile sample.

In each of the samples, the main concern to be addressed, of course, was the buckling effect caused from shearing the tile. This buckling takes effect almost immediately as the angle of deformation is increased since SMP is very soft in its transition phase (~100x lower modulus than rubber). As a way to prevent the SMP from deforming out-of-plane, pre-stretching the SMP along its diagonal allows the SMP to relax as its length shortens rather than bunch up out-of-plane. Common in each generation of tile fabrication was the general method of pre-strain. While in its soft state, the SMP was grabbed and pulled outwards along its length and width. It was then held in its stretched state until it cooled below its transition phase, causing it to re-harden and maintain its new shape. Note that only the center 3" x 3" square of the newly formed shape was important.

The amount of pre-strain needed was determined by some simple calculations. During the shape change process, one of the diagonals of the tile becomes shorter while the other becomes longer. This translates to one of the diagonals being in compression while the other is in tension. The tensioned (lengthened) diagonal only poses a problem if the amount by which it is strained exceeds 200% (maximum elastic strain of the SMP). The compressed (shortened) diagonal on the other hand is more cause for concern. As the diagonal is compressed, it leaves the SMP that lies in its path with nowhere else to go except up and down (out-of-plane). In order to cure this problem, the tile is pre-tensioned along its diagonal such that it will be in a relaxed state after enduring the compressive shape-change due to shearing of the tile. Since the tile is intended to rotate in either direction, it becomes necessary to pre-tension along both

diagonals. This also means that an increase in the pre-tension intended to overcome compression will cause the opposing diagonal (which is already tensioned) to be further tensioned. With this in mind, only a slight factor of safety will be used to ensure the shortened diagonal stays in tension while the lengthened diagonal strains only as much as needed and definitely lower than the maximum amount of 200%. As shown in Figure 6-16, the diagonal of a 3 x 3 in. tile is 4.24 in.

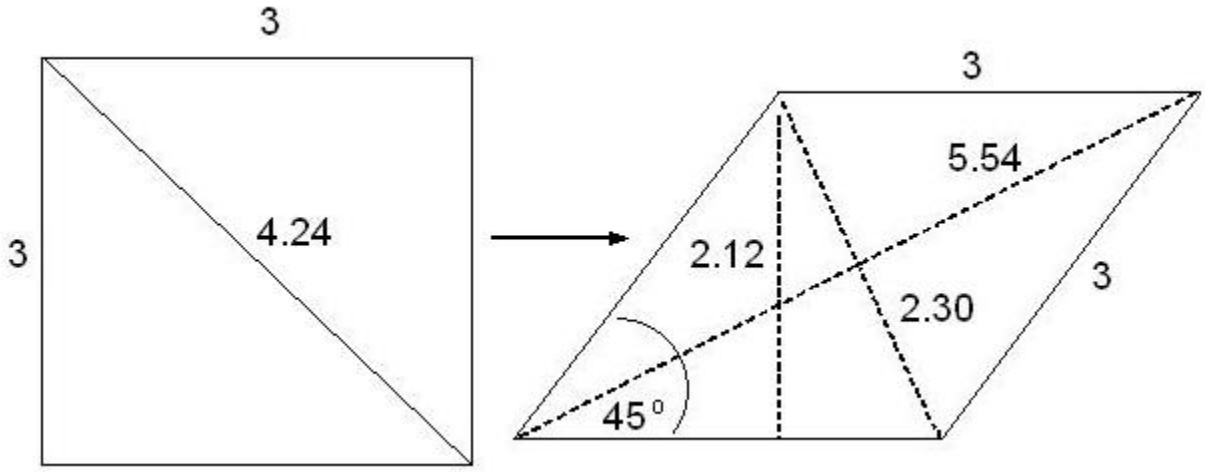

Figure 6-16 Schematic of 3 in. x 3 in. tile undergoing a 45 degree rotation

This diagonal shortens to 2.30 in. when the tile is rotated 45 degrees while the opposite diagonal lengthens to 5.54 in. According to Eq. 6.1, this results in a compression of 45.8% of the shortened diagonal.

$$100\% \cdot \frac{L_{initial} - L_{final}}{L_{initial}} = \%\ compressio\,n$$

$$\frac{4.24 - 2.30}{4.24} = 45.8\% \tag{6.1}$$

The value found in Eq. 6.1 is not, however, the amount by which the tile needs to be pre-strained. The tile needs to be pre-strained by the same amount of tension required to bring the diagonal of the tile from 2.30 in. back to its initial length of 4.24 in. This way, after a 45 degree rotation, the tile will essentially be in its relaxed state along the diagonal, as it was prior to its pre-strain. The simple calculation required to achieve this pre-strain is shown in Eq. 6.2 below. This is essentially the same equation as Eq. 6.1, except that the initial state is when the tile has 0% pre-strain.

$$100\% \cdot \frac{L_{initial} - L_{final}}{L_{initial}} = \%\ compressio\,n$$

$$\frac{2.30 - 4.24}{2.30} = -84.3\% \tag{6.2}$$

This can also be expressed more simply in terms of elongation.

$$\frac{L_{initial} - L_{final}}{L_{initial}} = \frac{L_i - \left(L_i + \Delta L\right)}{L_i} = \frac{-\Delta L}{L_i} = elongation \tag{6.3}$$

This means that the tile needs to be pre-tensioned to a new shape such that if it were to endure a 45 degree shape-change-inducing rotation, the length of its new diagonal would be 1.843 times its initial diagonal length.

Since pre-tensioning along a diagonal is unnecessarily difficult, the tile will be tensioned along both its x and y axes instead. The idea of superposition is applied as well, meaning that first the x direction will be tensioned and then the y direction will be tensioned. Shown below in Figure 6-17 is a rough drawing showing the simple geometry involved in calculating the needed x and y component pre-strains.

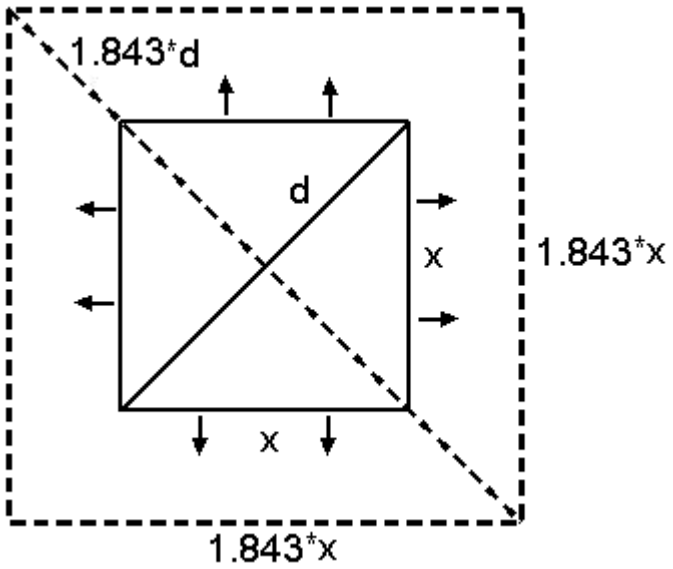

Figure 6-17 Drawing representing pre-tension components

If the initial length of a side of the tile is 1.63 in., then the length of a side of the tile after an 84.3% strain will be 3.in, which is the desired length. This corresponds to the desired size tile (after it has been pre-strained), however, a larger initial tile will be used for pre-straining to ensure uniform strains throughout the tile. This is discussed further in the following section.

6.2.1 ANSYS testing to determine initial SMP tile shape

After finding the required X and Y strains to offset the out-of-plane buckling incurred from the shape-change process, the next step was to determine an initial tile shape that could produce these strains uniformly throughout a desired 3 x 3 in. square shape. Note that, again, the SMP plate will be 0.25" thick, as with every other SMPP sample tested in this thesis. This was done using an iterative process in ANSYS.

Regardless of what the initial shape of the tile is prior to pre-straining, the center 3 in. x 3 in. section of the tile was all that was important in the end. This was because the final tile sub-section piece still had to remain a 3 x 3 inches so that it was able to fit into the tile array comprising the skin on the wing of a theoretical morphing aircraft. Consequently, as long as a 3 x 3 inch section of SMP could be machined out of the final specimen, then the initial shape of the SMP tile held no bearing. With this in mind, the initial size of the tile before pre-straining was chosen to be a 3 x 3 inch tile. This means that the size of the tile after the required pre-strain of 84.3% was about 5.5 x 5.5 inches. Clearly this was much larger than the needed 3 x 3 inch tile. There were, however, two important advantages in selecting such an oversized tile. Firstly, it would have been difficult to induce the relatively large required pre-strain on the SMP tile without ripping or damaging the material in any way. Since only the center 3" x 3" square of the sample was important after pre-straining, tears caused from gripping and stretching on the ends of a larger tile would not affect the inner 3" x 3" square. It was felt that too small of an initial tile might see a tear of the material overlap into the center area. The oversize allowed a good amount of room for error. It is shown later that this indeed proved to be useful, although tearing of the SMP still posed a couple of other problems. The

second reason was that there were already molds and mold pieces available that were tailored to a 3 x 3 inch tile.

The first ANSYS test done was to verify the pre-strain calculations above. SOLID95 elements and 15,000 nodes were used to comprise the mesh of the tile volume. The thickness of the plate was set to 0.25". Strains in the form of area displacements were imposed on the tile ends. The magnitude of the displacements was set to match that of the calculations above, e.g., 1.25 inches on the ends of the 3 x 3 inch tile. The first principle strain was then plotted to show the combination of X and Y strains. As shown below in Figure 6-18, the strain values from ANSYS match those calculated above (the 1% difference results from rounding error).

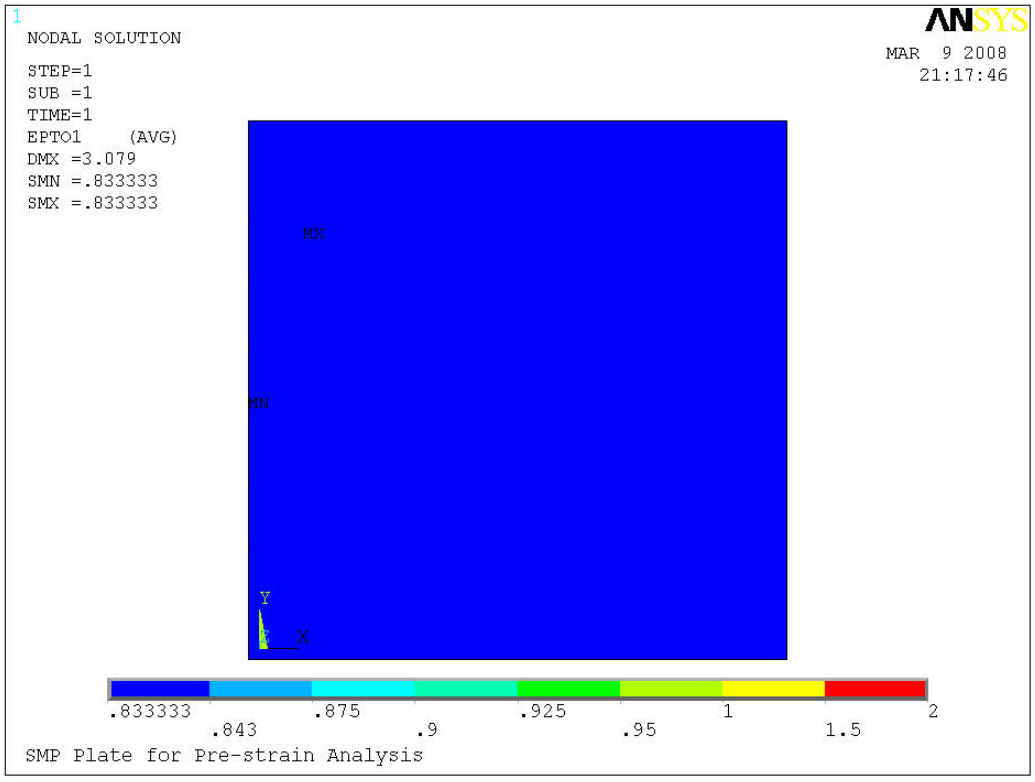

Figure 6-18 1st principal strain ANSYS plot of 3 x 3 inch tile tensioned 1.25 in. in all directions

It was recommended by Dr. Roy Marangoni (University of Pittsburgh, Mechanical Engineering) that, when bi-axially pre-straining a plate, a square shape with flanges produces the most uniform stress/strain distribution (with the pre-straining device attached to the flanges). Also, in order to physically pull the SMP during the pre-tensioning process, there needed to be somewhere for the machine to grab onto. Note that adding flanges to the square tile would increase the length by which the tile needed to be pre-tensioned in order to achieve the required 83.4% strain. ANSYS was used to determine optimal flange shapes and sizes as well as the new required pre-tension length for achieving 83.4% strain.

The flanges on the sides of the tile in the first ANSYS model were initially modeled as rectangles. The lengths of the flanges were determined by comparing the effects of several sizes. The smallest flange size was set to 0.4 inches, as this was about the width of the gripping mechanisms attached to the plate. The reason for this width is explained later in the experimental testing section. Pre-strains in the form of nodal displacements on the volumes of the ends of each of the flanges were imposed. The displacements values imposed on the flanges were chosen such that the minimum strain in the SMP plate was 84.3%. First principle strain contour plots with customized contour ranges to emphasize the maximum allowable strain (200%) and desired strain (84.3%) were then generated from the linear solution. As shown below in Figure 6-19, increasing the flange size offered seemingly no benefit. Note that the blue contour corresponds to where the SMP is gripped and that the center circular contour corresponds to the desired 83.4% strain. Also, the side pre-tension displacements were increased as the flange size was increased in order to achieve a minimum of 83.4% strain in each case.

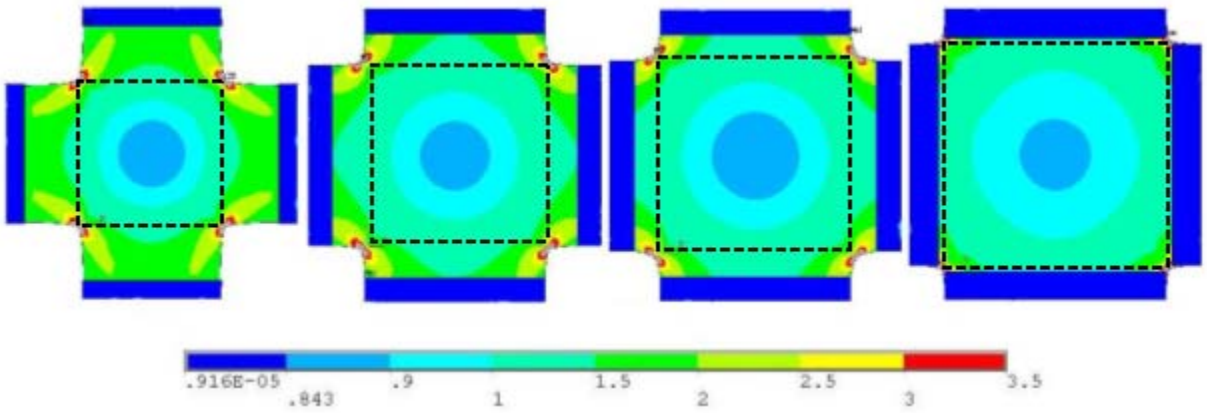

Figure 6-19 1st principal strain contour plots generated by ANSYS: from right to left, increasing flanges sizes are 0.4", 0.6", 0.8" and 1.4", respectively (not drawn to scale). Black outlined boxes corresponds to inner 3" x 3" area. Note that neither the dimensions of the inner square nor the width of the flanges are changed from case to case.

Looking at Figure 6-19, it appears that the inner 3" x 3" square in each case has nearly identical strain contours and that the corners in each case look nearly identical as well. Since there was no apparent benefit to an increased flange size, the flange size used in experimental testing was chosen to be 0.6 inches, which is slightly larger than the minimum of 0.4 inches, to allow for some overlap of gripping. Also evident in Figure 6-19 is the large amount of strains occurring in the inner corners between flanges. In order to alleviate the large stress concentration in the corners, filets were added to each inside corner. The radius of the filets is the same as the protruding length of the flanges (0.6"). As shown below in Figure 6-20, the filets reduce the stresses seen on the inner corners. Note that the filets also provide a slightly more uniform strain distribution throughout the tile, specifically in the center area, from which the desired 3 x 3 inch section would be cut.

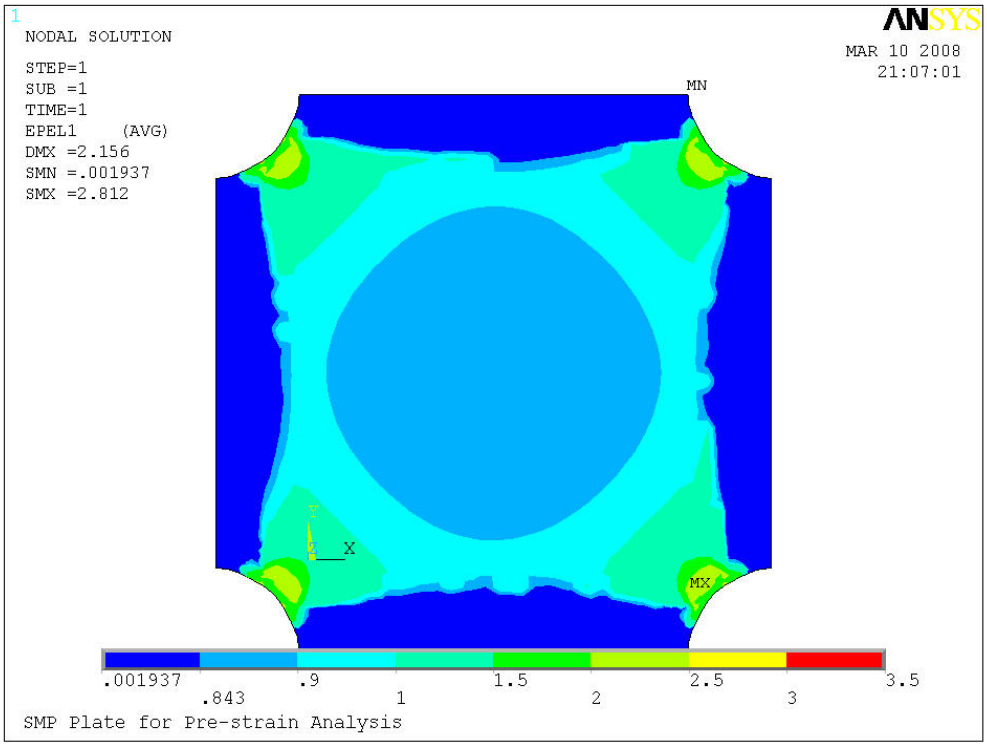

Figure 6-20 Strain contour plot of 3 x 3 in tile with filleted flange corners undergoing pre-strain

The pre-tension used on all sides in Figure 6-20 above was 1.5 inches. A prototype tile, shaped like that of Figure 6-20, will be created in the following section.

6.2.2 Fabrication of SMP tiles for buckling reduction

An aluminum mold (Figure 6-21) was first created to mimic the previously discussed ANSYS model (Figure 6-20). Dimensions of the cross-section of the mold are identical to those used in the above ANSYS model (3" x 3" square center, 0.60" flanges with 0.60" radius filets). The height of the mold was chosen to be 1" so that a few cross-sections of the plate could be created at once.

Figure 6-21 Mold used for fabrication of tile intended for shear testing

The first few attempts of SMP plate fabrication resulted in unusable specimens. Shown below in Figure 6-22 is a picture of the void-filled specimen.

Figure 6-22 Picture of unusable first few SMP plate specimens for shear testing

After some trouble-shooting with CRG Industries, it was decided that due to the large thickness of the SMP plate being cured, the inherent exothermic reaction involved in the curing process of Veriflex produced a large temperature gradient within the material. To solve this problem, a customized smoother cure cycle was used. At a rate of 1^{o}C/minute, the temperature

of the mold (containing the SMP) was increased from 23°C to 60°C. After staying at 60°C for 8 hours, it was then brought to 85°C again at a rate of 1°C/minute. It was left at 85°C for 26 hours and 58 minutes, resulting in a total cure cycle of 36 hours. It was found that this cure cycle effectively solved the mentioned problem. After slicing the specimen in thirds, an end mill was used to ensure that each plate was flat. The result of one of the SMP plates is shown below in Figure 6-23.

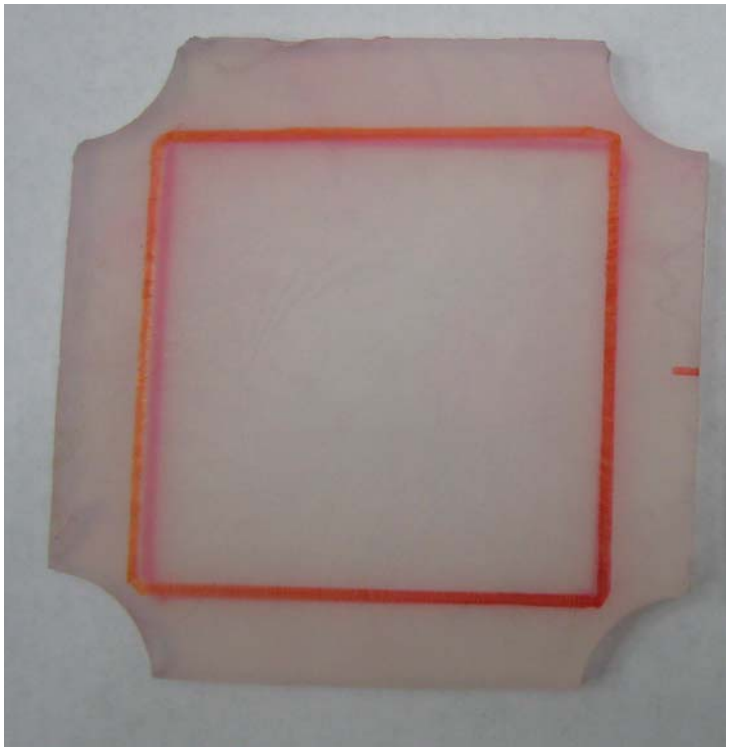

Figure 6-23 Final resulting SMP plate to be used for shear testing

Note that the red outlined box contains the area corresponding to the center 3" x 3" tile. This is the tile that will be used for pre-tensioning and in turn for the shear testing (shape-change).

7.0 EXPERIMENTAL TESTING

A variety of experimental testing was done in order to verify analytical findings as well as bring to light some new findings. No experimental testing was done to characterize out-of-plane deformation of the either the SMPP or the FESMPP in its sheared state due to an aerodynamic load. Since the primary concern associated with shearing the tile was with the buckling effect, testing the tile against an aerodynamic while in its rhombic was unnecessary. Also, there were no finite element or analytical models created for a rhombus-shaped tile subjected to a transverse load to gauge against experimental results in order to determine validity. Also note that the testing assembly could not simulate an aerodynamic load and function as an oven, so no experimental out-of-plane heated homogeneous SMP deflection tests were conducted.

7.1 SMPP AND FESMPP TESTING AGAINST SIMULATED AERODYNAMIC LOAD

Using a fourth generation fiber-embedded shape-memory polymer tile (Section 6.1.4), a testing assembly was created (Figure 7-1). For testing of the homogeneous SMP plate, a third generation fiber-embedded shape-memory polymer tile without the embedded fibers was used.

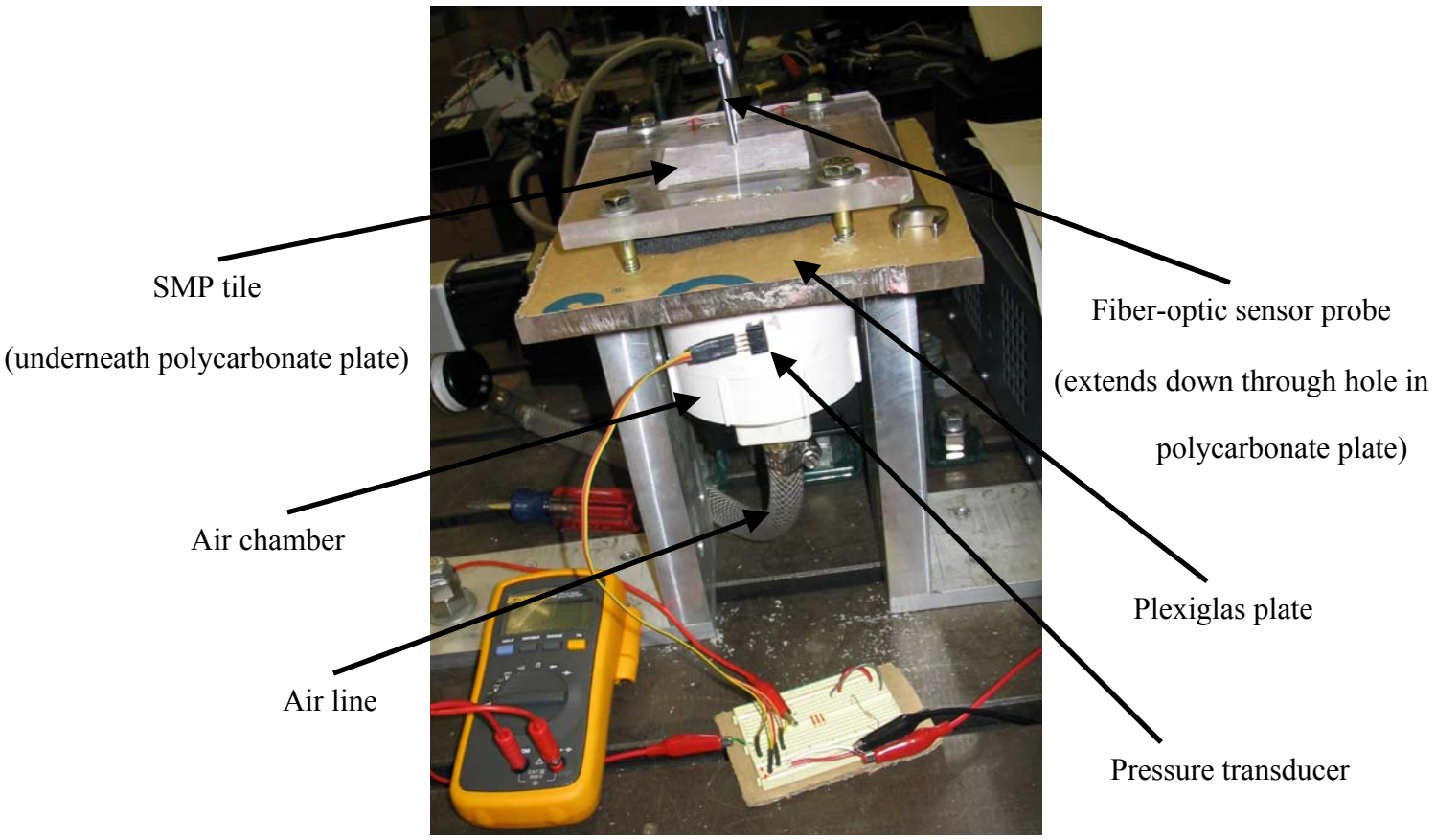

Figure 7-1 Aerodynamic testing assembly for FESMPP and SMP tiles

The air chamber was glued to the bottom-side of the Plexiglas plate and sandwiched between two metal 'L' plates clamped to a workbench. A hole was drilled in the center of the Plexiglas plate

The test assembly shown above uses an MTI-2100 Fotonic^{TM} Sensor and a PX26-005GV differential pressure transducer. The sensor was calibrated for small displacements. The pressure inside the air chamber was set to 2.7 psi (aerodynamic load) as per corresponding output from the pressure transducer (30.8 mV). The displacement (in mils) was then read from the Fotonic sensor's corresponding output module. This procedure was done for the SMPP in its un-heated state and for the FESMPP in both its heated and un-heated states. The

experimental results for out-of-plane deflection of the center of each plate are listed below in Table 7-1. Also listed in Table 7-1 are the corresponding results obtained from both the finite element ANSYS models and analytical models.

Table 7-1 Out-of-plane deflection at center of SMPP and FESMPP above and below transition temperature

	Out-of-plane deflection at center of plate (mils)			
	SMPP		FESMPP	
	Un-heated	Heated	Un-heated	Heated
Analytic	1.113	4940	0.877	3.51
ANSYS	1.239	602	1.096	121
Experimental	1.1	Not tested	0.9	137

Incorrect linear results (actual physics are non-linear)

Note that the experimental deflection results listed are the average of a set of five measurements, with each individual measurement have a very small deviation (too small for the resolution of the Fotonic sensor) from the group's average. For the un-heated cases, the deflections produced from the analytical model matched the experimental results more closely than those of the ANSYS models. For the heated FESMPP case, the result from the ANSYS model had a difference of 11.7% from the experimental result.

7.2 BIAXIAL PRE-TENSIONING OF SMP TILE FOR BUCKLING REDUCTION

Bi-axial pre-tensioning of the SMP plate was accomplished with the use of superposition. The SMP plate was uni-axially pre-tensioned in one direction, clamped, and then pre-tensioned in the second planar direction. As per Section 6.2, the SMP plates were initially pre-tensioned 84.3% in each direction. This produced some problems and so SMP plates were then pre-

tensioned 41.3% to accommodate a shear-inducing shape-change angle of 30^o (as opposed to 45^o). This method is further explained later in this section.

7.2.1 Pre-tensioning of the SMP tile with hole-patterned grips

Since the SMP tiles needed to be in their heated state during the pre-tension process, an assembly that could induce loads within an environmental chamber was used. Shown below in Figure 7-2 is the MTI 5K load machine (black) and corresponding BEMCO environmental chamber (blue).

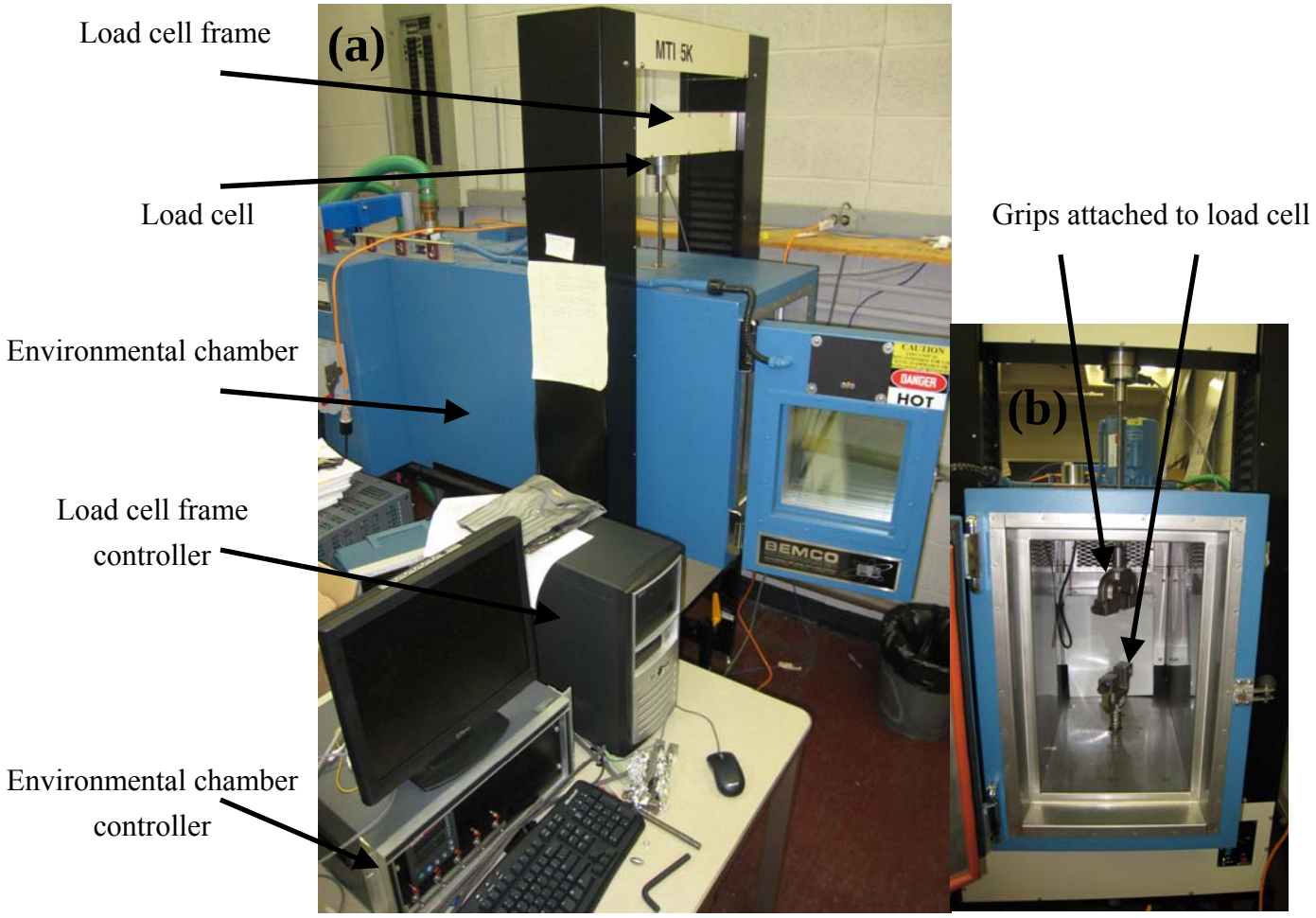

Figure 7-2 (a) MTI 5K load machine (black) and BEMCO environmental chamber (blue) and (b) inside view of environmental chamber

Using the SMP tiles created in section 6.2.2, fixtures were created to grip the sides of the SMP (as modeled with ANSYS in section 6.2.1) to ensure a secure grasp during the pre-tension process. These pre-tension grips were placed within the load cell grips contained within the environmental chamber. As per (Bortolin, 2005), the pre-tension grips were initially created as steel plates with a pattern of holes. Shown in Figure 7-3, screws were pierced through the thickness of the SMP and anchored on the outsides of the grips with a nut.

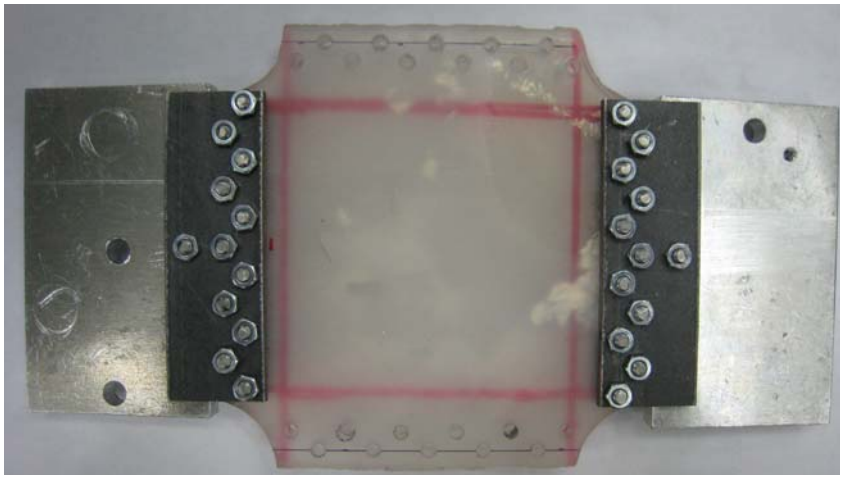

Figure 7-3 SMP plate with attached hole-patterned grips and anchored screws

The pattern of screws was created so that as the thickness of the SMP became smaller (via Poisson's ratio), screws pierced through the thickness of the SMP and anchored within the grips would hold it in place. Two small plates were attached to either side of the grips so that the load cell grips could pull on the center axis. The screws and nuts were all sufficiently tightened with a hex key. The SMP grip assembly was placed into the load cell grips within the environmental chamber. The temperature inside the chamber was set to 90^{o}C and the SMP was left inside to heat for 15 minutes to ensure it sufficient heating. At a velocity of 0.4 inches/minute, the upper grip of the load cell stretched the clamped SMP plate to the desired length. Shown in Figure 7-4 below is the SMP after being tensioned in one direction.

Figure 7-4 SMP plate after being tensioned in one direction with hole-patterned grips

As it turns out, this technique caused more damage by creating tears in the SMP than it did benefit by holding the SMP in place. Instead of using this technique to see the results of the bi-axially pre-tensioned case, a different method of clamping the plate was used.

7.2.2 Pre-tensioning of SMP tile with solid grips

It was felt that patterned holes through the SMP were not necessary to prevent the SMP from slipping during the pretension process. Instead, flat rectangular plates were tightened incrementally during the pre-tension process as the SMP's thickness shrank more and more. This method, although more tedious than the previous, prevented the SMP from slipping in the grips as well as preserved the integrity of the gripped area of SMP.

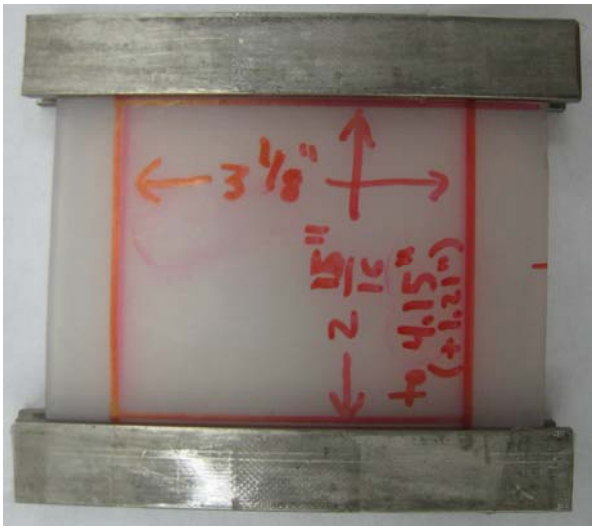

Figure 7-5 SMP plate with solid grips (red lettering is just for percentage of strain reference)

The tile was once again placed into the load cell grips inside the environmental chamber and heated to 90^{o}C. Before starting the pre-tension process, the grips were clamped down by hand-tightening the load cell grips with a hex key. The pre-tension process was set in motion, again tensioning at a rate of 0.4 inches/minute. The loading was paused and the clamps were re-tightened roughly every 0.25" to make sure there was no slipping between the SMP and the insides of the grips. The result after a full uni-axial pre-tension is shown below in Figure 7-6. No tearing occurred and the sample appears to be intact.

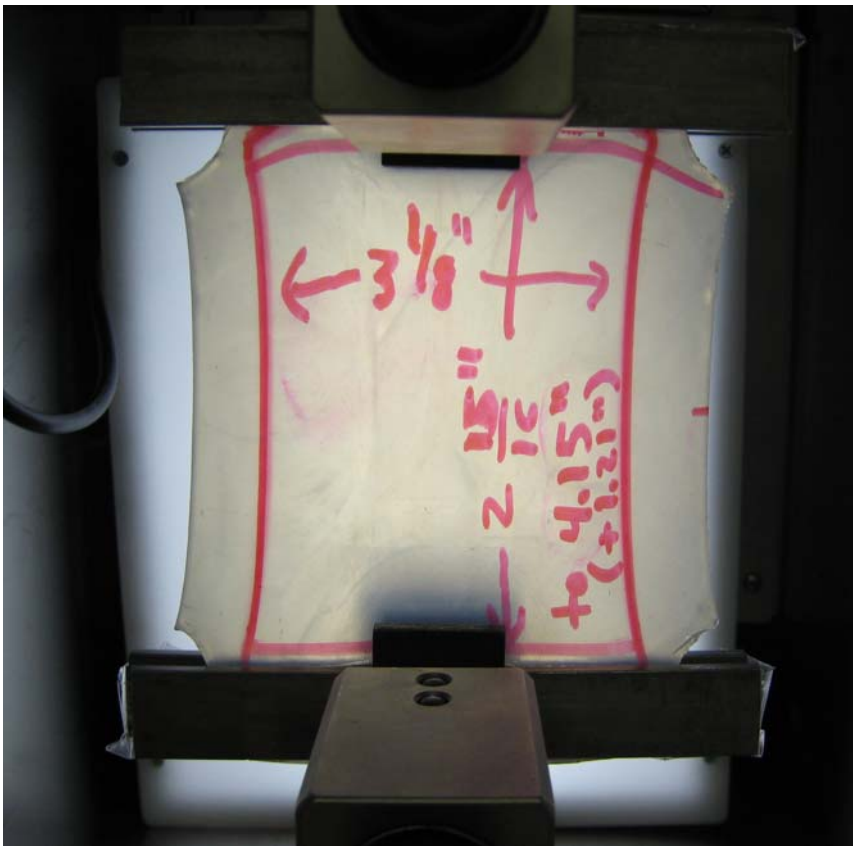

Figure 7-6 SMP plate inside environmental chamber after pre-tensioning with solid grips

The SMP plate was cooled with the grips attached in order to maintain the pre-tensioned state. In order to maintain the first pre-tension while inducing the second, holes were drilled into the SMP plate and crossbars were attached. As shown in Figure 7-7, this prevented the SMP from rebounding inward during the second planar pre-tension and also allowed the SMP to be stretched along the axis perpendicular to the crossbars.

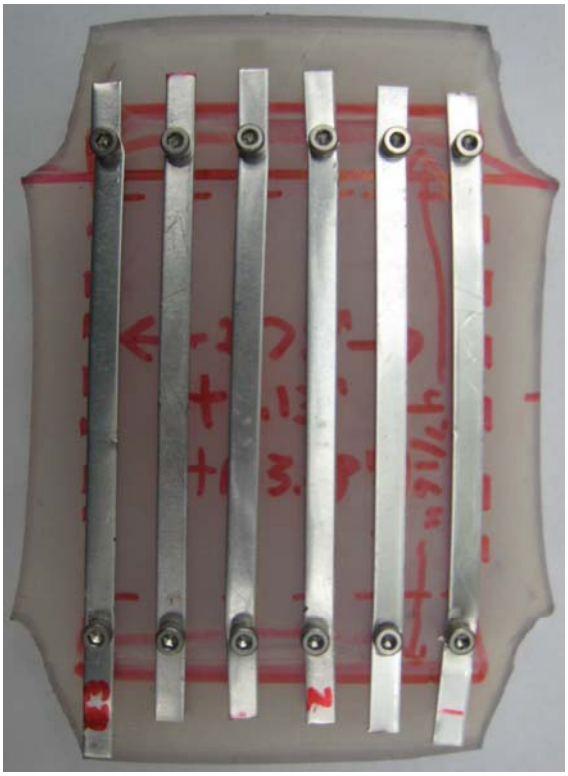

Figure 7-7 SMP plate after first pre-tension with attached crossbars

The mentioned danger with drilling through holes in the SMP was and still is that tearing will occur between the holes. It was thought that since far fewer holes were used, the danger would have been much more remote. Shown in Figure 7-8 below, it turned out that tearing in between the holes did indeed occur when applying 84.3% pre-tension in the second planar direction.

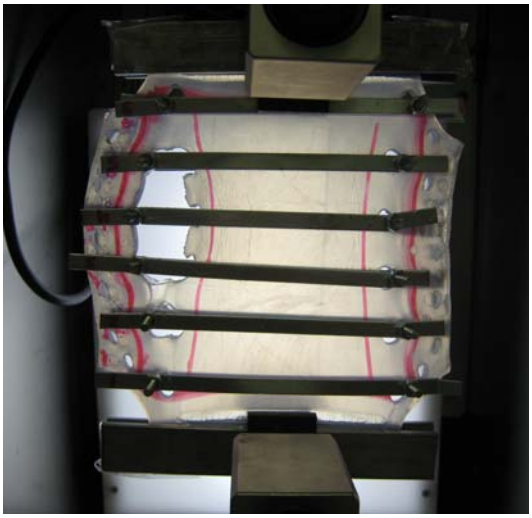

Figure 7-8 SMP plate while in environmental chamber showing large tear as a result of pre-tension in the second planar direction

While the large void in the SMP clearly made the sample unusable, it is interesting to note that the reason it became unusable was not as a direct result of the presence of the void, but rather as a consequence of the void. Since the crossbars maintained their length, the inside 3" x 3" center of the SMP was forced to lose its pre-tension in the first planar direction. This means that as the void grew larger, the pre-tension in the SMP decreased. For fear of having another method go awry, this same method was used for a second round of testing on a new sample, however, the pre-strains induced in each planar direction were set to 41.3% (using the method described in section 6.2). This new amount of pre-tension corresponded to a shear-inducing shape-change angle of 30^{o}, as opposed to the 45^{o} angle associated with the previously used 84.3% pre-strain. The lessened pre-strain also meant that the stresses on the SMP were much lower than in the previous case. Using the exact same method as described above, the bi-axially pre-tensioned SMP sample is shown below in Figure 7-9.

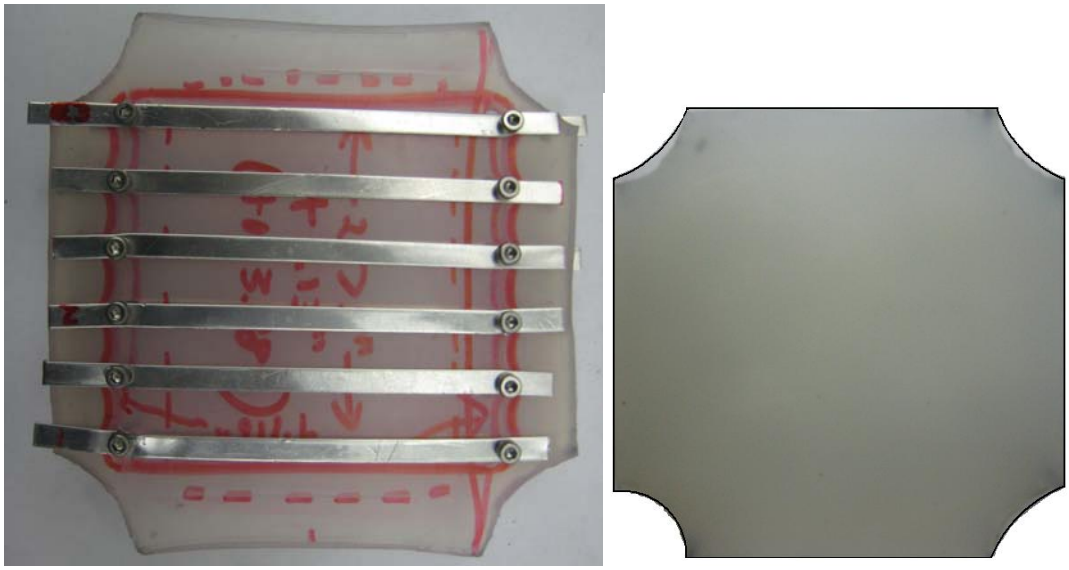

Figure 7-9 (Left) SMP sample after 41.3% pre-strain in both directions and (right) SMP sample shape before any pre-strain

Figure 7-7 shows what Figure 7-9 looked like before undergoing pre-strain in the second planar direction. The red lines between the crossbars in Figure 7-9 showed slight evidence of bowing when compared to Figure 7-7, which indicated that a slight amount of pre-tension was lost in the first planar direction of pre-strain between the crossbars as the sample was pre-strained in the second planar direction. This was expected and, judging from the amount of bow of the red lines, thought to be negligible at the time.

7.3 INDUCING SHAPE-CHANGE ON PRE-TENSIONED SMP TILE

A fixture was created to shear the bi-axially pre-tensioned SMP sample 30^{o} into a rhombus shape. The fixture was modeled after a similar fixture used in (Bortolin, 2005). A SolidWorks

drawing was created and the fixture was then machined from 6061 Aluminum. Shown below in Figure 7-10, the fixture was able to independently clamp each side of the SMP sample.

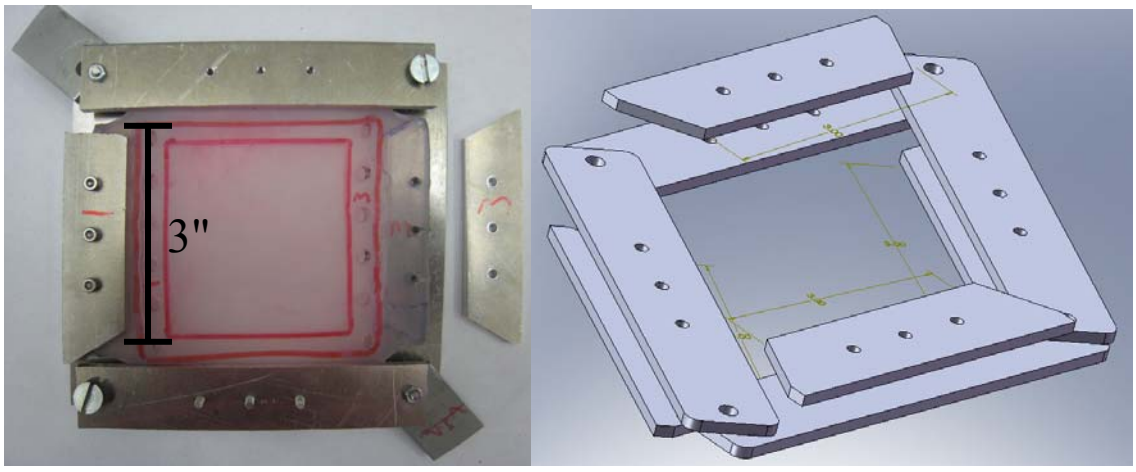

Figure 7-10 (a) SMP sample inside pre-tensioning fixture (ignore the outer red square line) and (b) SolidWorks drawing of pre-tensioning fixture assembly

Note that the same SMP sample shown in Figure 7-9 is used in Figure 7-10, except that the red lines have been erased and redrawn so a center 3" x 3" square may be tracked once again. Clamping on each side of the SMP plate was done by sandwiching the SMP between the lower and upper half of the fixture. Three screws were then tightened via three corresponding taps made in the lower half of each fixture piece. The resulting clamped portion of the SMP sample includes the desired center 3" x 3" square.

The SMP sample (with attached shearing fixture) was placed inside the environmental chamber and its corners were secured in between the load cell grips (Figure 7-11).

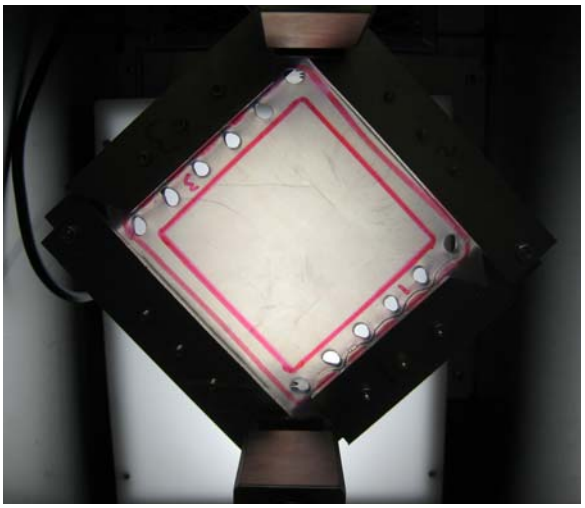

Figure 7-11 SMP sample with attached pre-tension fixture in environmental chamber.

At a rate of 0.4 inches/minute, the load cell grips pulled on the diagonal of the SMP plate till the sample was sheared by 30^{o}. The result is shown below in Figure 7-12.

Figure 7-12 Close-up of 41.3% bi-axially pre-tensioned SMP sample after shearing 30^{o}

As evident from Figure 7-12, it appears that the 41.4% bi-axial pre-tension was unable to prevent the onset of buckling. However, it was realized that perhaps the reason the pre-tension was unable to counteract the buckling behavior may have been because some of the pre-tension was lost at some point during the shearing process. In order to determine whether or not this was the case, the sample was unconstrained and reheated, thereby inducing the memory effect and causing the plate to return to its bi-axially pre-tensioned square configuration prior to shearing. The outlined red square in the middle of the plate was measured to determine whether or not it had shrunk from its initial 3" x 3" shape. Shown below in Figure 7-13 is the SMP sample being measured.

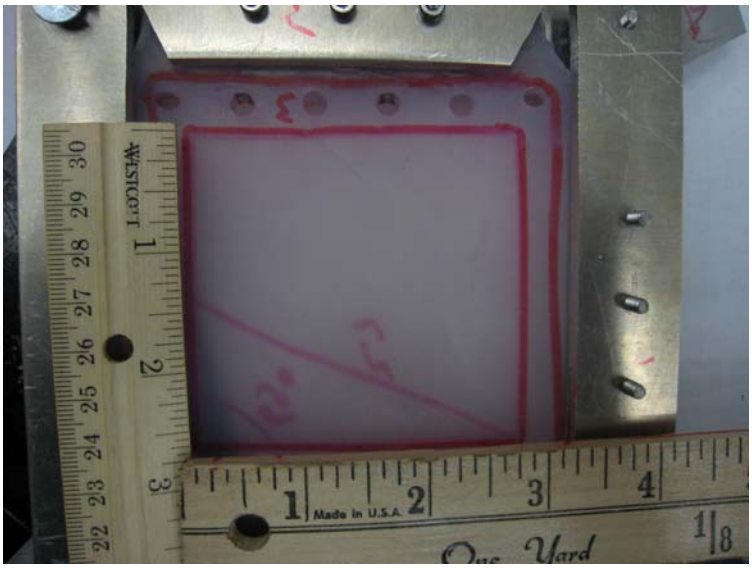

Figure 7-13 SMP sample after returning from its 30^{o} sheared state

It was found that the dimensions of the 3.11" x 3.09" initially sized square had been reduced to 2.78" x 2.93", respectively (2.78" in the vertical direction of Figure 7-13). Looking at Figure 7-11, it is clear that the holes drilled in the SMP for the crossbars used in section 7.2.2 stretched at some point during the shearing and pre-tensioning process, causing the inner

SMP to relax, compress and lose some of its tension. Comparing the initial size of the red-outlined square to the size after shearing, the SMP was compressed 10.6% in the first direction and 5.18% in the second direction (via Eq. 6.2). This meant that the SMP tile was only actually pre-strained enough to counteract buckling behavior up until a shape-change angle that corresponded to about 10.6% less than the originally intended pre-strain of 41.3%. Using the reverse of the method described in section 6.2.1 for a 3.11" x 3.09" square pre-strained by 30.7%, it was found that the sample should have been able to withstand a shear-induced shape-change angle of 65.4^{o}. In order to verify this, the sample from Figure 7-13 was sheared to an angle of about 65^{o} to see if the onset of buckling was, in fact, resisted. Shown below in Figure 7-14 is the sample after being sheared 24.6^{o}.

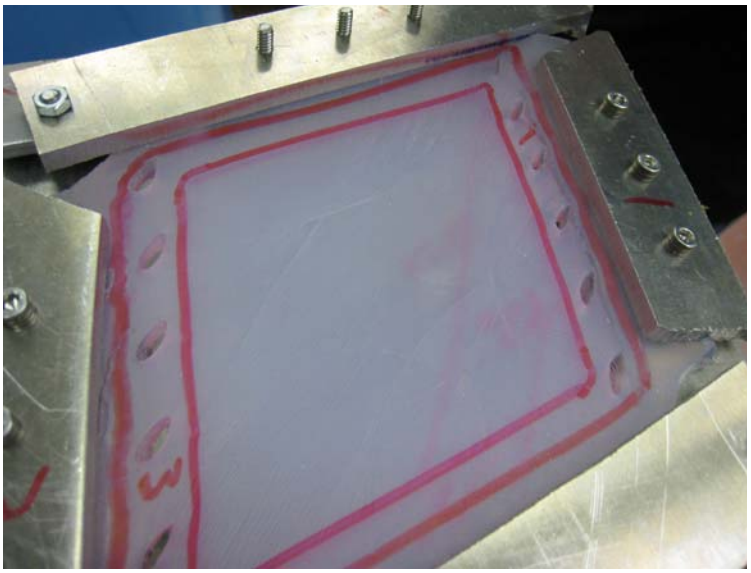

Figure 7-14 SMP sample after being sheared about 25^{o} to an angle of about 65^{o}

Looking at Figure 7-14, the unintentionally induced pre-strain of 30.7% on the SMP plate was able to delay the onset of buckling up until an angle of about 65^{o}. As a comparison,

Figure 7-15 shows one of the specimens with zero pre-tension after only a very slight shear-induced shape-change (<5 degrees). As expected, buckling in the sample occurs significantly and immediately.

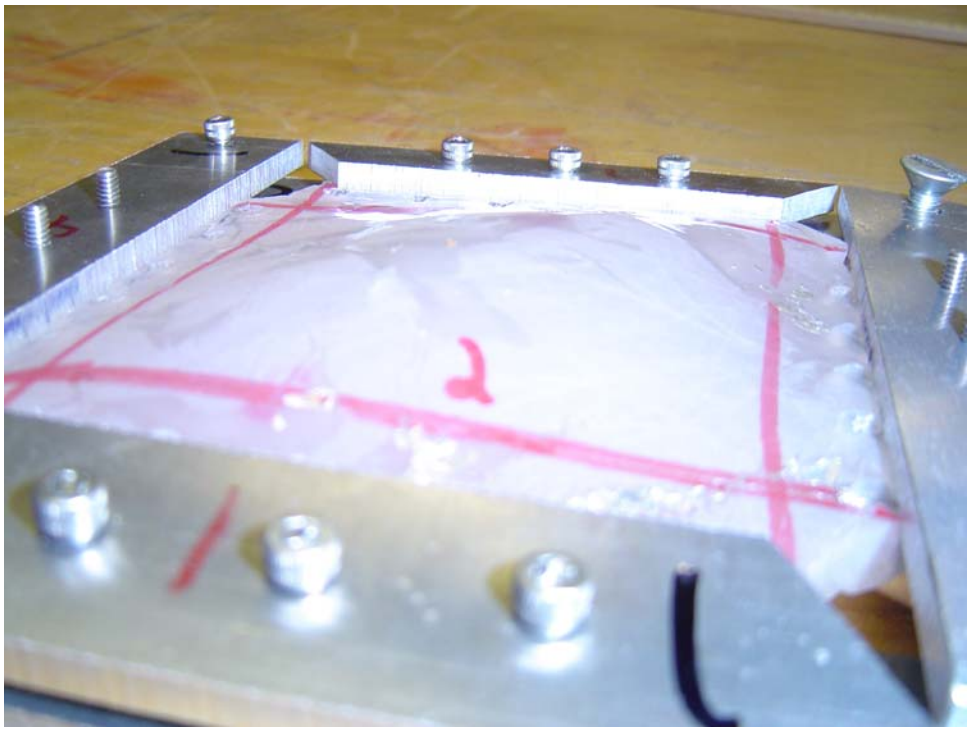

Figure 7-15 SMP Sample with zero pre-tension showing large buckling after only slight shape-change angle (camera flash was used to better show contour)

8.0 POWER REQUIREMENTS

Several finite element models will be created to determine the power and energy requirements associated with heating and shearing the tile. ANSYS scripts are listed in Appendix A.

8.1 POWER REQUIRED TO HEAT SMP PLATE VIA EMBEDDED FIBERS

8.1.1 ANSYS modeling to determine required heating times

Several finite element ANSYS models were created to specifically address the length of time that the fibers in the FESMPP needed to be heated in order to bring the entire SMP plate up to its transition temperature. Two-dimensional models were used since the direction along the fiber length had no bearing on the heating process since the fibers radiate heat radially. Along with the ANSYS models, some calculations were made to determine the power required to heat the wires to the needed temperature for the necessary length of time. The additional calculations, which were merely extensions of the Nichrome material properties located in Table 3-1 and Table 3-2, also helped in determining which diameter of Nichrome wire should be used. With these tools at hand, determining the power required to heat the fiber-embedded shape-memory polymer plate was approached as a relatively simple optimization problem.

There were several limitations that had to be incorporated into the model to accommodate the properties of the nickel-chromium fiber and shape-memory polymer matrix composing the fiber-embedded plate. First, the maximum working temperature of Veriflex (the shape-memory polymer used) is 135^{o} C according to CRG Industries. In order to prevent the temperature of the Veriflex from rising above 135^{o} C, the Nichrome fibers were set to a maximum heat of 135^{o} C. Also, since the end-user application of the FESMPP is for use in a morphing aircraft wing, the maximum time allowed for the SMP to reach its transition temperature was kept under 60 seconds to produce more realistic results. Variables left for modification are now down to the radius of and spacing between the Nichrome fibers. Note that the total length of the Nichrome fibers will be a function of the spacing between the fibers while the input power will be a function of the total length and desired temperature. The diameter of the Nichrome fibers will be kept between 30 gauge and 20 gauge for the reasons mentioned in the "NICHROME" section and also because it was assumed that if the wire diameter became too large, it may interfere with the shape-change process by creating voids. However, if a wire diameter outside the specified range is desired, the method can easily be applied to those as well.

To illustrate the primary difference of the effect that different diameter wires have on heating, the smallest diameter (30 gage) and largest diameter (20 gage) wires are both modeled as the heating elements of the FESMPP in ANSYS. While a more rigorous approach could be taken to determine the maximum and minimum acceptable gauge sizes without compromising structural integrity, the method thereafter would be identical and so only a rough estimate was used to determine the range. Shown in Figure 8-1 below is two contour plots of the nodal temperature throughout a 1.5 in. wide SMP plate after 60 seconds of heating. Note that the

contact resistance between the SMP and the Nichrome is modeled as perfect and that the film coefficient used for the interaction between the SMP and surrounding air corresponds to fairly laminar air (17.2W/m^2/K)

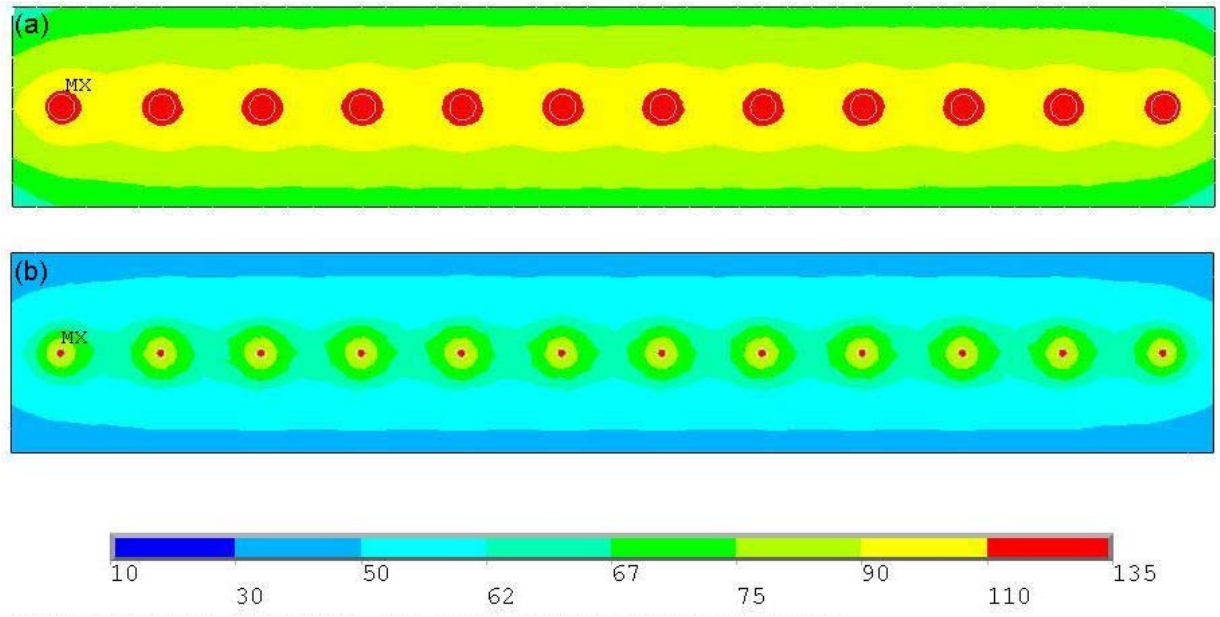

Figure 8-1 2-D ANSYS temperature (^{o}C) contour plots of 135^{o}C (a) 20 gauge Nichrome wires and (b) 30 gauge Nichrome wires heating SMP over 60 seconds (both with wire spacing of .125")

As shown in Figure 8-1, the smaller diameter wires failed to heat the SMP to its transition temperature (62^{o}C) while the larger diameter wires heated the entirety of the SMP plate to its transition temperature. It becomes clear that the spacing between the wires needs to be decreased as the wire diameter becomes smaller in order to compensate for the lack of heating.

Note that the width of the SMP plate in Figure 8-1 above is one half as wide as the actual SMP plate that will be used. This was done to simplify the ANSYS code, as it was very convenient to always use the same number of wires for each model (a plate twice as wide

would require twice as many wires). This alleviated the need to change the contact pairs each time a new model was created, which can be very time consuming. It was felt that this simplification had no impact on the final results since the nodal reference temperature used from this point on was located on the top middle of the surface of the cross-section. With this selection, the width of the plate should not matter so long as it's wide enough for the radiated heat to level off on the top middle of the surface. This will be explained and confirmed during the actual determinations of power requirements.

Every other number of wire gauge (20, 22, etc.) was examined using ANSYS to determine the power required to fully heat the SMP in the FESMPP to its transition temperature. Each gauge wire was spaced at a distance equal to its radius multiplied by a constant equal to a multiple of its radius (4x, 6x, etc.). This was done because it was found that 30 gauge wires spaced at a multiple of their radii produced nearly the same temperature contour as 20 gauge wires spaced at the same multiple of their radii (Illustrated below in Figure 8-2). Factors of four through ten were chosen because anything lower than a factor of four was thought to compromise structural integrity (4x radius spacing of 30 gauge wire means 32 mils between each wire) and anything more than a factor of ten would have resulted in a time greater than 60 seconds. Logically, the reasoning behind this also suggests that, fundamentally, standard Veriflex might not be the ideal choice for a morphing wing application where very short transition times are needed.

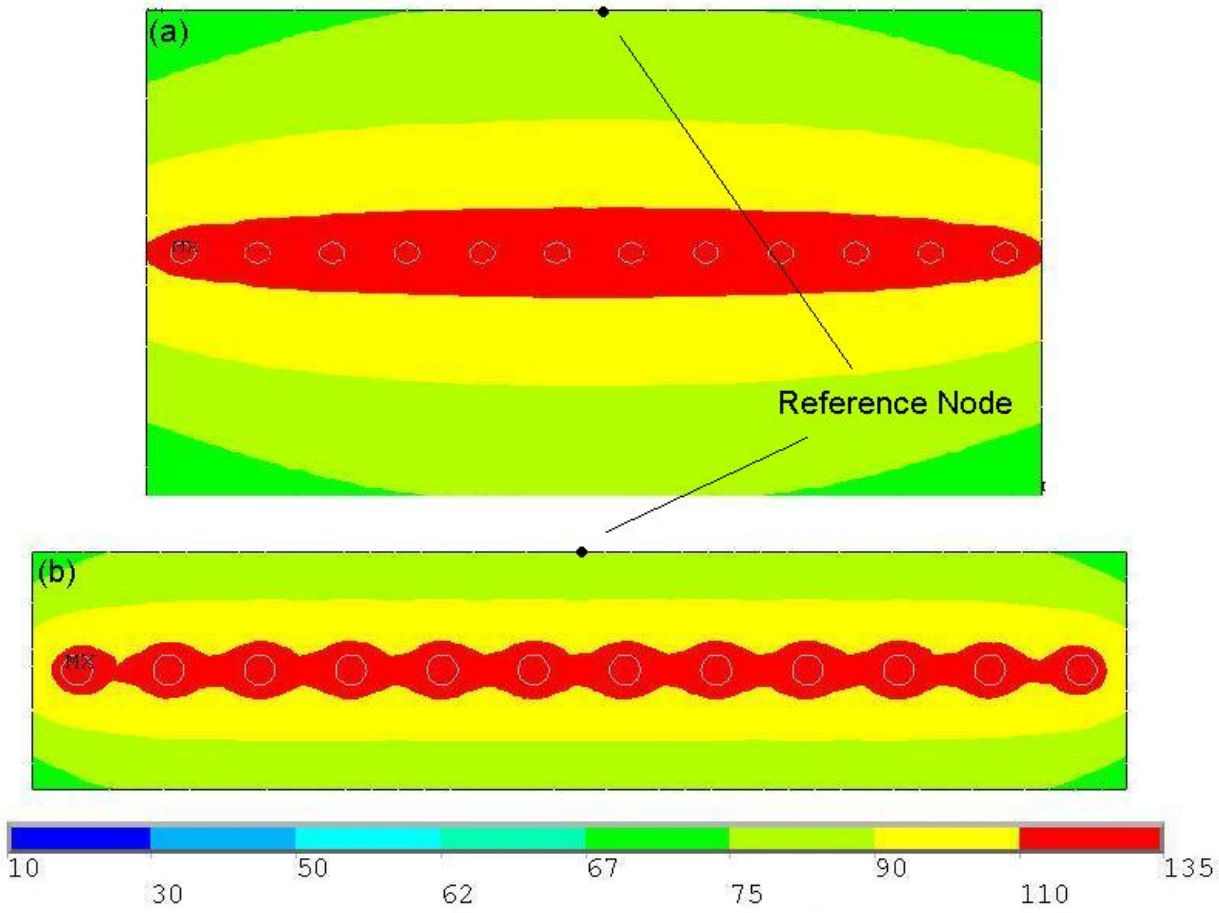

Figure 8-2 ANSYS representations of (a) 30 gauge wires spaced at 6x their radii and (b) 20 gauge wires spaced at 6x their radii. Note that the apparent discrepancy in widths is because the width of the plate in both cases is kept at 12x the wire spacing for simplification purposes as mentioned above.

A node in the middle of the top of the surface of the SMP plate was used as the reference point to determine when the plate reached its transition temperature. This was done to greatly simplify the model, as the overall width of the model became negligible for determining the time it took to achieve 62^{o}C as long as there were enough wires used. Since the corners of the FESMPP plate would experience very little deformation during shape change, it was deemed acceptable for the edges of those corners to not quite reach the transition temperature

Time-history post-processing was used in ANSYS to determine at what time the top middle node of the surface of the SMP reached 62°C for each case of spacing for each gauge wire. Below in Figure 8-3 is a graph showing a typical nodal temperature versus time relationship for the surface of the SMP.

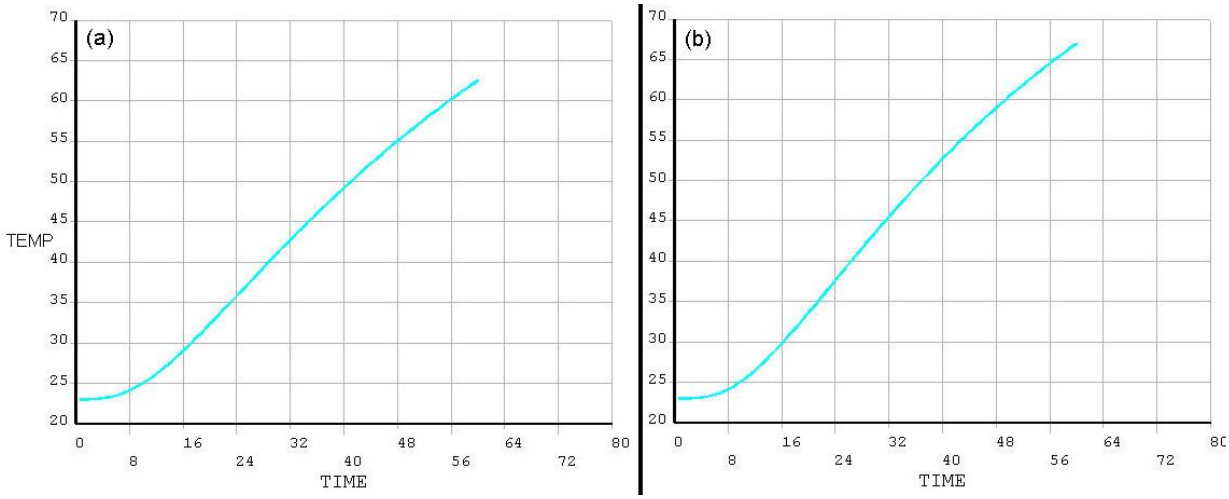

Figure 8-3 Temperature (°C) of top middle node vs. time (sec) for (a) 20 gauge wire and (b) 30 gauge wire spaced at 10x their radii.

The results for the required times are listed below in Table 8-1. These numbers will be used to determine the power required to heat the SMP to its transition temperature using the given wire radii and spacing.

Table 8-1 Times required for SMP to reach transition temperature with a given wire radius. Wire radii are given as a ratio of wire spacing to radius, denoted by 4x, 6x, 8x and 10x.

		Time (sec) required for top middle node to reach 62°C at spacing of given wire radius multiple			
Gauge	Radius (mm)	4x	6x	8x	10x
20	0.4064	33	40	49	60
22	0.3213	34	40	48	57
24	0.254	35	40	47	55
26	0.20195	35	41	47	54
28	0.16	36	41	47	53
30	0.127	37	41	47	52

Table 8-2 below shows the total length of Nichrome wire required to fill a 3 in. x 3 in. tile at the given radius and spacing. These numbers were calculated by first dividing the width of the SMP plate (3 in.) by the wire spacing to determine the total number of wires needed in a cross-section. This number was then multiplied by the length of the SMP plate, thereby effectively extruding the wires. Finally the total width of the SMP was added to this number to account for the external wire needed to connect the internal wires. This is also expressed in equation form below in Eq. 8.1.

Table 8-2 Total length of Nichrome required to heat the SMP to 62°C for given spacing of wire radius multiple for a 3 in. x 3 in. tile

		Total length of Nichrome wire required for given spacing of wire radius multiple for a 3 in. x 3 in. tile			
Gauge	Radius (mm)	4x	6x	8x	10x
20	0.4064	3.65	2.46	1.86	1.50
22	0.3213	4.59	3.09	2.34	1.88
24	0.254	5.79	3.89	2.93	2.36
26	0.20195	7.26	4.87	3.67	2.95
28	0.16	9.15	6.12	4.61	3.70
30	0.127	11.51	7.70	5.79	4.65

$$\left(\frac{width\ of\ SMP\ plate}{spacing\ multiple \times radius\ of\ wire}\right) \times width\ of\ SMP\ plate + width\ of\ SMP\ plate \qquad (8.1)$$

Note that using a spacing of 10x for the 20 gauge wire case means that 19 wires running axially through the plate are required to fill it with evenly spaced wires, while a 4x spacing for the 30 gauge wire case corresponds to 150 wires.

Using the total length of wire needed for the given wire radius with the given spacing, the resistance of the wire can be calculated and in turn the power required to sufficiently heat the SMP. However, since the chart in section 3.3 containing electrical power properties of Nichrome has current values listed for Nichrome in free air, it is necessary to create a list of

these values for Nichrome in Veriflex. Before doing this, however, a reproduction of Table 3-3 using analytical methods is first attempted to verify consistency.

8.1.2 Analytical reproduction of Nichrome electrical properties in air

A brief analytical model was created to relate the electrically generated heat in the Nichrome wire to the heat lost from the Nichrome wire to the air. Since the heat lost from the Nichrome to the air was equal to the heat electrically generated to keep the wire at equilibrium, the two values were set equal to one another, leaving current as the only unknown variable. An expression for the free-convection heat loss per meter to ambient air is given below in Eq. 8.2.

$$\frac{q}{L} = h\pi\, d(T_w - T_\infty) \tag{8.2}$$

where,

$\frac{q}{L}$ = Free-convection heat loss per meter of length (W/m)

h = Heat-transfer coefficient ($W/m^2/^oC$)

d = Diameter of Nichrome (m)

T_w = Temperature of Nichrome wire (^oC)

T_∞ = Temperature of ambient air (^oC)

The heat transfer coefficient, h, was calculated by using one of the "Simplified equations for air" in (Holman, 1981) for a horizontal cylinder subjected to free convection of laminar air ($10^4 < Gr_f Pr_f < 10^9$) at atmospheric pressure.

$$h = 1.32\left(\frac{T_w - T_\infty}{d}\right)^{1/4} \tag{8.3}$$

An expression for the heat lost from the wire due to radiation is given below in Eq. 8.4

$$q = \sigma\ \pi\ dT^4 \tag{8.4}$$

where,

q = Power radiated (W)

σ = Stefan-Boltzmann constant = 5.669 x 10^{-8} W/m^2/K^4

T = Absolute temperature (K)

Using Eqs. 8.2 - 8.4, the heat loss of one meter of each gauge wire is calculated for a wire temperature of 204°C and ambient air temperature of 23°C.

Table 8-3 Heat loss per meter for a given gauge wire at 204°C subjected to radiation and convective air at 23°C

AWG (Gauge)	Diameter (inches)	Diameter (meters)	h (W/m^2/°C)	q_{conv} (W)	q_{rad} (W)
20	0.032	8.13E-04	28.7	13.3	7.50
22	0.0253	6.43E-04	30.4	11.1	5.93
24	0.02	5.08E-04	32.2	9.32	4.70
26	0.0159	4.04E-04	34.2	7.84	3.72
28	0.0126	3.20E-04	36.2	6.59	2.95
30	0.01	2.54E-04	38.4	5.54	2.34

Using Ohm's Law, the electrical power supplied to the Nichrome wire can be expressed as $P = I^2 * R$. Since $q_{gen} = q_{lost}$, the heat loss can then be directly related to the electrical power supplied to the Nichrome wire as per Eq. 8.4.

$$q = h\pi d(T_w - T_\infty) = P = I^2 R \tag{8.5}$$

Using the resistance per meter values for each gauge wire listed in Table 3-5 and Eq. 8.4, the current required to heat a Nichrome wire at a given gauge diameter to 204°C in laminar convective free air at 23°C is found. Note that since the resistivity factor for Nichrome at 200°C is negligible (1.019), the change in resistance per change in temperature can be ignored.

Table 8-4 Analytically determined current required for a given gauge wire to maintain a temperature of 204°C in laminar convective free air at 23°C

AWG (Gauge)	Diameter (inches)	Diameter (meters)	h ($W/m^2/^oC$)	q_{conv} (W)	q_{rad} (W)	Resistance (Ohms/m)	Calculated current (A)
20	0.032	8.13E-04	28.7	13.3	7.50	2.16	3.10
22	0.0253	6.43E-04	30.4	11.1	5.93	3.46	2.22
24	0.02	5.08E-04	32.2	9.32	4.69	5.48	1.60
26	0.0159	4.04E-04	34.2	7.84	3.72	8.76	1.15
28	0.0126	3.20E-04	36.2	6.59	2.95	14.0	0.827
30	0.01	2.54E-04	38.4	5.54	2.34	21.9	0.599

Comparing the values of Table 8-4 to those found by the manufacturer (most likely through experimental testing) in Table 3-3, the analytically determined current values differed by 13% to 30% from those listed by the manufacturer. This suggested that there were some variables in real-world functioning Nichrome wire that were not incorporated into the analytical model. For this reason, the upcoming current values determined by a conductive

analytical model of the Nichrome wire surrounded by SMP should be considered to have a non-negligible amount of error as well.

8.1.3 Analytically determining power required to maintain Nichrome temperature in Veriflex

As per Newton's Law of Cooling, the heat generation from the Nichrome wires (which is equal to the electrical power supplied to it) must be equal to the heat lost from it to the surrounding system.

$$q_{generated} = q_{electrical} = q_{cond} \tag{8.6}$$

Two-dimensional heat transfer per length in a medium bounded by two isothermal surfaces, T_1 and T_2, may be represented in terms of a conduction shape factor S, as given in Eq. 8.7.

$$q_{cond} = k\ S(T_1 - T_2) \tag{8.7}$$

where,

q_{cond} = Heat flow

k = Thermal conductivity of Veriflex = 0.17 (W/m/^{o}C)

S = Conduction shape factor

T_1-T_2 = Change in temperature from wire to SMP medium = 135 ^{o}C - 23 ^{o}C =112 ^{o}C

Values of the shape factor, S, have been solved for a variety of different geometries in (Hahne, 1975) and so an appropriate one is chosen. The corresponding shape factor is given below in Eq. 8.8 for an isothermal cylinder buried in an infinite medium.

$$S = \frac{4\pi}{\ln\left(\frac{2L}{r}\right)}, \quad \frac{r}{L} \leq 0.1 \tag{8.8}$$

where,

r = Radius of wire

L = Length of wire

Using Eqs. 8.6 - 8.8, the heat flow from the Nichrome wire for each gauge wire was found. Similar to the convection method, these values were then set equal to the electrical power supplied to the Nichrome ($P = I^2*R$) and the current required to maintain the Nichrome at 135^{o}C was then found.

Table 8-5 Current required to maintain 1m of Nichrome at 135^{o}C in Veriflex at 23^{o}C

AWG (Gauge)	Diameter (inches)	Radius (meters)	S	q, ΔT=123^{o}C (heat loss, W)	Resistance (Ohms/m)	Current (A)
20	0.032	4.06E-04	1.48	28.1	2.16	3.61
22	0.0253	3.21E-04	1.44	27.4	3.46	2.81
24	0.02	2.54E-04	1.40	26.7	5.48	2.21
26	0.0159	2.02E-04	1.37	26.0	8.76	1.72
28	0.0126	1.60E-04	1.33	25.4	14.0	1.35
30	0.01	1.27E-04	1.30	24.8	21.9	1.06

Using required Nichrome lengths from Table 8-2 and required currents from Table 8-5, the required power supplied to the Nichrome wire to sufficiently heat the SMP is calculated for each gauge wire at the given spacing. The current required to heat Nichrome wire to 135^{o}C in SMP is squared and then multiplied by the total resistance of wire needed to sufficiently heat

the SMP (from Table 8-2). Essentially, this is just finding power through Ohm's Law, P = I^2*R. This is also given below in Eq. 8.9.

$$Power = \left(Current\ required\ for\ 135^{o}C\right)^2 \times \frac{\mathrm{Re}\,sis\tan ce}{meter} \times Total\ length\ of\ Nichrome \qquad (8.9)$$

Table 8-6 Total power (W) required for SMP to reach 62°C for each gauge at the given spacing

		Total power (W) required for SMP to reach 62°C for each gauge at the given spacing			
Gauge	Radius (mm)	4x	6x	8x	10x
20	0.406	103	69.2	52.4	42.4
22	0.321	126	84.6	64.0	51.6
24	0.254	155	104	78.3	63.0
26	0.202	189	127	95.5	76.8
28	0.160	232	155	117	93.9
30	0.127	285	190	143	115

To determine the energy required for the SMP in the FESMPP plate to be completely heated, the required powers from Table 8-4 are multiplied by the required times from Table 8-1. These numbers are shown below in Table 8-7.

Table 8-7 Total energy (J) needed for SMP to reach 62°C for each gauge at the given spacing

		Total energy (J) needed for SMP to reach 62°C for each gauge at the given spacing			
Gauge	Radius (mm)	4x	6x	8x	10x
20	0.406	3360	2780	2550	2550
22	0.321	4250	3400	3070	2940
24	0.254	5330	4170	3710	3480
26	0.202	6687	5170	4470	4110
28	0.160	8370	6360	5470	4960
30	0.127	10600	7880	6690	6000

Looking at Table 8-7, it appears as though the additional energy required to power the thicker gauge wire was worth it. Looking at Table 8-1 and Table 8-7, it appears as though

further spacing between the wires results in less required energy to heat the SMP to its transition temperature, however, it takes a longer period of time. Also interesting to note is that twice the spacing between the fibers corresponded to twice the total length of fiber needed, which in turn corresponded to twice the resistance, which then corresponded to twice the power required.

8.2 FORCE REQUIRED TO SHEAR SMP PLATE

The Instron machine (from Figure 7-2) was used to determine the loads required to shear the tile into its rhombic state. Shown below in Figure 8-4 is a plot of the force required to shear an SMP sample versus the increase in length of the plate's diagonal.

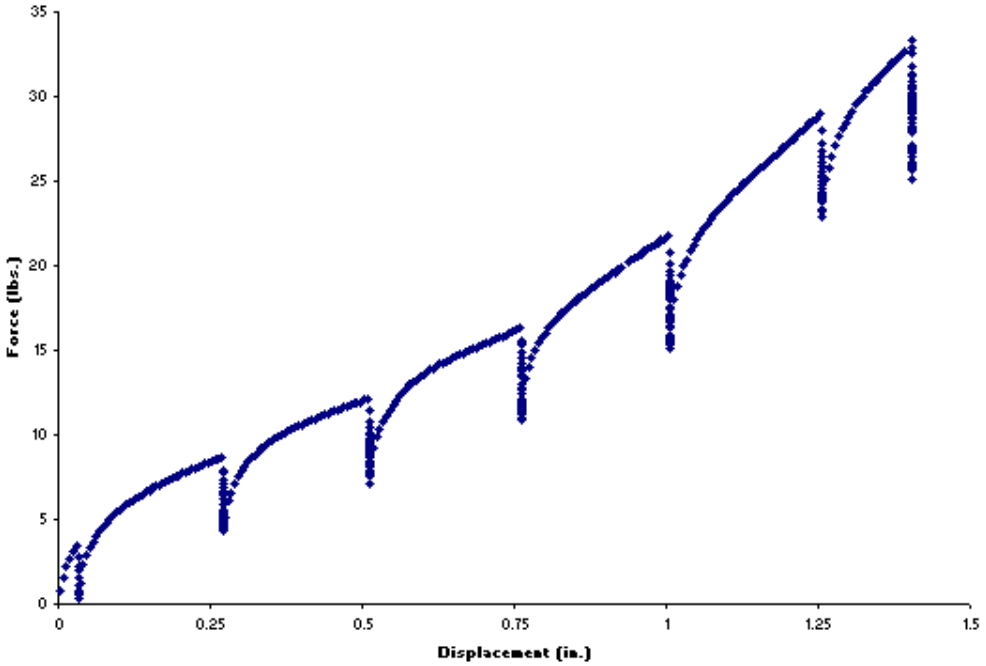

Figure 8-4 Plot of force seen by load cell while pulling on the ends of the shearing fixture versus the corresponding vertical displacement

Note that the large drop-offs in force occurring roughly every 0.25" correspond to when the load frame was paused and the gripping clamps were re-tightened. This was required because the thickness of the SMP shrank as its planar lengths were increased (as per the effect of Poisson's ratio).

This force vs. displacement relationship was converted to a force vs. angle of deformation relationship to more directly relate to the morphing aircraft application for which this thesis was originally intended. This was done using the geometric relationships shown below in Figure 8-5.

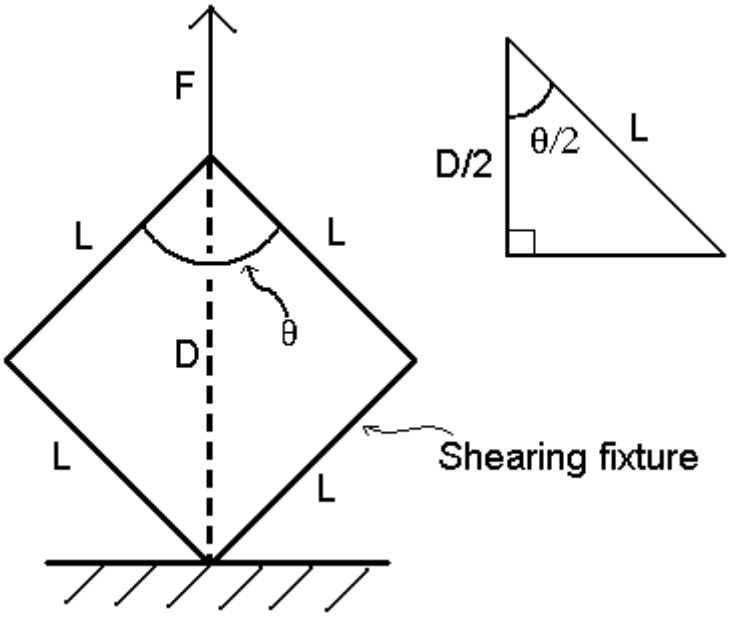

Figure 8-5 Geometric relationship of the vertical displacement of the shearing fixture and the shape-change angle associated with both itself and the contained SMP sample

The diagonal length of the tile directly corresponded to the vertical displacement of the load cell grips and so a relationship between the diagonal length and inner angle was generated.

$$\theta = 2 \cdot \cos^{-1}\left(\frac{(D+d)/2}{L}\right) \tag{8.1}$$

where,

L = Length of a side of the shearing fixture = 4.93 in.

D = Initial diagonal length of shearing fixture in vertical direction = 6.97 in.

90 - θ = Angle of shear deformation of both fixture and SMP sample (initially 0^o)

d = Vertical displacement of load cell grip (initially 0 in.)

D + d = Current diagonal length of SMP tile

Using Eq. 8.1, Figure 8-6 was created to show the given force required to shear the SMP tile a given angle. It is important to note that this is the force required to shear just one tile in the potentially very large array of tiles that would be used in the skin of a morphing aircraft.

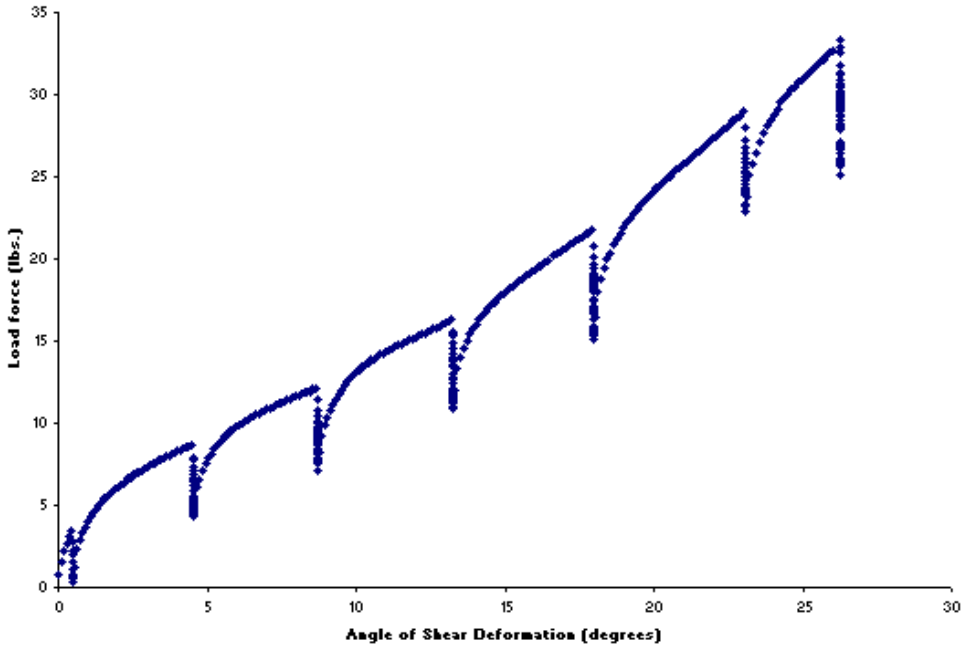

Figure 8-6 Plot of force seen by load cell versus the shear deformation of the SMP sample

9.0 CONCLUSIONS AND SUGGESTIONS FOR FUTURE WORK

Even during the early stages of fabrication and initial prototype testing, it was immediately clear that real-life application of an array of SMP tiles into a morphing aircraft wing would be a difficult task. Probably the most supportive testament to this realization was the amount of force that was required to shear a single SMP tile just 26 degrees. The final design specification of the morphing aircraft for which the testing in this thesis was originally intended called for a shear-induced shape-change angle of 45 degrees. Looking at the force requirements in Figure 8-6 above, it is not unreasonable to assume that a load required to shear the tile 45 degrees might be as high as 75 pounds. An array of these tiles would require a very large force to induce the needed shape-change. Also relevant to the difficulty of real-life application was the tendency of the SMP to tear during the pre-straining process. This behavior was evident, although only slightly, even with the solid gripped pre-tensioning method. Since the maximum successful pre-tensions used in this thesis corresponded to only about 25 degrees of deformation, and a final morphing aircraft might need up to 60 degrees of deformation, it can be assumed that the SMP would be even more likely to tear at some stage of the pre-tensioning or shearing. Obviously even a small tear anywhere in the SMP while it is functioning as the skin of a morphing aircraft would be detrimental to the flight of the aircraft. While the concept of counteracting the onset of buckling with pre-tension was proven in this thesis, pre-tensioning the SMP to the needed amount for use in real-life application where large

angles of shape-change are needed (>30 degrees) while maintaining structural integrity might be, and likely is, an impossible task with standard Veriflex. However, for a morphing application that requires small angles of shape-change (<30 degrees) , Veriflex may prove to be a viable solution for wing skin material. Also, the amount of shape-change supported by Veriflex would probably increase as the thickness of the SMP layer decreased since less force would be required to pre-strain the material, although more reinforcement fibers would be needed to compensate for the lost strength.

The analytical models were accurate in predicting the real-world behavior of both the SMP plate and the FESMP plate as they were subjected to aerodynamic loads while in their un-heated states. Since the analytical models were linear and the true physical behavior of the plates in their heated states were non-linear (as shown by the matching ANSYS and experimental results), analytic results for the SMP plates in their heated states were irrelevant. Due to the difficult workability of SMP and the associated tile fabrication, the errors calculated between the models and the experimental values were thought to be reasonable.

A few problems associated with the embedded fiber heating elements were noticed as samples were fabricated and analyses were conducted. Realistically, a morphing aircraft would likely see very high altitudes and very high wind speeds, which would significantly change the heat convection on the outside of the skin of its wing. This means that the power requirements associated with the heating of the SMP plate through its embedded fibers only hold true in very calm conditions. The power required to heat an SMP plate in harsher aerodynamic conditions would of course be significantly higher. Also, bi-axially pre-straining an SMP plate with already embedded fibers would inevitably create tears in the SMP. This could be avoided by embedding the fibers into the SMP after it has already been pre-tensioned

by drilling axial holes through the SMP and threading the fibers. This could be also be avoided by instead adding an array of heating elements on the underside of the SMP after it has been pre-tensioned rather than embedding fibers prior to pre-straining and embedding elastic fibers in the SMP prior to pre-tensioning. It is recommended that heating of the SMP via embedded wires be weighed against the advantages and disadvantages of heating through different means, such as a laser, light or magnet. Finally, as per the previous allusions, it will likely be required to use a material other than the currently available standard Veriflex for real-life implementation in a morphing aircraft requiring high deformations in the wing. This is not to say that standard Veriflex will not ever work in morphing that required large changes of angle, but rather a different material would probably be a better choice at this point in time. An ideal material would have very high resistance to out-of-plane deformation in both its heated and un-heated states while having very little resistance to shearing in its heated state. A material possessing these properties would require minimal force to shear (and therefore minimal force to induce shape-change in a morphing aircraft) while still resisting the out-of-plane deformations resulting from an aerodynamic load.

APPENDIX A

ANSYS CODE FOR HEATING POWER REQUIREMENTS

```
/title, Fiber-Embedded SMP Plate for Thermal/Structural Analysis
/filname,rad space
/prep7

!!!!!!!!!!!!!!!!!!!Creating Material Properties and Element Types!!!!!!!!!!!!!!!!!!!

et,1,PLANE55                !SMP
MP,    DENS, 1,     920                 !Density
MP,    KXX,  1,     0.17                !Thermal conductivity
MP,     C,   1,     1800                !specific heat
                            !Nichrome
MP,    DENS, 2,     8400
MP,    KXX,  2,     13.2
MP,     C,   2,     450

!!!!!!!!!!!!!!!!!!!Creating Model Geometry!!!!!!!!!!!!!!!!!!!

wireradius=.000254/2
wirespace=6*wireradius
wirespacefirst=wirespace/2
width=12*wirespace
thick=.00635

k,1, 0,0.0
k,2, width,0,0
k,3, 0,thick,0
k,4, width,thick,0
A,1,2,4,3
lplot
/pnum,line,1
```

```
lplot
CYL4,wirespacefirst,thick/2,wireradius,360,,,0
asba,1,2,,KEEP1, DELETE2          !keep area 1 and set as area 3
adele,1                            !first wire hole lines 5,6,7,8 (Quadrant1,Q2,Q3,Q4)
CYL4,wirespacefirst+wirespace,thick/2,wireradius,360,,,0
asba,3,1,,KEEP3, DELETE1          !keep area 3 and set as area 2
adele,3                            !second wire hole lines 9,10,11,12(Q1,Q2,Q3,Q4)
CYL4,wirespacefirst+2*wirespace,thick/2,wireradius,360,,,0
asba,2,1,,KEEP2, DELETE1          !keep area 2 and set as area 3
adele,2                            !third wire hole lines 13,14,15,16(Q1,Q2,Q3,Q4)
CYL4,wirespacefirst+3*wirespace,thick/2,wireradius,360,,,0
asba,3,1,,KEEP3, DELETE1          !keep area 3 and set as area 2
adele,3

CYL4,wirespacefirst+4*wirespace,thick/2,wireradius,360,,,0
asba,2,1,,KEEP2, DELETE1          !keep area 2 and set as area 3
adele,2                            !third wire hole lines 13,14,15,16(Q1,Q2,Q3,Q4)
CYL4,wirespacefirst+5*wirespace,thick/2,wireradius,360,,,0
asba,3,1,,KEEP3, DELETE1          !keep area 3 and set as area 2
adele,3
CYL4,wirespacefirst+6*wirespace,thick/2,wireradius,360,,,0
asba,2,1,,KEEP2, DELETE1          !keep area 2 and set as area 3
adele,2                            !third wire hole lines 13,14,15,16(Q1,Q2,Q3,Q4)
CYL4,wirespacefirst+7*wirespace,thick/2,wireradius,360,,,0
asba,3,1,,KEEP3, DELETE1          !keep area 3 and set as area 2
adele,3

CYL4,wirespacefirst+8*wirespace,thick/2,wireradius,360,,,0
asba,2,1,,KEEP2, DELETE1          !keep area 2 and set as area 3
adele,2                            !third wire hole lines 13,14,15,16(Q1,Q2,Q3,Q4)
CYL4,wirespacefirst+9*wirespace,thick/2,wireradius,360,,,0
asba,3,1,,KEEP3, DELETE1          !keep area 3 and set as area 2
adele,3
CYL4,wirespacefirst+10*wirespace,thick/2,wireradius,360,,,0
asba,2,1,,KEEP2, DELETE1          !keep area 2 and set as area 3
adele,2                  !third wire hole lines 13,14,15,16(Q1,Q2,Q3,Q4)
CYL4,wirespacefirst+11*wirespace,thick/2,wireradius,360,,,0
asba,3,1,,KEEP3, DELETE1          !keep area 3 and set as area 2
adele,3
allsel
aplot
                                                        !lines 5 - 52
lplot
asel,all
cm,smparea,area
CYL4,wirespacefirst,thick/2,wireradius,360,,,0
```

```
CYL4,wirespacefirst+wirespace,thick/2,wireradius,360,,,0
CYL4,wirespacefirst+2*wirespace,thick/2,wireradius,360,,,0
CYL4,wirespacefirst+3*wirespace,thick/2,wireradius,360,,,0
CYL4,wirespacefirst+4*wirespace,thick/2,wireradius,360,,,0
CYL4,wirespacefirst+5*wirespace,thick/2,wireradius,360,,,0
CYL4,wirespacefirst+6*wirespace,thick/2,wireradius,360,,,0
CYL4,wirespacefirst+7*wirespace,thick/2,wireradius,360,,,0
CYL4,wirespacefirst+8*wirespace,thick/2,wireradius,360,,,0
CYL4,wirespacefirst+9*wirespace,thick/2,wireradius,360,,,0
CYL4,wirespacefirst+10*wirespace,thick/2,wireradius,360,,,0
CYL4,wirespacefirst+11*wirespace,thick/2,wireradius,360,,,0        !wire lines 53 - 100

asel,u,area,,smparea,,,0                !wires are now areas 1,3,4,5
cm,wirearea,area
asel,all
aplot

!!!!!!!!!!!!!!!!!!!Meshing Model Geometry!!!!!!!!!!!!!!!!!!!

type,1                                  !using element type 1 defined above for SMP
mat,1                                   !using material 1 defined above for SMP
smrtsize,2
mshape,1,2d
amesh,smparea                           !mesh SMP area

type,1                                  !using element type 2 for Nichrome
mat,2                                   !using material 2 for Nichrome
smrtsize,2
mshape,1,2d
amesh,wirearea                          !mesh wire area

roomtemp=23
wiretemp=135                            !max operating temp 900C
FC=17                                   !film coefficient for air
TCC=500                                 !thermal contact conductance (Modeled at perfect)

!!!!!!!!!!!!!!!!!!!Creating Contact Pairs!!!!!!!!!!!!!!!!!!!

/COM, CONTACT PAIR CREATION - START
CM,_NODECM,NODE
CM,_ELEMCM,ELEM
CM,_KPCM,KP
CM,_LINECM,LINE
CM,_AREACM,AREA
CM,_VOLUCM,VOLU
/GSAV,cwz,gsav,,temp
```

```
MP,MU,1,
MAT,1
R,3
REAL,3
ET,2,169
ET,3,172
KEYOPT,3,9,0
KEYOPT,3,10,2
R,3,
RMORE,
RMORE,,TCC
RMORE,0
KEYOPT,3,1,2
! Generate the target surface
LSEL,S,,,5
LSEL,A,,,6
LSEL,A,,,7
LSEL,A,,,8
LSEL,A,,,9
LSEL,A,,,10
LSEL,A,,,11
LSEL,A,,,12
LSEL,A,,,13
LSEL,A,,,14
LSEL,A,,,15
LSEL,A,,,16
LSEL,A,,,17
LSEL,A,,,18
LSEL,A,,,19
LSEL,A,,,20
LSEL,A,,,21
LSEL,A,,,22
LSEL,A,,,23
LSEL,A,,,24
LSEL,A,,,25
LSEL,A,,,26
LSEL,A,,,27
LSEL,A,,,28
LSEL,A,,,29
LSEL,A,,,30
LSEL,A,,,31
LSEL,A,,,32
LSEL,A,,,33
LSEL,A,,,34
LSEL,A,,,35
LSEL,A,,,36
```

```
LSEL,A,,,37
LSEL,A,,,38
LSEL,A,,,39
LSEL,A,,,40
LSEL,A,,,41
LSEL,A,,,42
LSEL,A,,,43
LSEL,A,,,44
LSEL,A,,,45
LSEL,A,,,46
LSEL,A,,,47
LSEL,A,,,48
LSEL,A,,,49
LSEL,A,,,50
LSEL,A,,,51
LSEL,A,,,52
CM,_TARGET,LINE
TYPE,2
NSLL,S,1
ESLN,S,0
ESURF
CMSEL,S,_ELEMCM
! Generate the contact surface
LSEL,S,,,53
LSEL,A,,,54
LSEL,A,,,55
LSEL,A,,,56
LSEL,A,,,57
LSEL,A,,,58
LSEL,A,,,59
LSEL,A,,,60
LSEL,A,,,61
LSEL,A,,,62
LSEL,A,,,63
LSEL,A,,,64
LSEL,A,,,65
LSEL,A,,,66
LSEL,A,,,67
LSEL,A,,,68
LSEL,A,,,69
LSEL,A,,,70
LSEL,A,,,71
LSEL,A,,,72
LSEL,A,,,73
LSEL,A,,,74
LSEL,A,,,75
```

```
LSEL,A,,,76
LSEL,A,,,77
LSEL,A,,,78
LSEL,A,,,79
LSEL,A,,,80
LSEL,A,,,81
LSEL,A,,,82
LSEL,A,,,83
LSEL,A,,,84
LSEL,A,,,85
LSEL,A,,,86
LSEL,A,,,87
LSEL,A,,,88
LSEL,A,,,89
LSEL,A,,,90
LSEL,A,,,91
LSEL,A,,,92
LSEL,A,,,93
LSEL,A,,,94
LSEL,A,,,95
LSEL,A,,,96
LSEL,A,,,97
LSEL,A,,,98
LSEL,A,,,99
LSEL,A,,,100
CM,_CONTACT,LINE
TYPE,3
NSLL,S,1
ESLN,S,0
ESURF
ALLSEL
ESEL,ALL
ESEL,S,TYPE,,2
ESEL,A,TYPE,,3
ESEL,R,REAL,,3
/PSYMB,ESYS,1
/PNUM,TYPE,1
/NUM,1
EPLOT
ESEL,ALL
ESEL,S,TYPE,,2
ESEL,A,TYPE,,3
ESEL,R,REAL,,3
CMSEL,A,_NODECM
CMDEL,_NODECM
CMSEL,A,_ELEMCM
```

```
CMDEL,_ELEMCM
CMSEL,S,_KPCM
CMDEL,_KPCM
CMSEL,S,_LINECM
CMDEL,_LINECM
CMSEL,S,_AREACM
CMDEL,_AREACM
CMSEL,S,_VOLUCM
CMDEL,_VOLUCM
/GRES,cwz,gsav
CMDEL,_TARGET
CMDEL,_CONTACT
/COM, CONTACT PAIR CREATION - END
allsel

!!!!!!!!!!!!!!!!!!!Specifying Transient Solution!!!!!!!!!!!!!!!!!!!

/solu
antype,trans,new
solcontrol,
NSUBST,100,1000,100
OUTRES,ERASE
OUTRES,ALL,ALL
AUTOTS,1
KBC,1
TIME,60

!!!!!!!!!!!!!!!!!!!Specifying Loads and Boundary Conditions!!!!!!!!!!!!!!!!!!!
lsel,s,line,,1,4,1,0
cm,outerlines,line
sfl,outerlines,conv,FC,,roomtemp          !convection surface load on lines, film coeff specified
da,wirearea,temp,wiretemp                 !dof temp constraint on wire areas
ic,all,temp,roomtemp,,,                   !inital condition temp of 23C for SMP nodes
allsel
solve

!!!!!!!!!!!!!!!!!!!Post-Processing!!!!!!!!!!!!!!!!!!!

/post1
/triad,off
plnsol,temp,,0,,
/CVAL,1,30,50,62,67,75,90,110,wiretemp
/REPLOT
*ASK,Continue,Press any key to continue,1
```

```
!!!!!!!!!!!!!!!!!!!Time-History Post-Processing!!!!!!!!!!!!!!!!!!!

/post26
topmidnode=node(wirespace*6,thick,0)
nsol,2,topmidnode,temp,,Surface_Node_Temp_Between_Wires
store
xvar,1
plvar,2                                 !Transition Temp at 62C
prvar,2
```

ANSYS CODE FOR FESMPP UNDERGOING AERODYNAMIC LOAD

```
/title, Fiber-Embedded SMP Plate for Structural Analysis
/filname,SMPP-3DShearLoading
/prep7

!!!!!!!!!!!!!!!!!!!Creating Material Properties and Element Types!!!!!!!!!!!!!!!!!!!

et,1,SOLID95
                                !SMP
MP,     EX,     1,      7.981E8
!w/o wires:hot 1050E6, cold 240E3, w wires:hot 7.981E8, cold 1.843E9
MP,     EZ,     1,      2.41E5
!w/o wires:hot 1050E6, cold 240E3, w wires:hot 2.41E5, cold 1.054E9
MP,     EY,     1,      2.41E5
MP,     DENS,   1,      8400            !Density
MP,     PRXY,   1,      .45
MP,     PRYZ,   1,      .45
MP,     PRXZ,   1,      .45
MP,     GXY,    1,      8.312E4
!w wires: cold 3.636E8, hot 8.312E4, w/o wires:cold 3.621E8, hot 8.276E4
MP,     GYZ,    1,      8.312E4
MP,     GXZ,    1,      8.312E4
!MP,    KXX,    1,      0.17            !Thermal conductivity
!MP,     C,      1,      1800            !specific heat
                                !Nichrome
MP,     EX,     2,      186E9
MP,     DENS,   2,      920
MP,     PRXY,   2,      .3
!MP,    KXX,    2,      13.3
!MP,     C,      2,      450
```

```
!!!!!!!!!!!!!!!!!!!Creating Model Geometry!!!!!!!!!!!!!!!!!!!

width=3
thick=.25
length=3
k,1, 0,0.0
k,2, width,0,0
k,3, 0,thick,0
k,4, width,thick,0
A,1,2,4,3
asel,all
cm,smparea,area
aplot
vext,smparea,,,0,0,length
vplot
cm,smpvolu,volu

!!!!!!!!!!!!!!!!!!!Meshing Model Geometry!!!!!!!!!!!!!!!!!!!

type,1                  !using element type 1 defined above for SMP
mat,1                   !using material 1 defined above for SMP
smrtsize,1
mshape,1,3d
vmesh,smpvolu                   !mesh SMP area
erefine,all,,,2         !1 produces a jagged corner
allsel

!!!!!!!!!!!!!!!!!!!Specifying Static Solution!!!!!!!!!!!!!!!!!!!

/solu
antype,static
nlgeom,on
da,1,all,0
da,2,all,0
da,4,all,0
da,6,all,0
sfa,3,,PRES,18615.8110288  !(2.7psi) (400psf)
allsel
solve
finish

!!!!!!!!!!!!!!!!!!!General Post-Processing!!!!!!!!!!!!!!!!!!!

/post1
SET,first
plnsol,u,y,0
```

/VIEW,1,1,2,3
/REP,FAST

BIBLIOGRAPHY

Abdulrahim, M.," Flight Performance Characteristics of a Biologically-Inspired Morphing Aircraft," *43rd AIAA Aerospace Sciences Meeting and Exhibit*. Reno, Nevada. AIAA 2005-345. 2005.

Ashton, J.E., Whitney, J.M. *Theory of Laminated Plates*. Technomic Publishing Co., Inc. : Stamford, CT. 1970.

Bae, J., Kyong, N., Seigler, T. and Inman, D., "Aeroelastic Considerations on Shape Control of an Adaptive Wing," *Journal of Intelligent Material Systems and Structures*. Vol. 16, pp. 1051-1056. 2007.

Bortolin, R. "Characterization of shape-memory polymers for use as a morphing aircraft skin material," University of Dayton. August 2005.

Buckley, P., McKinley, G., Wilson, T., Small IV, W. Benett, W., Bearinger, J., McElfresh, M. and Maitland, D. "Inductively Heated Shape Memory Polymer for the Magnetic Actuation of Medical Devices," *IEEE Transactions on Biomedical Engineering*, Vol. 53, No. 10, pp. 2075-2083. 2006.

Conti, S., Lenz, M. and Rumpf, M. "Modeling and simulation of magnetic-shape-memory polymer composites," *Journal of Mechanics and Physics of Solids*. Vol. 55, pp. 1462-1486. 2007.

Duenas, T., Bolanos, E., Murphy, E., Mal, A., Wudl., F., Wang, Y., Hahn, H., Ooi, T. and Bortolin, R., "Multifunctional Self-Healing and Morphing Composites," *NextGen Aeronautics Incorporated*.

Gall, K., Christopher, Y., Liu, Y, Shandas, R., Willett, N. and Anseth, K. "Thermomechanics of the shape memory effect in polymers for biomedical applications," *Wiley InterScience*. April 2005. pp. 339-348

Hahne, E., and Grigull, U.: Formfaktor und Formweiderstand der stationaren mehrdimensionalen Warmeleitung, *Int. J. Heat Mass Transfer*, vol. 18, p. 751, 1975.

Holman, J.P. *Heat Transfer*. McGraw-Hill Book Company: New York. 1981.

Huang, W. and Yang, B. "Water-driven programmable polyurethane shape memory polymer: Demonstration and mechanism," *Applied Physics Letters*. Vol. 86, No. 114105, pp. 1-3. 2005.

Jones, R.M. *Mechanics of Composite Materials: Second Edition*. Taylor & Francis, Inc.: Philadelphia, PA. 1999.

Kakac, S. and Yener, Y. *Heat Conduction*. Taylor & Francis, Inc.: Washington, D.C. 1993.

Kauffman, G. and Mayo, I. "Memory Metal," *Chem Matters*. Oct. 1993: 4-7.

Kudva, J., "Overview of the DARPA Smart Wing Project," *Journal of Intelligent Material Systems and Structures*. Vol.15, pp. 261-267. 2004.

Leissa, A.W. *Vibration of Plates.* Office of Technology Utilization, National Aeronautics and Space Administration: Washington, D.C. 1969.

Lendlein, A. and Langer, R., "Biodegradable, Elastic Shape-Memory Polymers for Potential Biomedical Application," *Science*. Vol. 296, No. 5573, pp. 1673 - 1676. 2002.

Lendlein, A., Hongyan Jiang, Junger, O., Langer, R. "Light-induced shape-memory polymers," *Nature*. Vol. 434. pp. 879-882. 2005.

Liang, C., Rogers, C., and Malafeew, E. "Investigation of Shape Memory Polymers and Their Hybrid Composites," *Journal of Intelligent Material Systems and Structures*. Vol. 8, No. 4, pp. 380-386. 1997.

Maitland, D.J., Small IV, W., Ortega, J., Buckley, P., Rodriguez, J., Hartman, J. and Wilson, T., "Prototype laser-activated shape memory polymer foam device for embolic treatment of aneurysms," *Journal of Biomedical Optics*. Vol. 12(3). pp. 030504-1-3. 2007.

McFarland, D. *Analysis of Plates.* Spartan Books: New York. 1972.

Mei-Chin Chen, Hung-Wen Tsai, Yen Chang, Wei-Yun Lai, Fwu-Long Mi, Chin-Tang Liu, Hen-Sheng Wong and Hsing-Wen Sung, "Rapidly Self-Expandable Polymeric Stents with a Shape-Memory Property," *Biomacromolecules*. Vol. 8, pp. 2774-2780. 2007.

Reddy, J.N. *Mechanics of Laminated Composite Plates: Theory and Analysis*. CRC Press: Boca Raton. 1997.

Schmidt, A., "Electromagnetic Activation of Shape Memory Polymer Networks Containing Magnetic Nanoparticles," *Molecular Rapid Communications*, Vol. 27, pp. 1168-1172. 2006.

Slaughter, W.S. *The Linearized Theory of Elasticity*. Birkhauser:Boston. 2002.

Small IV, W., Metzger, M., Wilson, T. and Maitland, D., "Laser-Activated Shape Memory Polymer Microactuator for Thrombus Removal Following Ischemic Stroke: Preliminary *In Vitro* Analysis," *Journal of Selected Topics in Quantum Electronics*. Vol. 11, No. 4. pp. 892-901. 2005.

Swanson, S.R. *Introduction to Design and Analysis with Advanced Composite Materials.* Prentice Hall: Upper Saddle River, NJ. 1997.

Tey, S., Huang, W. and Sokolowski, W., "Influence of long-term storage in cold hibernation on strain recovery and recovery stress of polyurethane shape memory polymer foam," *Smart Materials and Structures*. Vol. 10, pp. 321-325. 2001.

Timoshenko, S. *Theory of Elastic Stability.* McGraw-Hill Book Company: New York. 1936.

Timoshenko, S., Woinowsky-Krieger, S. *Theory of Plates and Shells*. McGraw-Hill Book Company: New York. 1959.

Ugural, A.C. *Stresses in Plates and Shells*. McGraw-Hill Book Company: New York. 1981.

Wache, H. M., Tartakowska, D. J., Hentrich, A., and Wagner, M. H., "Development of a polymer stent with shape memory effect as a drug delivery system," *Journal of Materials Science: Materials in Medicine*. Vol. 14, pp. 109-112. 2003.

Yousefi-Koma, A. and Zimcik, D., "Applications of Smart Structures to Aircraft for Performance Enhancement," *Canadian Aeronautics and Space Journal*. Vol. 49, No. 4, pp. 163-172. 2003.

"MOR Electric Heating Assoc., Inc." 2008. http://www.heatersplus.com/wire.htm

"CRG Industries, LLC" 2008. http://crgindustries.com/index.html